Doctral Dissertation

Fabrication and Characterization of Oxide Materials with Low Thermal Conductivity

(低熱伝導率酸化物材料の創生と特性評価)

Takuji MAEKAWA

Division of Sustainable Energy and Environmental Engineering,
Graduate School of Engineering, Osaka University

2008

Doctral Dissertation

Fabrication and Characterization of Oxide Materials with Low Thermal Conductivity

（低熱伝導率酸化物材料の創生と特性評価）

Takuji MAEKAWA

Division of Sustainable Energy and Environmental Engineering,
Graduate School of Engineering, Osaka University

2008

Abstract

In the present study, the author studied the thermophysical properties of alkaline earth perovskite oxide materials and alkaline earth and yttrium oxide materials on bulk, and the fabrication and characterization of TiO_2 and ZrO_2 films grown by MOCVD. The purpose of this study is the development of new materials and the modification of oxides for applications required low thermal conductivity, such as thermal barrier coating (TBC) and thermoelectric (TE) conversion. In the chapter 2, thermophysical properties of alkaline earth perovskite type oxides and alkaline earth and yttrium oxide materials on bulk were systematically evaluated. The thermophysical properties were dependent on the relation of the crystal symmetry. The thermal conductivity of evaluated samples in this study is slightly higher than the thermal conductivity of YSZ, around 2 $Wm^{-1}K^{-1}$. It is necessary to decrease it more to apply it as a new substitute for thermal barrier coating material, a replacement of YSZ. However $SrHfO_3$, SrY_2O_4, and BaY_2O_4 have a potential to be utilized as TBC materials because they have high temperature stability and enough large thermal expansion coefficient. The author tried to offer the material design of low thermal conductivity materials. However, innovative TBCs require the overall performance, such as low thermal conductivity (<2 $Wm^{-1}K^{-1}$), high thermal expansion coefficient conductivity (>$9x10^{-6}$ K^{-1}), a stable phase, chemical resistance, a low sintering rate, and high fracture toughness. In the chapter 3, the relationship between the microstructure and the thermal conductivity of the TiO_2 and ZrO_2 films with different morphologies prepared by MOCVD was studied. The dense texture films, feather-like texture films, and substrate-free film of TiO_2 with anatase structures were obtained. The granule texture films and cauliflower-shaped texture films of ZrO_2 were obtained. A quantitative analysis of the amount of oxygen and amount of carbon impurities in the TiO_2 and ZrO_2 films were performed using RBS and NRA measurements. The amounts of oxygen were comparable among the

samples. However, the amounts of carbon impurities differed slightly: the films deposited at 660 Pa contain high carbon impurities. The amounts of oxygen and carbon impurities are closely related to the deposition condition of the films. The dense-textured TiO_2 films exhibited slightly lower thermal conductivity than that of bulk TiO_2; this was a result of the low relative density of the TiO_2 films. The feather-like textured TiO_2 films exhibited extremely low thermal conductivity -- below 0.5 $Wm^{-1}K^{-1}$ -- which is probably due to the grain boundaries oriented perpendicular to the heat flow direction. Both the granule texture ZrO_2 film and cauliflower-shaped texture ZrO_2 film showed low thermal conductivity, approximately 0.4 $Wm^{-1}K^{-1}$ and 0.6 $Wm^{-1}K^{-1}$ at room temperature. There are more grain boundaries in the granule texture film compared with the cauliflower-shaped texture film. The author has succeeded in realizing the thermal conductivity tuning in the films by controlling the microstructure. The results obtained in the present study apply to both TBC and TE designs for the development of high-performance materials. The systematic interests of the property would offer possibilities for applications of its properties in different branches of new engineering.

Contents

Chapter 1

General introduction

In this chapter, the author outlines the developmental status of advance energy, and the systems of thermal barrier coating and thermoelectric conversion as applications in the present research from the view point of the reduction of environmental burdens.

1.1. Introduction

Since the Industrial Revolution started in Britain in the 18th century, the human race has continued to consume a large amount of energy in comparison with the preindustrial time, thus rapidly improving the cultural level. Particularly, modes of transportation of products, telecommunication access methods, and so on have been greatly developed by utilizing an enormous amount of energy generated with fossil fuels, such as oil and coal. The improvement of the cultural level for this period is truly revolutionary compared with the cultural level until then. This fact is not an exaggeration. However, at the same time as this revolutionary cultural improvement, the exhaustion of the energy source had started a fatal problem for the human race. In recent years, the amount of the fossil fuel production is close to being in balance. However, the time needed for living things to be converted to energy is not equal to the time it takes humans to use up that energy. Under this situation, slightly extending the number of years for fossil fuel mining is not a fundamental solution for the "Longevity" of human beings. Humans rely heavily on the fossil fuels that lead to carbon dioxide (CO_2) emissions. Reduction of fossil fuel usage would also lower the cultural level–an act modern society would find difficult. Therefore, humans can not part with this high level of culture once tasted.

With the exhaustion of fossil fuels near, humans have been researching the energy source issue. A variety of alternative energy sources to replace fossil fuels has been proposed. Nitrogenous substances and CO_2 are not generated to take out energy when using clean energy, such as solar

energy and wind power [1,2]. However, it would be necessary to cover 10% of the Earth's surface with solar panels to supply the entire world's electricity with only solar power. Moreover, destruction of the surrounding environment due to these panels is unavoidable. Of course, these forms of alternative energy do not exhaust environmental pollutants, such as nitrogenous substances, sulfur compounds, et cetera as when energy is taken out of fossil fuel. However, other forms of clean energy also have faults. For example, wind power stations generate noise. In addition, it is difficult to completely replace fossil fuels with energy substitutes like clean energy.

Another new energy source is nuclear energy, created by focusing the energy of a nuclear fission reaction using the neutron [3]. Energy plants using this nuclear fission reaction are compact because this reaction has a very high output energy density. This energy density is no comparison with clean energy. Moreover, the energy can be taken out continuously using a neutron source in the nuclear reactor because the nuclear fission reactions are chain reactions. The fuel also has a possibility to ensure a stable energy supply for a long period of time by changing ^{238}U, which accounts for 99.3% of the natural uranium, into ^{239}Pu in the fast breeder reactor (FBR) [4]. Nuclear power is useful for putting the energy problem on hold for a while. However, atomic energy is enough to cause a shattering impact when an accident occurs. In the event of an accident, such as the explosion and core meltdown of the nuclear reactor as typified by Chernobyl, radioactive pollution spreads not only to the plant's surroundings, but also over a vast range. The person who handles this energy source needs not only advanced knowledge but also ethics, as it can be applied to the production of military arms technology, namely a nuclear weapon. In addition, technical problems, such as the disposal of high-level radioactive waste from the nuclear reactor, still remain.

The use of a large amount of hydrogen, including light hydrogen (H), deuterium (D) and tritium (T), which existed on Earth as other new energy

sources, has already been researched. The attempt to acquire energy by nuclear fusion reactions with hydrogen has been done for many years [5,6]. Some methods of taking out energy caused by nuclear fusions, such as a magnetic field confinement method, an inertia confinement method, et cetera, have been proposed. At the present time, it is difficult to continue nuclear fusion reactions without energy input from outside. At the moment, the International Thermonuclear Experimental Reactor (ITER) has been designed and will be built in the near future [7]. However, it will take a long time to achieve the self-ignition condition and to take out energy efficiently.

These situations indicate that there is no ultimate solution for an alternative energy source to fossil fuels. Therefore we have to use burning energy from fossil fuels and fission energy from nuclear fuels right now. For the enhancement of energy efficiency, a combustion temperature of fossil fuels must be achieved to increase this temperature, and high burn-up nuclear fuel must be used for the reduction of spent nuclear fuel.

1.2. Application field

The enhancement of energy efficiency is one of the methods for CO_2 emission control and energy conservation. By around 1990, the 1300 ^{0}C class gas turbine had been developed [8]. A gas turbine of 1500-1700 ^{0}C class is being designed for an achievement of thermal efficiency of 55-60 %. Thermal barrier coatings (TBCs) are widely used to protect hot sections of aircraft and land-based turbines by reducing the temperature of metal substrates [9]. Partially yttria (Y_2O_3) stabilized zirconia (ZrO_2) has been used as TBC materials due to its high linear thermal expansion coefficient (9.2×10^{-6} K^{-1} at 1273 K) as well as its low thermal conductivity (2.0 $Wm^{-1}K^{-1}$ at 1273 K). However, Y_2O_3 stabilized ZrO_2 (YSZ) has a limited temperature capability due to accelerated sintering and phase transformations at high

temperature [10]. As a result, a world-wide effort has been undertaken to identify new candidates for TBC applications [11,12].

The development of new efficient energy conversion methods is also needed for CO_2 emission control and energy conservation. Thermoelectric (TE) conversion has the potential to be an efficient form of energy conversion [13,14]. Thermal energy is changed to electric energy with double-conversion. First, thermal energy of superheated steam generated by a nuclear reaction or burning fossil fuel is changed to mechanical energy of rotational movement using a turbine. Next, electricity generators convert the mechanical energy into electrical energy. On the other hand, TE conversion electrical generation can convert thermal energy into electric energy directly. TE materials whose properties are high Seebeck coefficient, high electric conductivity and low thermal conductivity, have an advantage of high efficiency direct energy conversion [15]. If humans can discover such a sought-after material, the future environment will shift dramatically.

1.3. Thermal barrier coating materials

One of the focal points of this study is the development of new ceramic TBC materials. TBCs are widely used as protection shields against high temperature for the structural components of stationary and aerospace gas turbines. The merit of using ceramic TBCs is well-recognized as a potential to increase operation temperatures of engines, due to the reduction of cooling requirements. The operation temperature increase brings significant improvements in thermal efficiency, performance, and reliability. The TBC system typically consists of a metallic oxidation protection layer and an insulative ceramic topcoat. The topcoat films are used to protect hot sections by reducing the temperature of metal substrates. Their continued development is essential for improving the efficiency and performance of gas turbines by allowing the inlet gas

temperature to be increased further. Currently two processes, electron beam physical vapor deposition (EB-PVD) and atmosphere plasma spraying (APS), are widely used to produce the topcoat of the TBC system. Plasma-sprayed zirconia-based ceramics are one of the most important coating materials because of their low thermal conductivity and unique microstructure as a result of the plasma spraying process. TBCs of YSZ are widely used for the state-of-the-art topcoat material for aircraft and land-based turbines [16,17]. However this standard material has a limited temperature capability. At an application temperature higher than 1473 K, which is envisaged for further improvement of the efficiency of the gas turbine, the YSZ undergoes two detrimental changes. Significant sintering leads to microstructural changes and hence, a reduction of the strain tolerance in combination with an increase of Young's modulus [18]. Higher stress, which leads to the shortening of a life under thermal cyclic loading, will originate in the coating. The second change is a phase change of the non-transformable t'-phase, which is present in the as-sprayed YSZ coating. At elevated temperatures, the t'-prime which transforms into a tetragonal phase will further transform from the monoclinic phases. The transformation is accompanied by a volume change and a high risk for damage to the coating [19]. As a consequence, a considerable reduction of the thermal cycling life is observed. These disadvantageous properties of YSZ at high temperatures prompted an intense effort to identify new candidates for a TBC application in the past [11,12,20-24]. In general, TBC materials have to fulfill most of the following requirements, such as a stable phase, low thermal conductivity (<2 $Wm^{-1}K^{-1}$), high thermal expansion coefficient (>$9x10^{-6}$ K^{-1}), chemical resistance, low sintering rate and high fracture toughness. Detailed overviews on the development of new systems are also available [25-27]. Among the interesting candidates for TBCs, those materials with pyrochlore structure and high melting temperature show promising thermophysical properties. Previous

investigations show excellent physical properties of pyrochlore type materials, i.e., thermal conductivity lower than YSZ and high thermal stability [11,28]. However, the thermal expansion coefficient is typically lower (9-10 x 10^{-6} K^{-1}) than that of YSZ (10-11 x 10^{-6} K^{-1}), which leads to higher thermal stress in the TBC system as both substrate and bond coat have higher thermal expansion coefficients (about 15 x 10^{-6} K^{-1}). In addition, relatively low toughness values are observed in pyrochlore type materials [29], as toughening effects are not expected as observed in YSZ [30]. As a result, the thermal cycling properties are worse than YSZ coating. This problem is relevant for most of the new TBC materials, as the need for thermal stability seems to contradict the ability of transformation toughening. The way to overcome this problem is the use of layered topcoats. The failure of TBC systems often occurs within the TBC close to the bondcoat/topcoat interface [31]. At this location, YSZ is used as a TBC material within a relatively high thermal expansion coefficient and high toughness. The YSZ layer is then coated with the new TBC material (e.g. $La_2Zr_2O_7$), which is able to withstand the typically higher temperatures at this location. In several publications, the effort was reported on $La_2Zr_2O_7$/YSZ double-layer systems that this concept really works [32]. Recently, other groups have been also presented results of double layers prepared by EB-PVD [33]. Before now, the processes of trial and error in the development of the TBC system have been studied. However there are only few ultimate solutions. Seeking new TBC material may be a fundamental solution. Thus, the author paid particular attention to alkaline earth perovskite type oxides and alkaline earth and yttrium oxides for the development of TBC in the present study.

1.4. Thermoelectric conversion materials

In recent years, energy conversion materials attract attention from the viewpoint of effective energy use. The system using TE materials has great advantages. Not only does it utilize the TE property of the materials itself, but it also has high reliability requiring no frequent maintenance. Also, there is no noise and no waste production. These advantages could be demonstrated especially in a small on-site energy conversion system. With TE materials, waste heat would be utilized and electricity would be generated. The efficiency of the energy conversion is evaluated with a TE figure of merit Z. It is defined as

$$Z = \frac{S^2\sigma}{\kappa} \qquad (1.1)$$

where S, σ and κ are the Seebeck coefficient, electrical conductivity, and thermal conductivity, respectively. In addition, $S^2\sigma$ (equal to S^2/ρ, where ρ is electrical resistivity) is often called the power factor. The product of absolute temperature and figure of merit, ZT (dimensionless figure of merit) [34] is often applied to estimate the performance of thermoelectric materials. According to the definition, a large Seebeck coefficient, high electrical conductivity and a smaller value of thermal conductivity are essential for a material with a higher figure of merit. This means high performance TE materials. However, the correlation between these parameters, especially the tradeoff relationship between the Seebeck coefficient and electrical conductivity, makes the correlation difficult to enlarge the power factor. Therefore the maximization of the figure of merit is difficult for this reason. The ZT value of the materials used in the current devices is about 1. The materials, Bi_2Te_3, PbTe et cetera, are state-of-the-art TE conversion materials. However tellurium (Te) is not only scarce as a resource, but also unstable at high temperatures. Moreover, it has toxicity. Therefore it was not used as a commercial use. In addition, stable materials at high temperatures and harmless TE conversion materials are needed. Recently,

oxide materials have attracted attention as an environmentally-friendly type of material from the viewpoint of safety and cheapness. In recent days, although comparatively highly efficient materials, such as $NaCo_2O_4$, $Ca_2Co_2O_5$ or doped $SrTiO_3$, and thin films of $SrTi_{0.8}Nb_{0.2}O_3$, are being developed [35-39], systematic research of physical property have been in need. If systematic research on bulk and film is found to be sufficient for performance, it can be used for business purposes.

1.5. Objectives

The purpose of this study is the development of new materials and the modification of oxides for applications required low thermal conductivity, such as TBC and TE. The strontium (Sr) and barium (Ba) series perovskite type oxide materials have the potential to be attractive functional materials because they have various unique properties in spite of their relatively simple crystal structure. However the detail analyses of the physical (thermal, mechanical, magnetic, et cetera) properties of the alkaline earth perovskites and alkaline earth and yttrium oxides have not been reported. The systematic interests of the property offer possibilities for applications of its properties in different branches of new engineering. To achieve the above-mentioned purpose, the author has systematically studied the thermophysical properties, such as thermal, mechanical and electrical properties, of alkaline earth series perovskite type oxides, and alkaline earth and yttrium oxides with X-ray diffraction (XRD), Raman spectrum, ultrasonic pulue-echo, Vickers hardness, thermal conductivity, and electrical conductivity measurements. Particularly, the thermal expansion coefficient, melting temperature, thermal conductivity, heat capacity, elastic moduli, Debye temperature, Vickers hardness, electric conductivity, Seebeck coefficient, have been measured, and the relationships between the properties were studied. The author then tried to offer the material design

of low thermal conductivity materials using published proposal [40,41].

Film materials have recently received significant attentions as key material technology for their adaptability to the environment, their functionality, and the development of energy material. Ceramic coatings are widely used for various technological applications. In addition, the evaluation of thermal conductivity films is needed in various engineering areas, such as TBCs and TE. In the TBC applications, a low thermal conductivity will provide greater insulation and permit higher turbine operating temperatures and thermal efficiency. In the TE applications, a reduction of thermal conductivity can increase the conversion effect. Therefore, the reduction of the thermal conductivity has been attempted in order to increase the reliability and performance of the materials. In this research, the relationship between microstructure and thermal conductivity of the film fabricated by metal-organic chemical vapor deposition (MOCVD) [42] was evaluated. CVD coatings involve the chemical reactions of gaseous reactants on or near the vicinity of a heated substrate surface [43]. This atomistic deposition method can provide highly pure material with structural control at atomic or nanometric scale level. Moreover, it can produce single layer, multilayer, composite, nanostructured, and functionally graded coating materials with well controlled dimensions and unique structures at low processing temperatures.

Reference

[1] N. P. Cheremisinoff, *Fundamentals of wind energy* (Ann Arbor Science Publishers, Michigan, 1978)

[2] W. C. Dickinson and P. N. Cheremisinoff, *Solar energy technology handbook* (M. Dekker sponsored by American Section of the International Solar Energy Society, inc, New York, 1980)

[3] R. A. Knief, *Nuclear Energy Technology: Theory and Practice of Nuclear Power* (Hemisphere Publishing Corporation, Washington, D. C., 1981)

[4] A. K. Agrawal and J. G. Guppy, *Decay Heat Removal and Natural Convection in Fast Breeder Reactors* (Hemisphere Publishing Corporation, Washington, D. C., 1981)

[5] C. M. Braams and P. E. Stott, *Nuclear Fusion : Half a Century of Magnetic Confinement Fusion Research* (Institute of Physics Publishing, Bristol, UK, 2002)

[6] G. McCracke, *Fusion : The Energy of the Universe* (Academic Press, Burlington, Mass., 2005)

[7] J. C. Wesley, "International Thermonuclear Experimental Reactor: Physics issues, capabilities and physics program plans," *Physics of Plasmas*, **4** 2642-2652 (1997).

[8] M. P. Boyce, *Gas Turbine Engineering Handbook* (Gulf Professional Publishing, Burlington, Mass., 2006)

[9] N. P. Padture, M. Gell, and E. H. Jordan, "Thermal barrier coatings for gas-turbine engine applications," *Science*, **296(5566)** 280-284 (2002).

[10] D. Stoever, G. Pracht, H. Lehmann, M. Dietrich, J.E. Doering, and R. Vassen, "New material concepts for the next generation of plasma-sprayed thermal barrier coatings," *Journal of Thermal Spray Technology*, **13(1)** 76-83 (2004).

[11] H. M. Wang, M. C. Simmonds, and J. M. Rodenburg, "Manufacturing of YbAG coatings and crystallization of the pure and Li_2O-doped Yb_2O_3-Al_2O_3 system by a modified sol-gel method," *Materials Chemistry and Physics*, **77(3)** 802-807 (2003).

[12] K. Matsumoto, Y. Itoh, and T. Kameda, "EB-PVD process and thermal properties of hafnia-based thermal barrier coating," *Science and Technology of Advanced Materials*, **4(2)** 153-158 (2003).

[13] I. B. Cadoff and E. Miller, *Thermoelectric materials and devices* (New York : Reinhold, 1960)

[14] T. C. Harman and J. M. Honig, *Thermoelectric and thermomagnetic effects and applications* (New York : McGraw-Hill, 1967)

[15] T. M. Tritt, "Thermoelectric materials: Holey and unholey semiconductors," *Science*, **283(5403)** 804-805 (1999).

[16] W. A. Nelson and R. M. Orenstein, "BC experience in land-based gas turbines," *Journal of Thermal Spray Technology*, **6(2)** 176-180 (1997)

[17] M. Andritschky, P. Alpuim, D. Stover, and C. Funke, "Study of the mechanics of the delamination of ceramic functional coatings," *Materials Science & Engineering, A: Structural Materials: Properties, Microstructure and Processing*, **A271(1-2)** 62-69 (1999).

[18] C. Funke, B. Siebert, D. Stover, and R. Vaben, "Properties of ZrO2-7wt%Y2O3 thermal barrier coatings in relation to plasma spraying conditions," *Thermal Spray: A United Forum for Scientific and Technological Advances, Proceedings of the United Thermal Spray Conference, 1st, Indianapolis, Sept. 15-18, 1997*, 277-284 (1998).

[19] R. A. Miller, J. L. Smialek, and R. G. Garlink, "Phase stability in plasma-sprayed, partially stabilized zirconia-yttria," *Advances in Ceramics, 3(Sci. Technol. Zirconia)*, 241-253 (1981).

[20] R. L. Jones, R. F.Reidy, and D. Mess, "Scandia, yttria-stabilized zirconia for thermal barrier coatings," *Surface Coating and Technology*, **82(1-2)** 70-76 (1996).

[21] R. Vassen, X. Cao, F. Tietz, D. Basu, and D. Stover, "Zirconates as new materials for thermal barrier coatings," *Journal of the American Ceramic Society*, **83(8)** 2023-2028 (2000).

[22] G. W. Schafer and R. Gadow, "Lanthanum aluminate thermal barrier coating," *Ceramic Engineering and Science Proceedings, 20(4, 23rd Annual Conference on Composites, Advanced Ceramics, Materials, and Structures: B, 1999)*, 291-297 (1999).

[23] M. Dietrich, V. Verlotski, R. Vaben, and D. Stover, "Metal-glass based composites for novel TBC-systems," *Materialwissenschaft und Werkstofftechnik*, **32(8)** 669-672 (2001).

[24] X. Q. Cao, R. Vassen, W. Jungen, S. Schwartz, F. Tietz, and D. Stover, "Thermal stability of lanthanum zirconate plasma-sprayed coating," *Journal of the American Ceramic Society*, **84(9)** 2086-2090 (2001).

[25] R. Vassen and D. Stover, "onventional and new materials for thermal barrier coatings," *NATO Science Series II: Mathematics, Physics and Chemistry, 16(Functional Gradient Materials and Surface Layers Prepared by Fine Particles Technology)*, 199-216 (2001).

[26] D. R. Clarke and C. G. Levi, "Materials design for the next generation thermal barrier coatings," *Annual Review of Materials Research*, **33**, 383-417 (2003).

[27] J. R. Nicholls, "Advances in coating design for high-performance gas turbines," *MRS Bulletin*, **28(9)** 659-670 (2003).

[28] H. Lehmann, D. Pitzer, G. Pracht, R. Vaben, and D. Stover, "Thermal conductivity and thermal expansion coefficients of the lanthanum rare-earth-element zirconate system," *Journal of the American Ceramic Society*, **86(8)** 1338-1344 (2003).

[29] U. Bast and E. Schumann, "Development of novel oxide materials for TBC's," *Ceramics Engineering and Science Proceedings*, **23(4)** 525-532 (2002).

[30] P. D. Harmsworth and R. Stevens, "Phase composition and properties of plasma-sprayed zirconia thermal barrier coatings," *Journal of Materials Science*, **27(3)** 611-615 (1992).

[31] R. Vaben, G. Kerkhoff, and D. Stover, "Development of a micromechanical life prediction model for plasma sprayed thermal barrier coatings," *Materials Science and Engineering, A: Structural Materials: Properties, Microstructure and Processing*, **A303(1-2)** 100-109 (2001).

[32] R. Vassen and D. Stoever, "New thermal barrier coatings based on pyrochlore/ YSZ double layer systems," *Ceramic Engineering and Science Proceedings*, **26(3)** 3-10 (2005).

[33] B. Saruhan, U. Schulz, R. Vassen, G. Pracht, P. Bengtsson, C. Friedrich, R. Knoedler, O, Lavigne, P. Moretto, C. Siry, F. Taricco, N. Coignard, and R. Wing, "Evaluation of two new thermal barrier coating materials produced by APS and EB-PVD," *Ceramic Engineering and Science Proceedings*, **25(4)** 363-373 (2004).

[34] D. M. Rowe, *CRC Handbook of Thermoelectrics* (CRC Press, New York, 1995).

[35] K. Kurosaki, H. Muta, M. Uno, and S. Yamanaka, "Thermoelectric properties of $NaCo_2O_4$," *Journal of Alloys and Compounds*, **315(1-2)** 234-236 (2001).

[36] S. Li, R. Funahashi, I. Matsubara, H. Yamada, K. Ueno, and S. Sodeoka, "Synthesis and thermoelectric properties of the new oxide ceramics Ca3-xSrxCo4O9+δ (x=0.0-1.0)," *Ceramics International*, **27(3)** 321-324, (2001).

[37] H. Muta, K. Kurosaki, and S. Yamanaka, "Thermoelectric properties of rare earth doped $SrTiO_3$," *Journal of Alloys and Compounds*, **350(1-2)** 292-295 (2003).

[38] S. Ohta, S. Nomura, H. Ohta, M. Hirano, H. Hosono, and K. Koumoto, "Large thermoelectric performance of heavily Nb-doped $SrTiO_3$ epitaxial film at high temperature," *Applied Physics Letters*, **87(9)** 092108/1-092108/3 (2005).

[39] H. Ohta, S. Kim, Y. Mune, T. Mizoguchi, K. Nomura, S. Ohta, T. Nomura, Y. Nakanishi, Y. Ikuhara, M. Hirano, H. Hosono, and K. Koumoto, "Giant thermoelectric Seebeck coefficient of a two-dimensional electron gas in $SrTiO_3$," *Nature Materials*, **6(2)** 129-134 (2007).

[40] D. R. Clarke, "Materials selection guidelines for low thermal conductivity thermal barrier coatings," *Surface and Coatings Technology*, **163-164** 67-74 (2003).

[41] M. R. Winter and D. R. Clarke, "Oxide materials with low thermal conductivity," *Journal of the American Ceramic Society*, **90(2)** 533-540 (2007).

[42] H. O. Pierson, *Handbook of Chemical Vapor Deposition : Principles, Technology and Applications* (William Andrew Publishing, Norwich, N. Y.) (2000)

[43] K. L. Choy, "Chemical vapor deposition of coatings," *Progress in Materials Science*, **48(2)** 57-170 (2003)

Chapter 2

Thermophysical properties of bulk oxide materials

In this chapter, the author describes the thermophysical property measurements of Sr and Ba series perovskite type oxides and alkaline earth and yttrium oxide materials on bulk. In addition, the author focuses on the materials for TBC and TE applications. The relationships between the properties, viz. thermal expansion coefficient, melting temperature, thermal conductivity, heat capacity, elastic moduli, Debye temperature, Vickers hardness, electrical conductivity and the Seebeck coefficient of the materials were studied.

2.1. Introduction

At present day, the development of high burn-up uranium-plutonium mixed oxide (MOX) fuels is currently underway with a view toward effective use of energy and improvement of economical efficiency [1,2]. For example, the reduction of the spent fuel emissions can lead to loss of a burden for nuclear fuel cycles. It also helps to further reduce power costs. Therefore, successful promotion of the high burn-up MOX fuel has been widely needed. Safety and reliability will also consequently be achieved. The thermal conductivity of nuclear fuels is significantly important for the evaluation of the safety of the fuel. In irradiated fuel, the number of fission products, which affect the physico-chemical properties of the fuel, is increased. In MOX fuel, some fission products, such as zirconium and rare earth elements, are dissolved in the matrix phase during irradiation. There are two types of precipitated fission products: metallic compounds and ceramic phases. The metallic compound phases are Mo-Ru-Pd-Rh compounds. The ceramic phases are perovskite type structure of $(Ba,Sr)(U,Pu,Zr,RE,Mo)O_3$ [3-9]. The systematic knowledge of the physico-chemical properties of all the phases in the fuel is important to know each property about the composition element.

The perovskite type oxides and related materials have the potential

to be attractive functional materials, such as TE Energy Conversion [10], TBC [11], Solid Oxide Fuel Cell (SOFC) [12] and catalysis applications [13] because they have various unique properties in spite of their relatively simple crystal structure. For example, strontium titanate ($SrTiO_3$) is a typical perovskite dielectric material with a wide range of technological applications. Its special properties, such as ferroelectricity [14], semiconductivity [15], superconductivity [16], catalytic activity [17], and thermoelectricity [18], have been reported extensively. It is known that there are a lot of possible combinations of the constituent elements. In addition, perovskite related materials, such as LSCO ($La_{2-x}Sr_xCuO_4$), have been a focus of a lot of attention in the past ten years in the high-temperature superconductivity (HTSC) research area [19]. Thus, the perovskite related materials are also interesting for applications. However the detail analyses of physical (mechanical, thermal, magnetic, transport, etc.) property on the bulk materials have scarcely been reported until now. The systematic interests, such as material dependence of themophysical properties, have possibilities to be applications of their properties in different branches of new engineering. Therefore the author focused on the perovskite type oxides with a wide range of tolerance factors and alkaline earth and yttrium oxide materials for a development of new candidates. For TBC and TE applications, the reduction of thermal conductivity has been attempted in order to increase the reliability and performance of the materials.

2.1.1. Alkaline earth perovskites

Perovskite type oxide is one of the basic mineral ores, which mineralogist Earl Perovski discovered in the old Russia empire in the 19th century. He found that the composition of the oxide was $CaTiO_3$. At the beginning of the 20th century, $BaTiO_3$ was compounded as a strong dielectric

material. Recent studies have proven that the oxides exhibit a number of noteworthy physical properties. Perovskite-type oxides are significantly attractive as functional inorganic materials, having a strong dielectric [20,21], energy-conversional functionality [22-24], superconductivity [25-27], electronic and ionic conductivity [28], and catalyst functionality [17], etc.

In general, the perovskite-type oxide could be described in terms of ABX_3, where A and B represent metal cations and X represents doubly ionized oxygen anion. The radius of A cation is almost the same as that of the X anion. The B cation has the coordinate number of 6, i.e. the octahedron in which the six corners are occupied by an X anion each (See in Fig. 2.1). Ordinarily, "A" cation site is occupied by alkali, alkali earth and rare earth metals, while the cation settlement on B site depends on the valence states of both A and X ions. Considering the neat combination of the valency of each ions, the chemical formulae of $A^{+}B^{5+}O_3$, $A^{2+}B^{4+}O_3$ and $A^{3+}B^{3+}O_3$ can be easily accepted. In addition, the complex perovskite-type oxides, such as $A^{2+}(B'^{4+}_{0.5}B''^{4+}_{0.5})O_3$ and $A^{2+}(B'^{2+}_{1/3}B''^{5+}_{2/3})O_3$ are now well-recognized. This may imply a lot of possible combinations of the constituent elements. Among the well-known perovskite systems, ABO_3, which has geophysical importance in industrial applications, exhibits some extent of distortion from the high symmetry cubic structure. One of the most commonly adopted perovskite structures is the orthorhombic and tetragonal where the degree of distortion is characterized by the tilting of the BO_6 octahedra. The phenomenological and semi-empirical models of structural distortions gained more and more interest over the past decades. The pioneering study by Goldschmidt [29] was based on the tolerance factor defined in terms of the ionic radium, and it was suitable to establish limits of stability for the perovskite structure. More sophisticated methods followed, which include, for example, the classification of perovskites based on their adopted octahedral tilting, proposed by Glazer [30,31]. The next generation of models consists of semi-empirical relaxation methods by Woodward [32]

and the group theoretical analysis by Howard and Stokes [33].

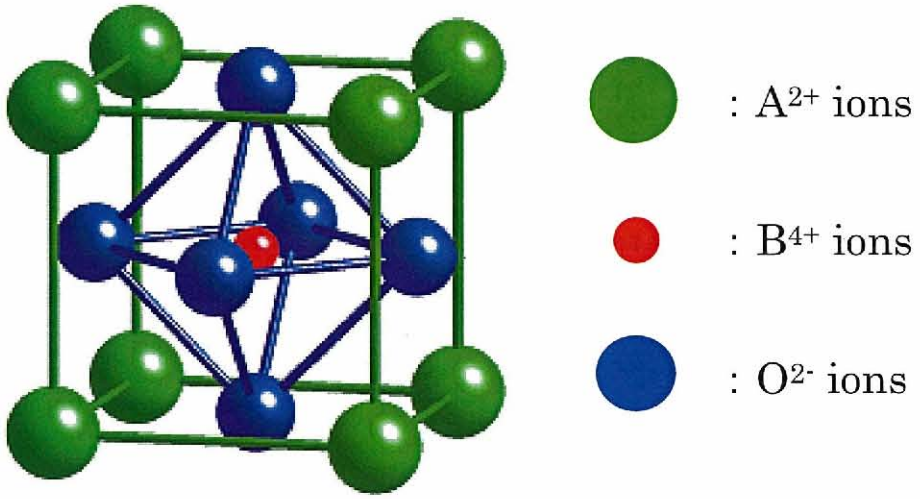

Fig. 2.1 Perovskite type structure

$SrHfO_3$ and $BaHfO_3$ which have a high melting temperature, have been well-known for a long time [34,35]. Recently, Kennedy et al. [36] investigated the high temperature phase transitions using powder neutron diffraction of $SrHfO_3$. $SrRuO_3$ has an interesting magnetic system [37,38] and one of highly conductive metallic oxides [39]. Therefore, it can be used for electrodes and junctions in microelectronic devices. Up to now, many studies have been done on the thin films of $SrRuO_3$ [40-42] at low temperatures. The $SrMoO_3$ compound shows interesting properties, such as metallic conductance and Pauli paramagnetic properties [43]. The low electric resistivity [44] make it an attractive material for electrodes. The electrical and optical studies have been presented in other papers [45-48]. $Ba_{1-x}Sr_xMoO_3$ solid solutions might be thermoelectric materials. It was discovered that barium stannate has interesting applications in materials technology due to its dielectric properties. Stannates have received most attention in recent years as compounds of ceramic dielectric bodies [49] with complex compositions, Alkaline-earth stannates ($ASnO_3$, where A=Ca, Sr,

Ba). And some of their applications are thermally stable capacitors, humidity sensors, gas sensors, et cetera. Barium stannate, $BaSnO_3$, is a cubic perovskite-like compound that behaves as a pure n-type semiconductor with a band gap of 3.4 eV [50,51] and is stable at high temperatures up to over 1273 K [52,53]. Thus, the perovskite-related materials are also interesting for every application. However the detail analyses of physical (mechanical, thermal, magnetic, transport, et cetera) property on the bulk materials have scarcely been reported until now. The systematic interests have possibilities to be applications of their properties in different branches of new engineering.

2.1.2. Alkaline earth and Yttrium oxides

Some research has been undertaken on perovskite and pyrochlore oxides as possible candidates for new TBC materials [54,55]. The author focused on Ba and Sr series yttrium oxide materials, such as SrY_2O_4, BaY_2O_4 and $Ba_3Y_4O_9$ as the new TBC candidate materials. SrY_2O_4 is a typical inter oxide in the Y_2O_3–SrO pseudo-binary system [56]. The crystal structure of SrY_2O_4 is orthorhombic with the space group *Pnam* [57-59] as shown in Fig. 2.2. Although the crystal structure, high temperature stability and optical properties of SrY_2O_4 have already been reported [57-63], the thermal and mechanical properties are scarcely reported. In addition, the physical properties of BaY_2O_4 have also been scarcely reported. Only the crystal structure [64-66] and phase relations [67,68] have been reported. In the present study, polycrystalline sintered samples of SrY_2O_4, BaY_2O_4 and the related material $Ba_3Y_4O_9$ (See Fig. 2.3) were prepared and their thermophysical properties were studied. The aim of the present study is to perform a systematical investigation on the physical properties of Sr and Ba series alkaline earth and yttrium oxide materials, such as SrY_2O_4, BaY_2O_4 and $Ba_3Y_4O_9$, to compare the results.

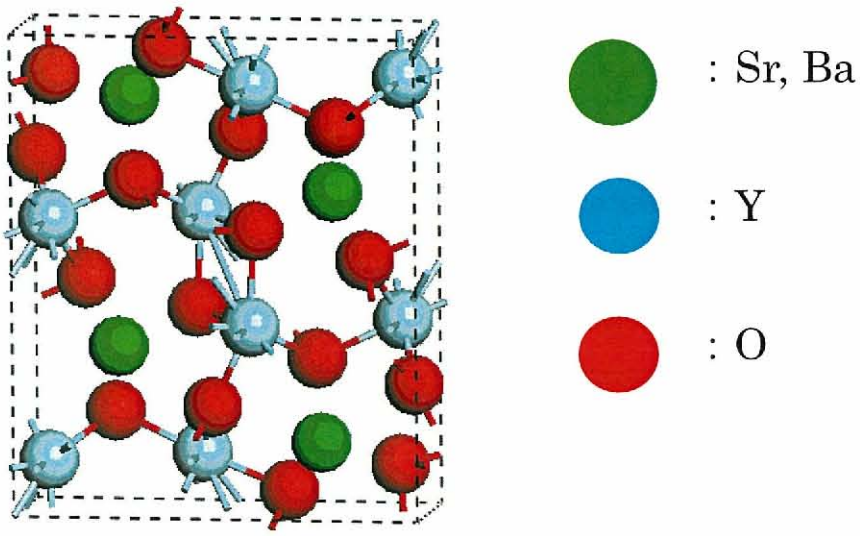

Fig. 2.2 crystal structure of SrY_2O_4 and BaY_2O_4

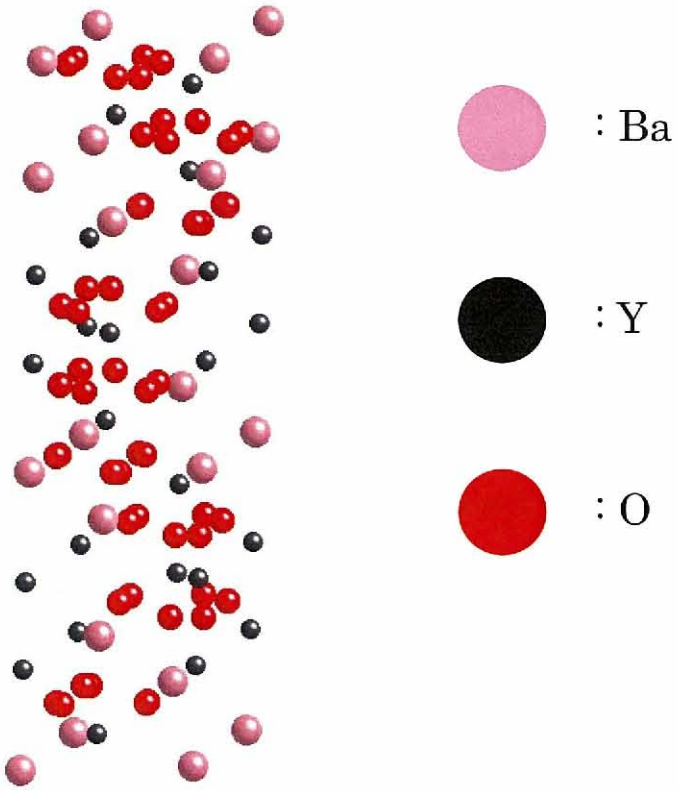

Fig. 2.3 crystal structure of $Ba_3Y_4O_9$

2.2. Experimental procedures

2.2.1. Sample preparation

Sr and Ba series perovskite-type oxides and alkaline earth and yttrium oxide materials were synthesized by a solid-state reaction. For instance, the single phase powder samples of $SrFeO_3$, $SrRuO_3$, $SrHfO_3$, $BaSnO_3$ and $BaHfO_3$ were prepared by mixing the appropriate amounts of starting powdered materials, such as $SrCO_3$ (Aldrich Chemical, 99.9+%), $BaCO_3$ (Wako, 99.9%), Fe_2O_3 (Furuuchi Chemical, 99.99%), RuO_2 (Rare Metallic, 99.9%), SnO (Furuuchi Chemical, 99.9%) and HfO_2 (Furuuchi Chemical, 99.9%) followed by a reaction in air. To prepare the stoichiometric compounds in the mole ratio of 1:1, the starting materials were weighed, mixed and homogenized by hand mixing in mortars. After homogenization, the mixed oxides were pressed into a form of discs with a die and two punches. The pellets were heated in an electric furnace at each temperature for several hours and several times, enough to ensure the completion of the reactions.

The other polycrystalline samples of $Sr_{1-x}Ba_xMoO_3$, such as, $SrMoO_3$, SBM1 ($Sr_{0.75}Ba_{0.25}MoO_3$), SBM2 ($Sr_{0.5}Ba_{0.5}MoO_3$) and SBM3 ($Sr_{0.25}Ba_{0.75}MoO_3$), and $SrVO_3$ were synthesized in a different way. The polycrystalline samples of $SrVO_{3-\delta}$ were prepared by a solid-state reaction using $SrCO_3$ (Wako, 99.9%) and V_2O_3 (Wako, 99+%) or V_2O_5 (Nacalai Tesque, 99%) powders as the starting materials. The two types of starting ingredients were mixed stoichiometrically with the molar ratio of Sr/V for the mixtures being kept constant at 1/1, irrespective of the type of the starting materials. The mixtures pressed uni-axially at 200 MPa into a pellet of 25 mm in the diameter were calcined at 1073 K for 10 h in air. The calcined products were crushed with an agate mortar. The process was repeated. The mixture of $SrCO_3$ and V_2O_5 wad heated up to 873 K for 10 h in air before the calcinations at 1073 K because of the low melting temperature of V_2O_5 (963 K). The powder of the oxygen excess strontium

vanadate was then heated up to the maximum temperature, 1573 K, with a subsequent holding time of 12 h, under a 4% H_2-Ar atmosphere. The process was repeated until the reaction was complete. The stoichiometric quantities of $SrMoO_4$ (Furuuchi Chemical, 99.9%) and $BaMoO_4$ (Furuuchi Chemical, 99.9%) were used as raw materials to prepare single phase powder samples of $Ba_{1-x}Sr_xMoO_4$ with a heat treatment at 1073 K in air. $Ba_{1-x}Sr_xMoO_3$ [44,69] was obtained by the hydrogen reduction of $Ba_{1-x}Sr_xMoO_4$ powder samples under 4% H_2-Ar atmosphere at 1523 K.

After making the single-phase perovskite powder, the polycrystalline $SrHfO_3$ sample was sintered at 1873 K for 10 h in air. On the other hand, the other obtained perovskite powders were placed into a 20 mm-diameter graphite die and given a spark plasma sintering (SPS; Sumitomo Coal Mining, Dr Sinter SPS-1020 or Dr Sinter Lab. SPS-515S apparatus) at each temperature for each time under inert atmosphere, shown in Table 2.1. The temperature was measured by an optical pyrometer focused on the graphite die. During heating, the pressure of 50 MPa was applied to the sample. The heating rate was 300 K min^{-1} from room temperature to 873 K, and 100 K min^{-1} from 873 K to each temperature. For measurements of thermophysical and mechanical properties, appropriate shapes of the samples were cut from the sintered pellets.

For sample preparations of SrY_2O_4, BaY_2O_4 and $Ba_3Y_4O_9$, appropriate amounts of $SrCO_3$ (Aldrich Chemical, 99.9+%), $BaCO_3$ (Wako, 99.9%) and Y_2O_3 (Furuuchi Chemical, 99.99%) powders were mixed and calcined at 1273 K for 10 h in air. $Ba_3Y_4O_9$ powder was reheated at 1773 K for 10 h in air. The calcined intermediates were crushed into powders and these processes were repeated again. After that, the obtained powders were fractionated using a fine sieve (200-mesh). The screened powders underwent SPS (Dr Sinter Lab. SPS-515S) at 1773 K, 1273 K and 1173 K measured by means of an optical pyrometer focused on the graphite die under a nitrogen atmosphere for SrY_2O_4, in a vacuum (<10 Pa) for BaY_2O_4 and in air for

$Ba_3Y_4O_9$ respectively. During the heating, the pressure of 30 MPa was applied to the sample. The heating rate was set to be 100 $Kmin^{-1}$ from room temperature to 873 K, and 50 $Kmin^{-1}$ from 873 K to each maximum temperature. Finally, the sintered samples were annealed in an electric furnace at 1273 K for SrY_2O_4 and BaY_2O_4, and at 1773 K for $Ba_3Y_4O_9$ in air.

Table 2.1 Sample preparation conditions

sample	Starting materials	Reaction temperature	Reaction atmosphere	Sintering temperature	Sintering time	Sintering atmosphere
$SrVO_3$	$SrCO_3 + V_2O_5$	1073 + 1573 K	air + reduction	1573 K	1 m(SPS)	Ar
$SrFeO_3$	$SrCO_3 + Fe_2O_3$	1073 K	air	1273 K	1 m(SPS)	Ar
$SrMoO_3$	$SrMoO_4$	1523 K	reduction	1573 K	0 m(SPS)	N_2
$SrRuO_3$	$SrCO_3 + RuO_2$	823 + 1273 K	air	1673 K	0 m(SPS)	N_2
$SrHfO_3$	$SrCO_3 + HfO_2$	1273 K	air	1873 K	10 h	air
BSM1-3	$BaMoO_4 + SrMoO_4$	1073 + 1523 K	air + reduction	1573 K	0 m(SPS)	Ar
$BaSnO_3$	$BaCO_3 + SnO$	1473 K	air	1623 K	0 m(SPS)	Ar
$BaHfO_3$	$BaCO_3 + HfO_2$	1273 K	air	1773 K	0 m(SPS)	Ar
SrY_2O_4	$SrCO_3 + Y_2O_3$	1273 K	air	1773 K	3 m(SPS)	N_2
BaY_2O_4	$BaCO_3 + Y_2O_3$	1273 K	air	1273 K	0 m(SPS)	vacuum
$Ba_3Y_4O_9$	$BaCO_3 + Y_2O_3$	1773 K	air	1773 K	0 m(SPS)	air

Identification of the obtained materials was performed. The samples were characterized by a scanning electron microscopy (SEM; Hitachi, S-2600H) equipped with an energy dispersive x-ray spectroscopy (EDX; Horiba, EX-200). In order to determine the chemical composition on the surface of the samples, the SEM-EDX analysis was performed. The oxygen analysis was performed using Horiba EMGA-550 to identify the oxygen concentration of the samples. With this apparatus, the sample's powder was heated with metal in the carbon crucible and dissolved in a metallic (Ni and Sn) liquid matrix. Then, the carbon monoxide (CO) produced by oxygen in the sample reacted with carbon and was measured by non-dispersive infrared spectroscopy (NDIR). In this manner, the weight of oxygen in the

sample was determined. The crystal structure was identified by XRD (Rigaku, RINT2000) analysis using Cu-Kα radiation at room temperature. Fabrication of the single-phase material was determined.

2.2.2. Crystallographic properties

To identify the crystal structure and determine the lattice parameters and the density by geometrical measurement of all the samples, powder XRD analysis was performed at room temperature. The lattice parameter was evaluated from the XRD pattern. The bulk density of the samples was determined by the geometric measurement. The high temperature powder XRD (HT-XRD) analysis was performed from room temperature to about 1273 K in a helium flow to study the phase transition and the thermal expansion behavior. The average linear thermal expansion coefficient was calculated in the each temperature range. Raman spectroscopy measurement in air at room temperature was performed using a laser Raman spectroscopy (NR-1100) supplied by JASCO. This system has a photoelectron multiplier as a detecting element and a double monochromator spectrometer with a bandwidth of 0.15 cm^{-1}. The light source used was an argon ion laser at an excitation frequency of 514.5 nm and a power of 25-100 mW. Since the power of the laser influenced the heat excitation of the sample, the conditions of the measurements changed with each sample. The details of the conditions of the Raman spectrum measurements are shown in Table 2.2. After being compensated using indene, all the samples were measured at room temperature in air.

Table 2.2 Conditions of Raman spectrum measurements

Sample	Laser power	Scanning times	Width of slit	Scan speed	Sensitivity
$SrHfO_3$	100 [mW]	1 times	0.40 [mm]	120 [cm^{-1}/min]	20
$SrRuO_3$	100 [mW]	4 times	0.40 [mm]	120 [cm^{-1}/min]	20

2.2.3. Mechanical properties

The longitudinal and shear sound velocities were measured by the ultrasonic pulse-echo method (Nihon Matech, Echometer 1062) at room temperature in air. The sound velocities in the sample were estimated from the sample length and the propagation time between the ultrasonic echoes obtained from the Echometer. The sintered sample was bonded to a 5 MHz longitudinal or shear sound wave echogenic transducer with Sonicoat-SHN15 (Nichigo Acetylene). From the sound velocities, the elastic moduli (Young's modulus, shear modulus, bulk modulus, compressibility, Poisson's ratio, Lame constants, and sonic anisotropic factor) and Debye temperature were evaluated. The hardness was measured by loading a diamond pyramid-type (with apex 136°) indenter into the surface of the specimen at room temperature using the micro-Vickers hardness tester (Matsuzawa Seiki, MHT-1). The hardness tests of perovskites and composite materials were performed under 1 kg (9.8 N) of an indentation load for 30 sec and 15 sec, respectively. The width across the corner was determined using an optical microscope. The measurement was repeated 12 times for each sample, and the average value was calculated from the data in which the maximum and minimum values were excluded [70].

2.2.4. Thermal properties

The specific heat capacities of the samples were measured by the differential scanning calorimeter (DSC; ULVAC, triple-cell DSC) apparatus, in the temperature range from room temperature to about 1273 K. The apparatus has a "triple-cell" system and an adiabatic temperature control system, which was originally developed by Takahashi [71]. The principle of the apparatus is briefly summarized in Takahashi's published paper. The measurement was made out in a high-purity argon (99.999%) flow with a flow rate of 100 ml/min. The accuracy of the apparatus was checked using

an alpha-Alumina (α-Al_2O_3) standard. For the specific heat capacity measurements, the samples with a column shape of approximately 4 mm in diameter and approximately 4 mm in height were pressed using a cold press. The heat capacities were reconfirmed from the Neumann-Kopp's law using the thermodynamic data [72] of (Sr,Ba)O and MO_2.

The thermal diffusivities of the samples were measured by the laser flash method in the temperature range from room temperature to about 1473 K in a vacuum (10^{-4} Pa) by using TC-7000 (ULVAC). The technique is based on transiently heating one surface of the sample with an energy pulse from a ruby laser. Subsequently, the temperature change on the opposite surface was monitored with an indium antimonide infrared detector. The ambient temperature of the sample was established and controlled with a high temperature tube furnace. The ambient temperature was measured with a platinum-rhodium (Pt-10% Rh) thermocouple. In the present study, the thermal diffusivity was determined using the half-time method. The thermal diffusivity data measured during the cooling cycle was also compared with the heating cycle. The excellent agreement of the thermal diffusivity data indicates that the stoichiometry of the samples does not change during the measurement. The thermal conductivity was calculated from the thermal diffusivity D, heat capacity C_p, and density ρ, using the following standard equation:

$$\lambda = DC_p\rho . \qquad (2.1)$$

For the thermal diffusivity measurements, the samples with thickness of about 1 mm thickness were sliced and polished from the sintered pellet. The melting temperature was measured by the thermal arrest method under a reduction atmosphere. The thermal expansion behavior was studied by using a thermal dilatometer (Bruker AXS, TD5020SA) in the temperature range from 300 to about 1273 K in a nitrogen flow in order to evaluate the average linear thermal expansion coefficient.

2.2.5. Electrical properties

In the temperature range between room temperature and about 1073 K, the electrical properties, such as electrical resistivity, electrical conductivity and the Seebeck coefficient were measured simultaneously with a direct current four-point probe method using the ZEM-1 (ULVAC-RIKO) apparatus under a helium atmosphere. Two thermocouples and Ni electrodes, which have a small heater, were mechanically attached to both sides of the sample. The small heaters give the sample temperature gradient (The upper side is the low temperature, and the lower side is the high temperature.). The thermocouples measured not only the temperature of the hotter and cooler sides of the sample but also the voltage between A and B. In order to heat the whole system at a uniform temperature, the sample and electrode were surrounded by a Ni cover. Electric resistivity ρ, electrical conductivity σ and the Seebeck coefficient S of the samples were measured by using the following equations.

$$\rho = \frac{1}{\sigma} \tag{2.2}$$

$$\sigma = \frac{V_{Ref}}{R_{Ref}} \frac{1}{\Delta V} \frac{s}{l} \tag{2.3}$$

$$S = \frac{\Delta V}{\Delta T} \tag{2.4}$$

In Eq. (2.3), R_{Ref} is the resistivity of the reference resistor, V_{Ref} is the voltage of the reference resistor, s is the area of cross section of the sample, and l is the distance between the two electrodes, respectively. In Eq. (2.4), ΔV is the thermoelectric motive force between the thermocouples. The Seebeck coefficient was measured in the temperature gradients ΔT of approximately 3, 5, and 8 K.

2.3. Results and discussion

2.3.1. Alkaline earth perovskites

2.3.1.1. Crystallography characteristics

The sample characteristics are summarized in Table 2.3. The chemical compositions most of the samples do not deviate far from the stoichiometric compositions. On the other hand, the estimated oxygen concentrations other than $SrHfO_3$, $BaSnO_3$ and $BaHfO_3$ are slightly lower than the stoichiometric composition. $SrHfO_3$, $BaSnO_3$ and $BaHfO_3$ show white, $SrVO_3$, $SrFeO_3$ and $SrRuO_3$ show black, and $Sr_{1-x}Ba_xMoO_3$ samples show brown colors.

Table 2.3 chemical compositions of the samples

Sample	Chemical composition		Oxygen
	A^{2+} : B^{4+}	Sr^{2+} : Ba^{2+}	concentration
$SrVO_3$	51 : 49		2.51 ± 0.07
$SrFeO_3$	50 : 50		2.95 ± 0.01
$SrMoO_3$	50 : 50		2.77 ± 0.06
$SrRuO_3$	50 : 50		2.85 ± 0.71
$SrHfO_3$	51 : 49		3.03 ± 0.66
SBM1	52 : 48	74 : 26	2.83 ± 0.02
SBM2	50 : 50	49 : 51	2.86 ± 0.11
SBM3	53 : 47	26 : 74	2.93 ± 0.19
$BaSnO_3$	52 : 48		3.05 ± 0.05
$BaHfO_3$	51 : 49		3.04 ± 0.14

Figure 2.4 shows the XRD profiles of the products: (a) when the V_2O_3 starting material is used, and (b) when the V_2O_5 starting material is used. In the case of the V_2O_5 starting material, the single phase of $SrVO_3$ was obtained, while in the case of the V_2O_3 starting material, the second phase of $Sr_3V_2O_8$ was detected in addition to the main phase. Therefore, the sample of the V_2O_5 starting material was used for the calculation of the lattice

parameter of $SrVO_3$. The powder XRD patterns of the samples at room temperature, such as $SrVO_3$, $SrFeO_3$, $SrMoO_3$, $SrRuO_3$, $SrHfO_3$, $BaSnO_3$ and $BaHfO_3$ are shown in Fig. 2.4(c). Figure 2.4(d) shows the XRD patterns of $Sr_{1-x}Ba_xMoO_4$ as raw materials to prepare $Sr_{1-x}Ba_xMoO_3$, together with the published data [73,74]. In addition, Fig. 2.4(e) shows the XRD patterns of $Sr_{1-x}Ba_xMoO_3$, together with the published data [75,76]. Through these results, the confirmation of the formation of single phase structures was obtained in the present study. The lattice parameters evaluated by using the results, are shown in Table 2.4. The values are in good agreement with published data. Fig. 2.5 shows the chemical composition dependence of lattice parameters for solid solutions of molybdates, $Sr_{1-x}Ba_xMoO_3$. The lattice parameters are changed linearly according to Vegard's rule. The bulk densities of the samples are also shown in Table 2.4 as the percents of the theoretical densities.

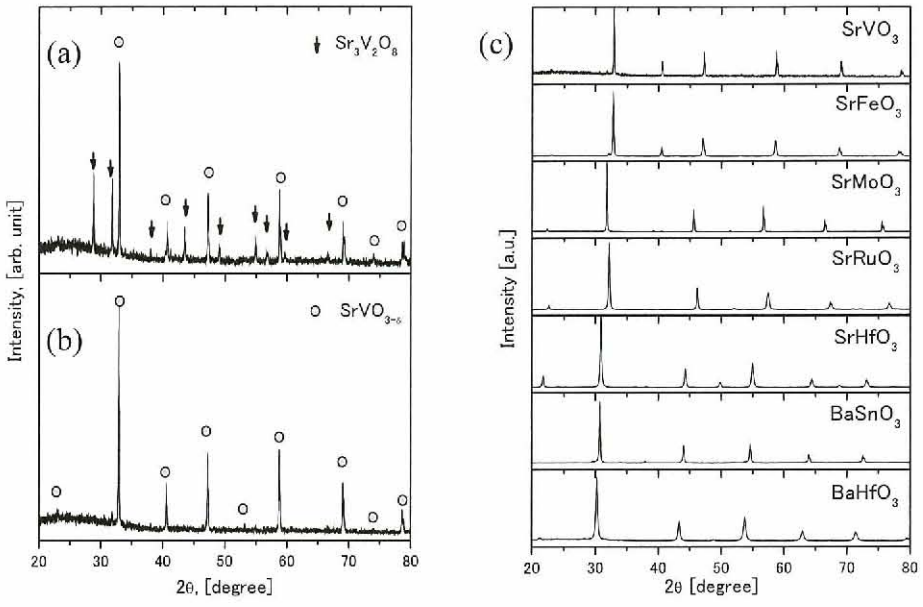

Fig. 2.4. XRD patterns of the product from (a) V_2O_3 and (b) V_2O_5 mixture, and (c) perovskite type oxides

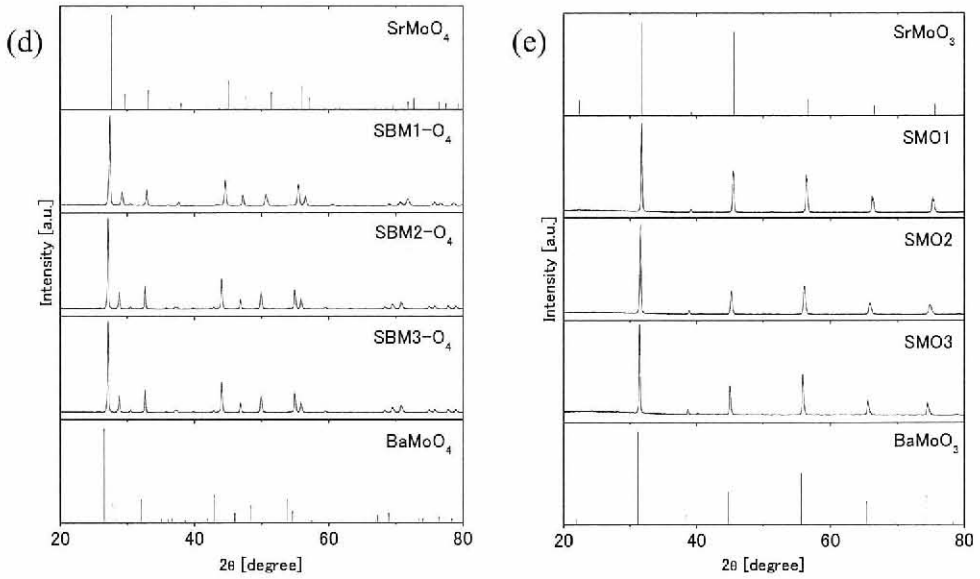

Fig. 2.4 (d,e) XRD patterns of $Sr_{1-x}Ba_xMoO_4$ as raw materials and $Sr_{1-x}Ba_xMoO_3$

Table 2.4 lattice parameters and sample conditions

Sample	Tolerance factor	System at R.T.	Lattice parameter			Relative density
			a [nm]	b [nm]	c [nm]	[%T.D.]
$SrVO_3$	0.986	cubic	0.3841			95
$SrFeO_3$	1.022	cubic	0.3858			87
$SrMoO_3$	0.986	cubic	0.3975			89
$SrRuO_3$	1.001	orthorhombic	0.5569	0.5553	0.7875	97
$SrHfO_3$	0.958	orthorhombic	0.5790	0.5851	0.8243	91
SBM1	1.001	cubic	0.3993			87
SBM2	1.016	cubic	0.4009			92
SBM3	1.031	cubic	0.4024			83
$BaSnO_3$	1.026	cubic	0.4116			95
$BaHfO_3$	1.020	cubic	0.3858			87

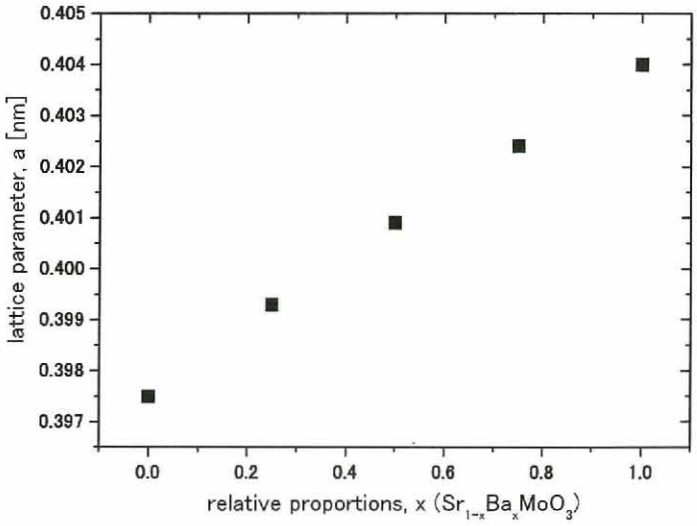

Fig. 2.5 Composition dependence of lattice parameter for $Sr_{1-x}Ba_xMoO_3$

The inclination and rotation of a BO_6 octahedron, and the subtle displacement of atoms reduce the symmetry of perovskite type oxides, which often leads to the transformation of its crystal structure into non-cubic systems. The reduction or disappearance of the crystal distortion gradually occurs when the ambient temperature increases, and the oxides undergoes the phase transition to a space group with a higher symmetry. The conventional parameter describing the geometric distortion of a perovskite type compound is defined as a tolerance factor, *t* [77].

$$t = \frac{r_A + r_O}{\sqrt{2}(r_B + r_o)} \qquad (2.5)$$

In this formula, r_A, r_B, r_O show each ionic radii of each atom. Ordinarily, the value of '*t*' is within 0.75 to 1.1, and the cubic structure has a value near 1. As the value of '*t*' shifts from 1, the geometric distortion becomes gradually large.

In this study, the values of the tolerance factor, '*t*' of the perovskites are shown in Table 2.4. The Shannon values of the ionic radius [78] were used in the present study. The radii are also shown in Table 2.5. When the

molar volume is plotted along the longitudinal y-axis and the B^{4+} ionic radius is plotted on the horizontal x-axis, the result is shown in Fig. 2.6. This figure shows that the lattice volume depends on the radius of the composition ion. Moreover, since the Sr series compound is looser at the point of inclination, it is believed that the interaction between ions of these oxides was stronger than that of Ba series oxides.

Table 2.5 Ionic radii of the components

SHANNON's ionic radium			
Atomic number	Ion	Coordination number	Ionic radium
38	Sr^{2+}	12	0.144 nm
56	Ba^{2+}	12	0.161 nm
23	V^{4+}	6	0.058 nm
26	Fe^{4+}	6	0.0585 nm
42	Mo^{4+}	6	0.065 nm
44	Ru^{4+}	6	0.062 nm
50	Sn^{4+}	6	0.069 nm
72	Hf^{4+}	6	0.071 nm
8	O^{2-}	2	0.135 nm

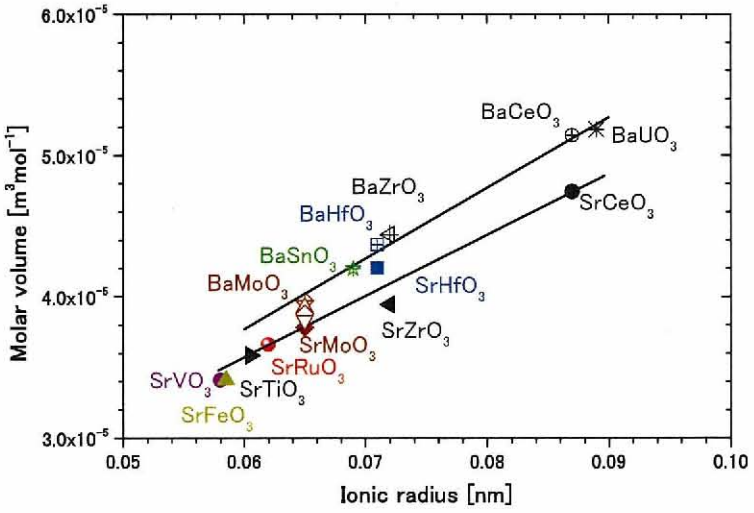

Fig. 2.6 Relationship between molar volume and ionic radius

Recently, Kennedy and Chakoumakos reported high temperature phase transitions in $SrHfO_3$ and $SrRuO_3$ studied by high temperature neutron diffraction using the Rietveld method [36,79,80]. In these papers, it was reported that $SrHfO_3$ undergoes four phase transitions: orthorhombic ($Pbnm$) → orthorhombic ($Cmcm$) → tetragonal ($I4/mcm$) → cubic ($Pm\bar{3}m$). Also, $SrRuO_3$ undergoes three phase transitions: orthorhombic ($Pbnm$) → tetragonal ($I4/mcm$) → cubic ($Pm3m$) (See Fig. 2.7) when the temperature increases. In the present study, the phase transitions in $SrHfO_3$ and $SrRuO_3$ are observed from the HT-XRD analysis. $SrHfO_3$ and $SrRuO_3$ undergo the following phase transitions:

$SrHfO_3$:

orthorhombic ($Pbnm$) $\xrightarrow{800\ K}$ orthorhombic ($Cmcm$) $\xrightarrow{1000\ K}$ tetragonal ($I4/mcm$),

$SrRuO_3$:

orthorhombic ($Pbnm$) $\xrightarrow{800\ K}$ tetragonal ($I4/mcm$) $\xrightarrow{950\ K}$ cubic ($Pm3m$).

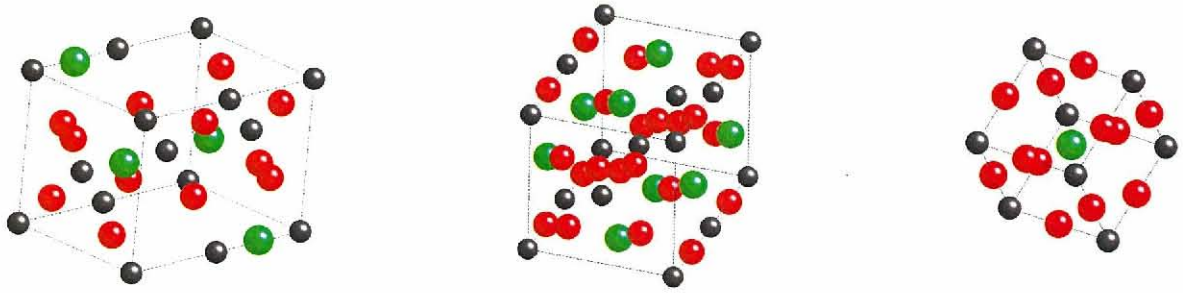

(a) orthorhombic (b) tetragonal (c) cubic

Fig. 2.7 (a,b,c) Crystal structure of $SrRuO_3$

These results are in good agreement with published data [36,80]. From the HT-XRD analysis, the temperature dependences of lattice parameters in the nm scale of $SrHfO_3$ and $SrRuO_3$ are obtained as follows:

$SrHfO_3$, 300 – 800 K, orthorhombic (*Pbnm*):

$$a = 5.68\times10^{-1} + 6.00\times10^{-5}T - 9.53\times10^{-8}T^2 + 6.36\times10^{-11}T^3, \quad (2.6)$$

$$b = 5.67\times10^{-1} + 6.00\times10^{-5}T - 6.90\times10^{-8}T^2 + 2.85\times10^{-11}T^3, \quad (2.7)$$

$$c = 8.15\times10^{-1} - 1.00\times10^{-5}T + 1.18\times10^{-8}T^2, \quad (2.8)$$

$SrHfO_3$, 800 – 1000 K, orthorhombic (*Cmcm*):

$$a = 1.61\times10^{-1} + 2.20\times10^{-3}T - 2.43\times10^{-6}T^2 + 8.95\times10^{-10}T^3, \quad (2.9)$$

$$b = -4.79\times10^{-1} + 4.51\times10^{-3}T - 5.20\times10^{-6}T^2 + 1.99\times10^{-9}T^3, \quad (2.10)$$

$$c = -4.37\times10^{-1} + 4.26\times10^{-3}T - 4.80\times10^{-6}T^2 + 1.81\times10^{-9}T^3, \quad (2.11)$$

$SrHfO_3$, 1000 – 1100 K, tetragonal (*I4/mcm*):

$$a = -5.70\times10^{-1} + 4.18\times10^{-3}T - 4.84\times10^{-6}T^2 + 1.82\times10^{-9}T^3, \quad (2.12)$$

$$c = -3.90\times10^{-1} + 4.27\times10^{-3}T - 4.82\times10^{-6}T^2 + 1.77\times10^{-9}T^3, \quad (2.13)$$

$SrRuO_3$, 300 – 800 K, orthorhombic (*Pbnm*):

$$a = 5.56\times10^{-1} + 2.15\times10^{-6}T + 3.58\times10^{-9}T^2, \quad (2.14)$$

$$b = 5.54\times10^{-1} - 7.93\times10^{-6}T + 3.04\times10^{-8}T^2 - 1.81\times10^{-11}T^3, \quad (2.15)$$

$$c = 7.88\times10^{-1} - 2.00\times10^{-5}T + 5.07\times10^{-8}T^2 - 3.30\times10^{-11}T^3, \quad (2.16)$$

$SrRuO_3$, 800 – 950 K, tetragonal (*I4/mcm*):

$$a = 5.34\times10^{-1} + 3.00\times10^{-5}T + 2.61\times10^{-8}T^2 - 2.96\times10^{-11}T^3, \quad (2.17)$$

$$c = 8.57\times10^{-1} - 5.00\times10^{-5}T - 1.54\times10^{-7}T^2 + 1.47\times10^{-10}T^3, \quad (2.18)$$

$SrRuO_3$, 950 – 1100 K, cubic (*Pm3m*):

$$a = 3.31\times10^{-1} + 1.80\times10^{-4}T - 1.69\times10^{-7}T^2 + 5.52\times10^{-11}T^3, \quad (2.19)$$

where T is in Kelvin. The temperature dependences of the lattice volume (nm^3) are as follows:

$SrHfO_3$, 300 – 1100 K:

$$V = 6.66\times10^{-2} + 5.76\times10^{-6}T - 4.49\times10^{-9}T^2 + 1.93\times10^{-12}T^3, \quad (2.20)$$

$SrRuO_3$, 300 – 1100 K:

$$V = 5.98\times10^{-2} + 3.13\times10^{-6}T - 2.04\times10^{-9}T^2 + 1.13\times10^{-12}T^3, \quad (2.21)$$

where T is temperature in Kelvin. The temperature dependences of linear thermal expansion coefficients α_l in K^{-1} of $SrHfO_3$ and $SrRuO_3$ measured by the HT-XRD are as follows:

$SrHfO_3$, 300 – 1100 K:

$$\alpha_l = 3.88\times10^{-6} + 1.75\times10^{-8}T - 9.49\times10^{-12}T^2, \quad (2.22)$$

$SrRuO_3$, 300 – 1100 K:

$$\alpha_l = -4.16\times10^{-6} + 5.86\times10^{-8}T - 7.78\times10^{-11}T^2 + 3.41\times10^{-14}T^3, \quad (2.23)$$

where T is in Kelvin. The average linear thermal expansion coefficients α_l are 1.13×10^{-5} K^{-1} for $SrHfO_3$ and 1.03×10^{-5} K^{-1} for $SrRuO_3$ in the temperature range between 300 K and 1100 K. On the other hand, the other perovskites, such as $SrVO_3$, $SrMoO_3$, $BaSnO_3$ and $BaHfO_3$, have no phase transition in the all temperature. Figure 2.8 shows the temperature dependence of thermal expansion for perovskite type oxides. The values of average linear thermal expansion coefficients are shown in Table 2.6.

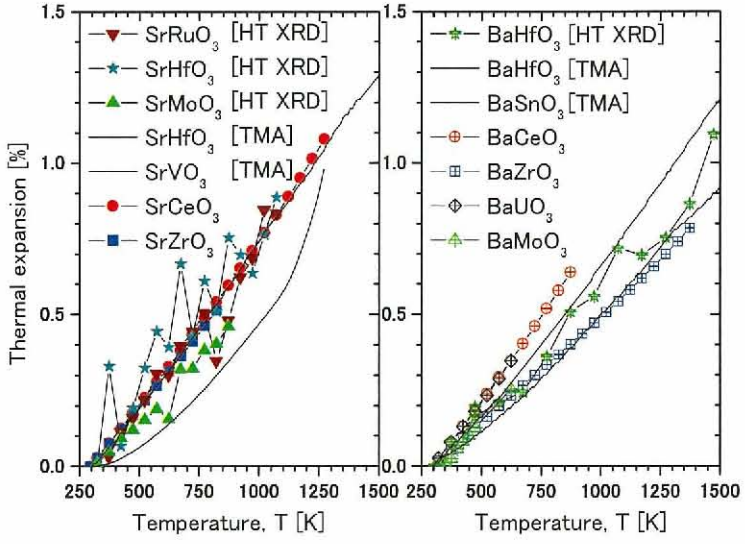

Fig. 2.8 Temperature dependent of thermal expansion for perovskites

Table 2.6 Mechanical properties of perovskits

Sample	V_L (m/s)	V_S (m/s)	A	E (GPa)	G (GPa)	κ (GPa)	β (Gpa^{-1})
$SrVO_3$	7169	4162	1.006	224	90.0	147	6.80 E-03
$SrMoO_3$	6603	3565	0.935	180	69.5	145.8	6.86 E-03
$SrRuO_3$	6312	3083	0.846	161	60.1	171.7	5.83 E-03
$SrHfO_3$	6118	3531	1.000	220	87.9	146.6	6.82 E-03
SBM1	5895	3271	0.961	152	59.3	113.5	8.81 E-03
SBM2	6068	3416	0.975	179	70.7	128.8	7.76 E-03
SBM3	5633	3190	0.981	147	58.1	103.7	9.64 E-03
$BaSnO_3$	6373	3814	1.026	244	99.9	145.8	6.86 E-03
$BaHfO_3$	5397	3245	1.041	194	79.5	113.9	8.78 E-03

Sample	σ	λ (GPa)	θ_D (K)	T_m (K)	Hv (Gpa)	α_l (K^{-1})	D (T.D.)
$SrVO_3$	0.246	87.0	612	(2333)	3.85	1.45 E-05	95 %
$SrMoO_3$	0.294	99.4	510	1967	5.48	7.98 E-06	89 %
$SrRuO_3$	0.343	131.6	448	2575	10.31	1.03 E-05	97 %
$SrHfO_3$	0.250	88.0	490	3200	9.31	1.13 E-05	91 %
SBM1	0.277	74.0	465	-	2.80	-	87 %
SBM2	0.268	81.7	483	-	3.62	-	92 %
SBM3	0.264	65.0	452	-	2.26	-	83 %
$BaSnO_3$	0.221	79.2	522		4.99	-	95 %
$BaHfO_3$	0.217	60.9	438	(2893)	5.08	7.97 E-06	91 %

Raman scattering spectra of the $SrRuO_3$ and $SrHfO_3$ are shown in Fig. 2.9. For the $SrHfO_3$, Raman spectrum measurements have been previously performed and the results have been reported [81], with the exception of the $SrRuO_3$, for which published data had not existed. The typical wave lengths of the $SrHfO_3$ spectrum are detected at 423 and 595 cm^{-1}.

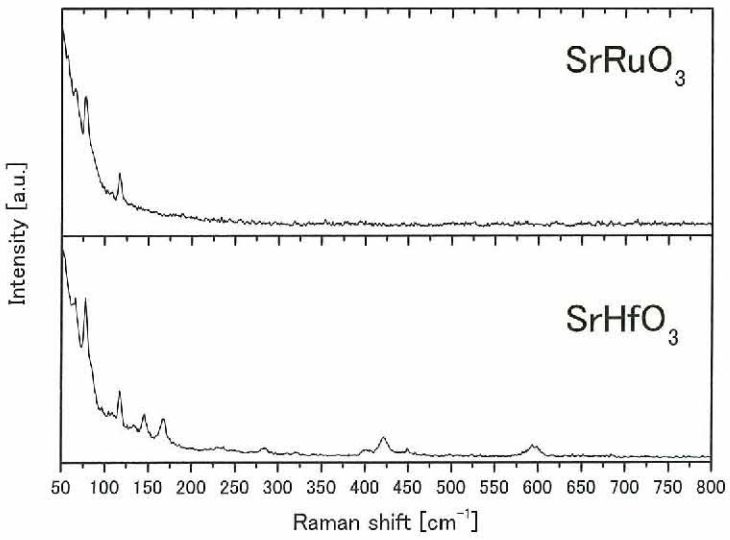

Fig. 2.9 Raman shifts of $SrRuO_3$ and $SrHfO_3$

2.3.1.2. Mechanical properties

The sound velocities of the perovskites were measured at room temperature. The longitudinal wave and the shear wave were measured in the bulk samples. The relationship between the longitudinal and shear waves were estimated using the following formula (2.33).

$$V_S = \frac{V_L}{\sqrt{3}} \tag{2.33}$$

where V_S is shear sound velocity and V_L is longitudinal sound velocity. For an isotropic medium, the Young's modulus E, shear modulus G, compressibility β, bulk modulus K, bulk compressibility β, Poisson's ratio ν and sonic anisotropy coefficient A, and Debye temperature θ_D can be written in terms of using the shear and longitudinal sound velocities as follows [90,91]:

$$E = \frac{\rho V_S^{\,2}\left(3V_L^{\,2} - 4V_S^{\,2}\right)}{\left(V_L^{\,2} - V_S^{\,2}\right)} \tag{2.34}$$

$$G = \rho V_S^{\ 2} \tag{2.35}$$

$$K = \rho(V_L^2 - \frac{4}{3}V_S^2) \tag{2.36}$$

$$\beta = \frac{1}{K} = \frac{1}{\rho(V_L^2 - \frac{4}{3}V_S^2)} \tag{2.37}$$

$$\nu = \frac{1}{2}\frac{(V_L^2 - 2V_S^2)}{(V_L^2 - V_S^2)} \tag{2.38}$$

$$A = \sqrt{3}\frac{V_S}{V_L} \tag{2.39}$$

$$\theta_D = \left(\frac{h}{k_B}\right)\cdot\left[\frac{9N}{4\pi V\cdot\left(V_L^{\ -3} + 2V_S^{\ -3}\right)}\right]^{\frac{1}{3}} \tag{2.40}$$

$$\nu_D = \left[\frac{9N}{4\pi V(v_L^{-3} + 2v_S^{-3})}\right]^{\frac{1}{3}} \tag{2.41}$$

where h is the Plank constant, k_B is the Boltzmann constant, N is the number of atoms in a unit cell, and V is the unit cell volume. The elastic moduli and Debye temperature evaluated in the present study are summarized in Table 2.6. The Vickers hardness H_V was measured by forcing a diamond pyramid type (with apex 136°) indenter into the surface of the specimen, and defined as,

$$H_V = \frac{2P_H \sin\theta}{d^2} = 1.8544\frac{P_H}{d^2} \tag{2.42}$$

where d (mm) is the mean diagonal length of the diamond shaped impression made on the indented surface. P_H is the stress of the indenter [72]. All the results are indicated in Table 2.6. Hardness is associated with the resistance of the material to plastic deformation. For some oxide and carbide ceramics, the hardness H was found to be proportional to Young's modulus E with the values of $H/E=0.05$ [92]. The H/E for pure metals was estimated using the published data [93] and obtained as 0.006, 0.003 and 0.004 for bcc, fcc and hcp metals, respectively [94]. The values of H for

perovskites are plotted in Fig 2.17, as a function of Young's modulus E together with data from the other substances data [95]. As shown in the figure, it was discovered that the relationship between hardness and Young's modulus for $SrRuO_3$ and $SrHfO_3$ showed a different tendency.

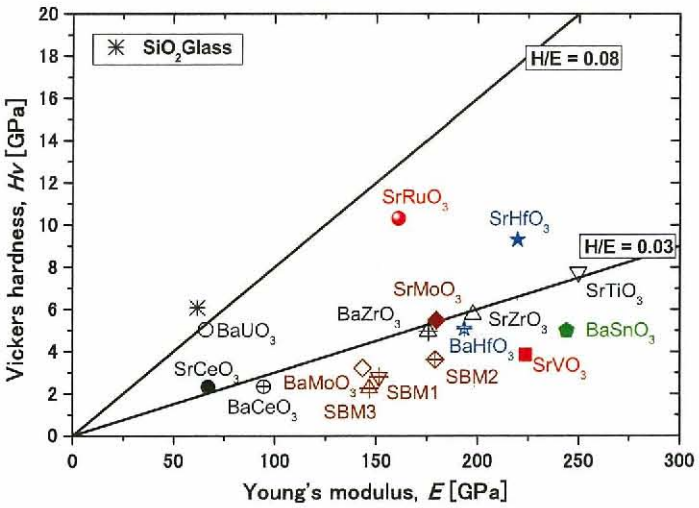

Fig. 2.17 Relationship between H_V and E for perovskite type oxides

In this study, the elastic porosity results were correlated by applying the Duckworth-Knudsen equation. The equation is usually used to determine the dependence of E on porosity according to the following Eq.(2.43):

$$E = E_0 e^{-bP} \tag{2.43}$$

where E is Young' modulus, E_0 is the zero porosity Young's modulus, P is the porosity, and b is the porosity correction factor (for $P < 0.5$). This equation was applied to the E and G experimental results, and a numerical iterative optimization method, known as the simplex algorithm [96], was used to estimate the E_0 values. From these results, correlations among the various perovskite type oxides were evaluated systematically. Correlation between the tolerance factor and various elastic constants are shown in Fig. 2.18.

Figure 2.19 shows the chemical composition dependence of Young's modulus for $Sr_{1-x}Ba_xMoO_3$. They show that there are obvious correlations between the tolerance factor and elastic constants. Is is considered that the symmetry of a crystal is relevant to inter ionic bonding states, therefore the tolerance factor has affected the elasticity-characteristic of materials. Since Young's modulus E is proportional to (d^2U/dr^2) and $1/r$, where U is the potential energy and r is the atom distance, E is related to the cohesive energy U_0 and the equilibrium atom distance r_0. For pure metal, their Young's moduli are proportional to RT_m/V_a [97] where T_m is the melting temperature of pure metal and V_a is the volume of pure metal per gram atom. The relationship of $E = 97.9(RT_m/V_a)$ was obtained for pure metals. A comparison of Young's modulus and melting temperature is shown among perovskite type oxides in Fig. 2.20. It is known that the Debye temperature θ_D can be related to the melting temperature T_m in K, the molar mass M and the molar volume V_m by the Lindemann relationship [98]. The relationship was reexamined for pure metals, and the ratios of θ_D to $(T_m/(MV_m^{2/3}))^{1/2}$ were estimated to be 1.42, 1.60 and 1.80 for bcc, fcc and hcp metals [94]. For perovskite type oxides the following relationship has been reported [99]:

$$\frac{\theta_D}{q^{5/6}(T_m/(MV_m^{2/3}))^{1/2}} \qquad (2.44)$$

where q is the number of atoms in the chemical formulas. Fig. 2.20 shows this relationship for various oxides obtained in the present study, together with the published data [100,101]. The proportional value of most perovskite type oxides is 1.60, which is in correspondence with previous reports.

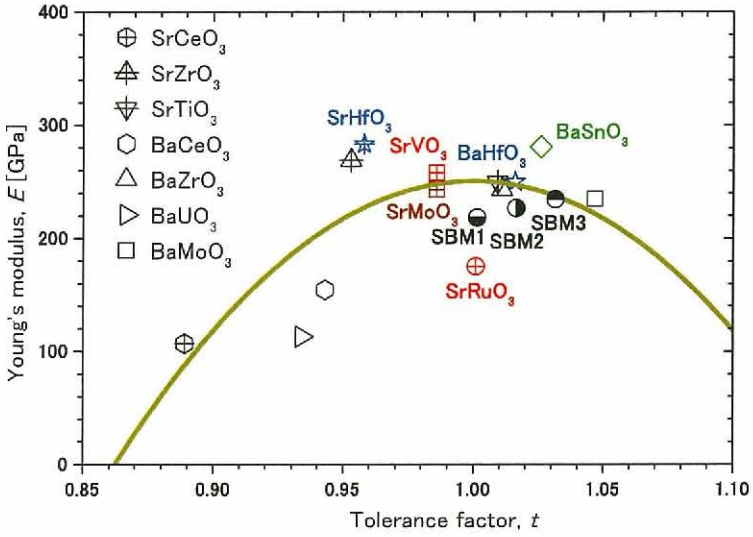

Fig. 2.18 Relationship between E and t for perovskite type oxides

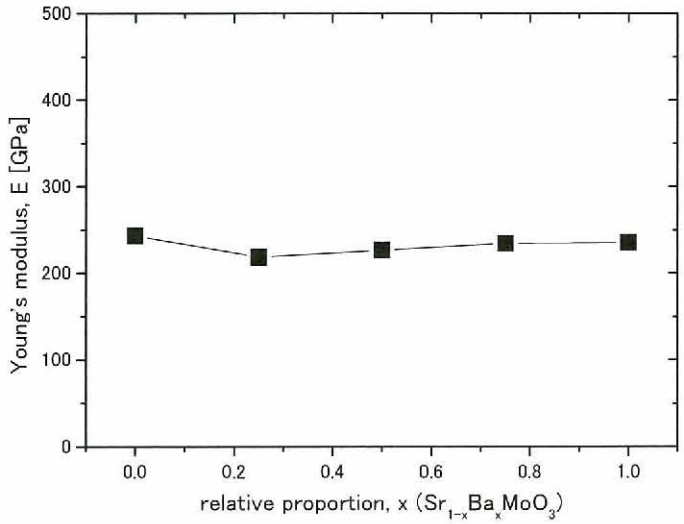

Fig. 2.19 Composition dependence of Young's modulus for perovskites

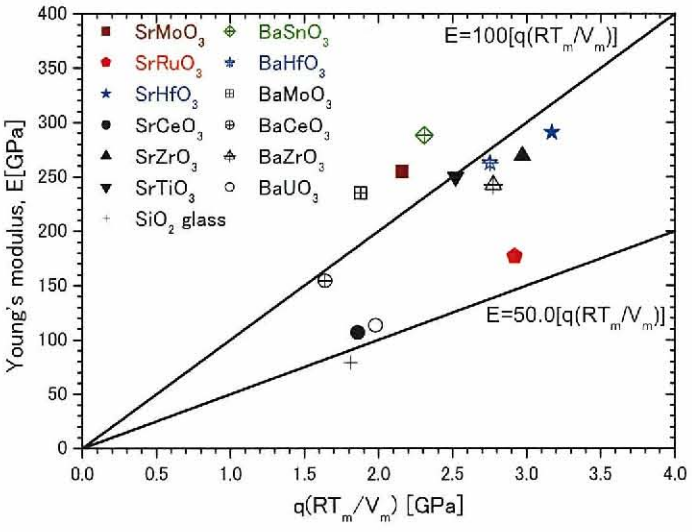

Fig. 2.20 Relationship between E and Tm for perovskites

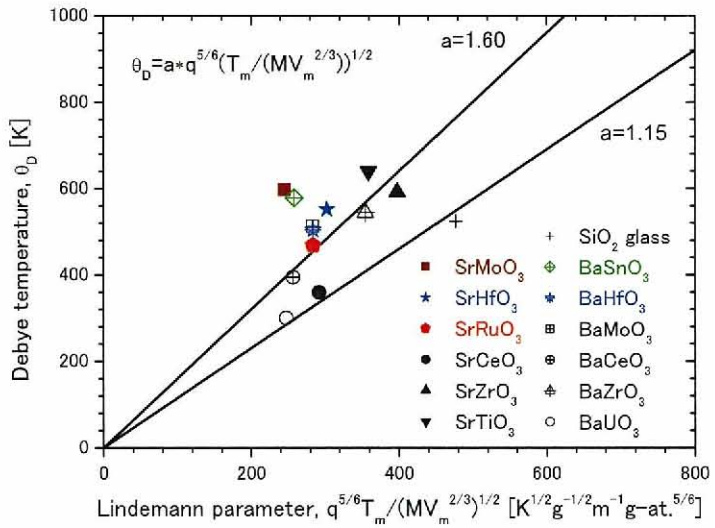

Fig. 2.21 Relationship between Debye temperature and Lindemann parameter

2.3.1.3. Thermal properties

The temperature dependence of the heat capacity for the perovskite type oxides determined by the scanning method in the temperature range between about 300 K and 1300 K is shown in Fig. 2.10. The heat capacity C_p of various oxides can be expressed as follows,

$$C_p = A + B \times T + C \times T^{-2}. \qquad (2.24)$$

The coefficient A, B, and C in this formula were estimated from the experimental data as shown in Table 2.7. Figure 2.11(a) indicates the temperature dependence of the heat capacity of $SrVO_3$. In Fig. 2.11(a), the open circles represent the experimental data obtained from the DSC measurement, the solid line represents the fitting result of the experimental data, the dashed line represents Dulong-Petit's law curve, and the dash-dot line represents Neumann-Kopp's law curve obtained from the published data on SrO and VO_2. The measured heat capacity of $SrVO_3$ is slightly lower than that evaluated by Neumann-Kopp's law. The heat capacity at constant pressure C_P can be evaluated from the following relation:

$$C_P = C_h + C_d + C_{others}, \qquad (2.25)$$

where C_h is the harmonic term, C_d is the lattice dilational term, and C_{others} is the residual term. The harmonic term C_h is expressed by using the measured Debye temperature θ_D as follows:

$$C_h = 3nRD\left(\theta_D / T\right), \qquad (2.26)$$

where n is the number of atoms per molecule, R is the gas constant, and $D(\theta_D/T)$ is the Debye function. The lattice dilatational term C_d can be calculated from the volumetric thermal expansion coefficient α_V and compressibility β as follows:

$$C_d = \frac{\alpha_V{}^2 V_m T}{\beta}, \qquad (2.27)$$

where V_m is the molar volume and T is the absolute temperature. For an isotropic medium, α_V equals $3\alpha_l$. The values of C_h and $C_h + C_d$ estimated

from the equations given above are shown in Fig. 2.11(b). In Fig. 2.11(b), the solid line represents the fitting result of the experimental C_p data, the dashed line represents C_h obtained from Eq. (2.26), and the dash-dot line represents $C_h + C_d$, in which C_d was obtained from Eq. (2.27). It can be seen from Fig. 2.11(b) that the experimentally obtained result is consistent with the estimated $C_h + C_d$, indicating that the contribution of C_{others} is small in this case. The peaks from the phase transitions were not observed in the C_P curves of $SrRuO_3$ and $SrHfO_3$. The value of the pure perovskites data was similar with published data [43,71], but the solid solution of molybdate looks slightly higher than other perovskites. In this study, the result of the heat capacity data was used in estimating thermal conductivity. The temperature dependence of the thermal diffusivity and the thermal conductivity of the perovskites on each density are shown in Fig. 2.12. The thermal conductivity λ was calculated from the measured thermal diffusivity D, specific heat capacity C_p and density d using the following relationship,

$$\lambda = DC_p d . \qquad (2.28)$$

The thermal conductivity was corrected to 100% of the theoretical density using Schulz's equation [81],

$$\lambda_M = \lambda_C (1 - C_D)^{-3/2} \qquad (2.29)$$

where C_D is the dispersed phase porosity equal to the fractional porosity, and λ_M and λ_C are the thermal conductivity of the matrix and total conductivity, respectively. The temperature dependence of the thermal conductivity corrected to the theoretical density is shown in Fig. 2.13. Generally, the thermal transport properties of ceramics are influenced by many factors, such as lattice defects, grain boundaries, and pores. These factors reduce the thermal conductivity. In the present study, the oxygen vacancy which plays a role as a phonon-scattering center and reduces the lattice thermal conductivity was existed in $SrVO_3$ slightly higher than other perovskites. The relatively high thermal conductivity is attributed to the simple cubic structure with the light component element, and to the contribution of the

electrical thermal conductivity. The thermal conductivity of most perovskites, with the exception of $SrRuO_3$, decreases with increasing temperature. On the other hand, the thermal conductivity of $SrRuO_3$ increases with increasing temperature, and molybdates have very high thermal conductivity, which indicates that the electronic contribution is predominant (See chapter 2.3.1.4.). The relationship between the thermal conductivity at room temperature and tolerance factor is shown in Fig. 2.14. Figure 2.14 shows liner correlation in each Sr, Ba series, because the phonon conductivity is depent on the crystal symmetry. Figure 2.15 shows the temperature dependence of thermal resistivity for perovskites. The result indicates that the phonon conduction is predominant in the thermal conduction of most low thermal conductivity perovskites.

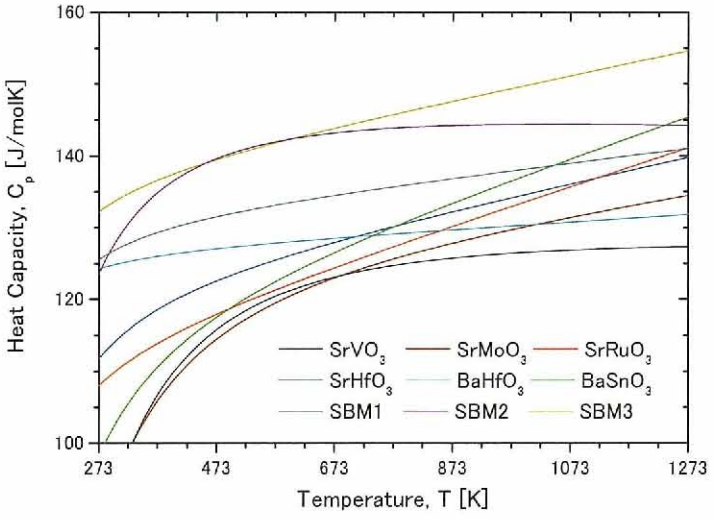

Fig. 2.10 Temperature dependence of heat capacity for perovskite type oxide

Table 2.7 Coefficient of heat capacity ($C_p = A + BT + C/T^2$)

Sample	A	B	C
$SrVO_3$	132	-2.00 E-03	-3.42 E+06
$SrMoO_3$	121	1.19 E-02	-2.73 E+06
$SrRuO_3$	108	2.65 E-02	-5.19 E+05
$SrHfO_3$	118	1.76 E-02	-8.18 E+05
SBM1	129	9.76 E-03	-4.47 E+05
SBM2	150	-3.23 E-03	-1.87 E+06
SBM3	134	1.68 E-02	-4.37 E+05
$BaSnO_3$	112	2.74 E-02	-1.55 E+06
$BaHfO_3$	126	4.99 E-03	-2.01 E+05

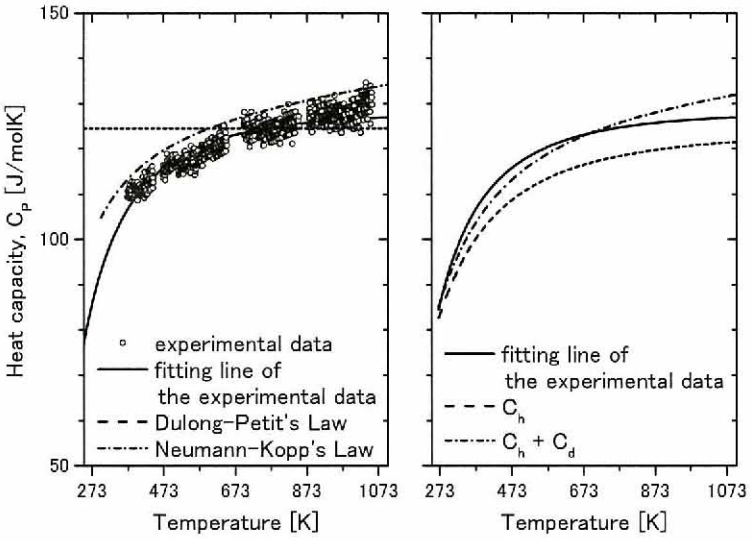

Fig. 2.11 Temperature dependence of the heat capacity of $SrVO_{3-\delta}$

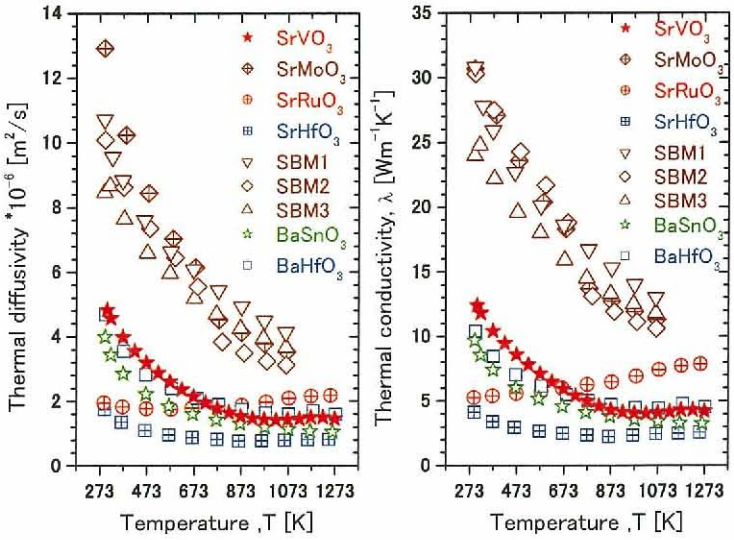

Fig. 2.12 Temperature dependence of thermal diffusivity and thermal conductivity of perovskites on each density.

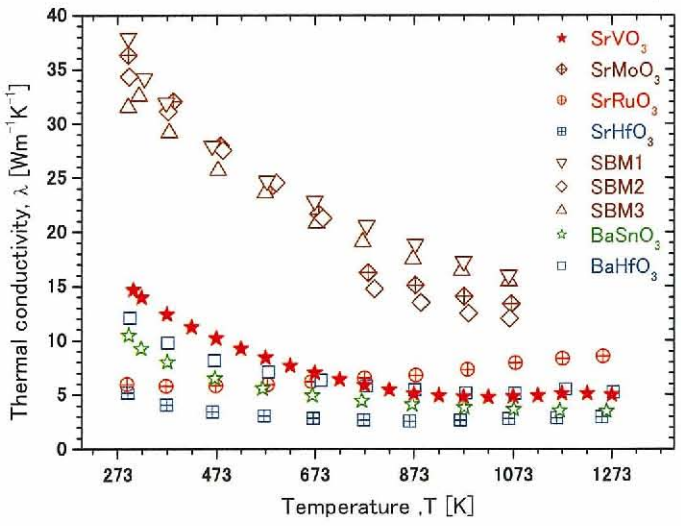

Fig. 2.13 Temperature dependence of thermal conductivity of perovskites corrected to the theoretical density

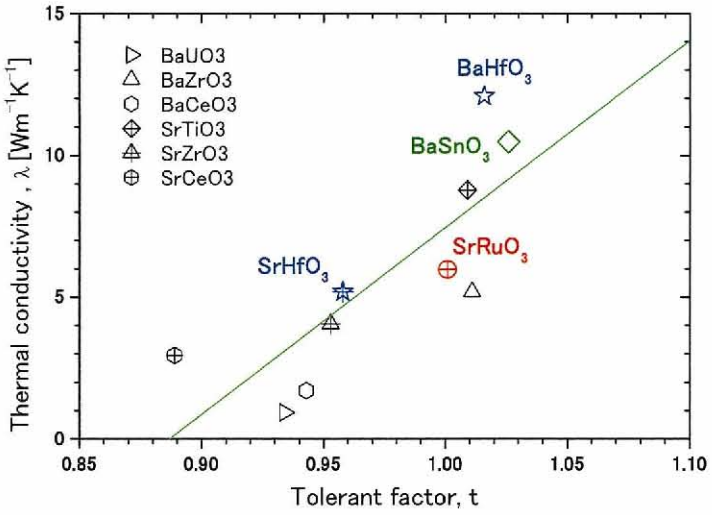

Fig. 2.14 Relationship between λ and t for perovskite type oxides

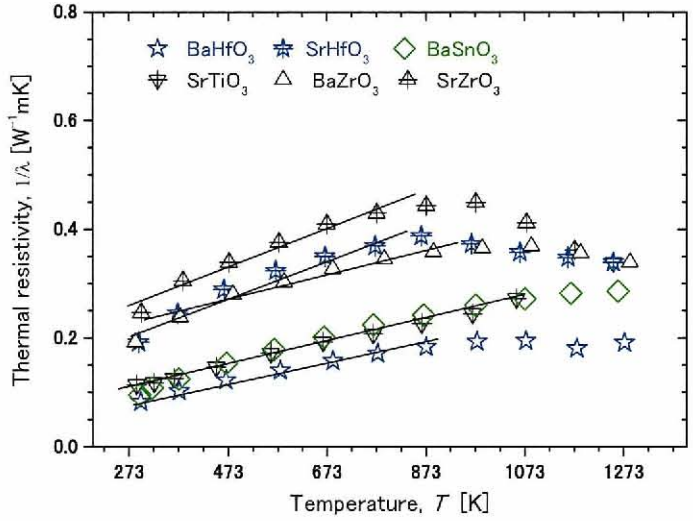

Fig. 2.15 Temperature dependent of 1/λ for perovskite type oxides

The melting temperature T_m of the perovskites is shown in Table 2.6. The melting temperature of $SrRuO_3$ and $SrHfO_3$ is in good agreement with published data [34,82]. The melting temperature of $SrHfO_3$ is higher than

that of other perovskites, for example, the melting temperature of 2170 K [83] for $SrTiO_3$ and that of 2883 K [84] for $SrZrO_3$. In the present study, the melting temperature of $BaHfO_3$ was not evaluated because of the unclear thermal arrest signal, so the reference value [35] is shown in Table 2.6. The melting temperature of $SrVO_3$ is also taken from published data [85]. The relationship between the linear thermal expansion coefficient and melting temperature for the perovskite oxides is shown in Fig. 2.16. In this figure, the data of other perovskite type oxides are plotted for comparison [35,83,84,86-88]. It is confirmed that the linear thermal expansion coefficient varies inversely to the melting temperature for many substances [89].

$$\alpha_l \cdot T_m = 0.019 \quad \text{(for metals)} \tag{2.30}$$

$$\alpha_l \cdot T_m = 0.019 \quad \text{(for perovskite type oxide)} \tag{2.31}$$

$$\alpha_l \cdot T_m = 0.030 \quad \text{(for fluorite type oxides)} \tag{2.32}$$

For the alkaline, Sr, and Ba series perovskite type oxides, the products of α_l and T_m show approximately the same value (= 0.02).

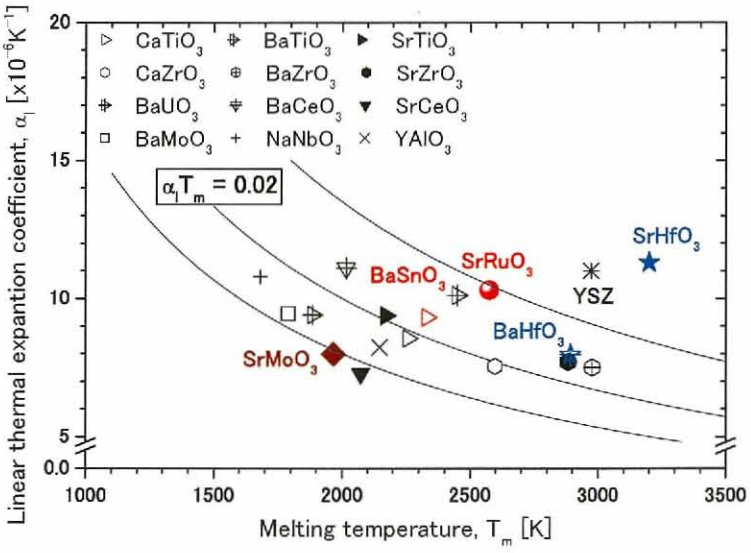

Fig. 2.16 Relationship between α_l and T_m for perovskite type Oxides

2.3.1.4. Electrical properties

Figure 2.22 shows the temperature dependence of the electrical resistivity ρ and the Seebeck coefficient S for $SrVO_3$ together with the published data [102-105]. The electrical resistivity is an order of magnitude of 10^{-4}-10^{-5} (Ωm), and shows positive temperature dependence, indicating metallic behavior. The values of the electrical resistivity determined in the present study are well consistent with the extrapolated data reported by Dougier [102]. However, the values obtained in the present study are lower than the published data [103-105]. It is believed that the sample density and oxygen vacancy have a significant effect on the electrical resistivity. The values of the Seebeck coefficient are negative in the whole temperature range, showing that the majority of charge carriers are electrons. The value of the Seebeck coefficient at room temperature obtained in the present study is in good agreement with the Dougier's result [102], which is consistent with the results of the electrical resistivity. The absolute value of the Seebeck coefficient increases when the temperature increases.

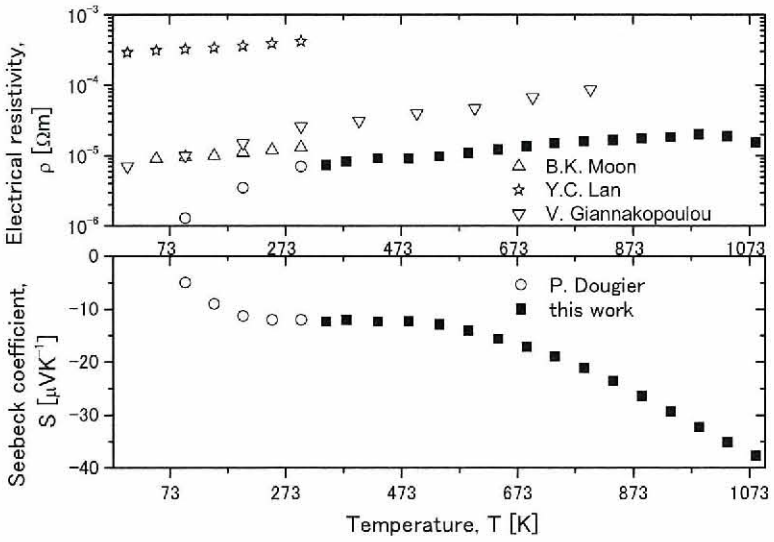

Fig. 2.22 Temperature dependence of the electrical resistivity and Seebeck coefficient for $SrVO_{3-\delta}$ [102-105]

The temperature dependence of the electrical conductivity is shown in Fig. 2.23, together with the data of $BaMoO_3$ [106]. The values of the electrical conductivity of most perovskites, with the exception of the SBM3, are an order of magnitude of 10^5 ($\Omega^{-1}m^{-1}$). It is well known that the total thermal conductivity κ_{total} of solids can be written as follows:

$$\kappa_{total} = \kappa_{lat} + \kappa_{el} \cdots \quad (2.45)$$

where κ_{lat} is the lattice contribution and κ_{el} is the electronic contribution. κ_{el} can be calculated using the Wiedemann-Franz-Lorenz relation:

$$\kappa_{el} = L\sigma T \quad (2.46)$$

where L is the Lorenz number, σ is the electrical conductivity, and T is the absolute temperature. κ_{lat} is obtained by subtracting κ_{el} from κ_{total}. Variations of κ_{total}, κ_{lat}, and κ_{el} of $SrRuO_3$ and $SrMoO_3$ with temperature are shown in Fig. 2.24-25. As can be seen in this figure, the κ_{el} of $SrRuO_3$ is about 40% of the κ_{total} at room temperature, and it increases gradually when temperature increases. On the other hand, the κ_{el} of $SrMoO_3$ is about 20% of the κ_{total} at room temperature and it decreases gradually when temperature increases. The κ_{el} of $SrVO_3$ is approximately 10% of the κ_{total} at room temperature, and it increases gradually when temperature increases. At 1073 K, the κ_{el} of $SrVO_3$ is approximately 35% of the κ_{total}. The temperature dependence of the Seebeck coefficient S is shown in Fig. 2.26, together with the published data of $BaMoO_3$ [106]. The Seebeck coefficient of $SrMO_3$, $SrRuO_3$, and SBM1 is positive in the whole temperature range, showing that the majority of charge carriers are holes. The values of the Seebeck coefficient of $SrRuO_3$ are around 30-40 μVK^{-1} in the whole temperature range. On the other hand, the Seebeck coefficient of SBM2 and SBM3 is negative, showing that the majority of charge carriers are electrons. The values of the Seebeck coefficient are around -30 μVK^{-1}. In addition, the color of the surface of the molybdate sample was changed after the measurement. It seems that the sample was oxidized above 800 K.

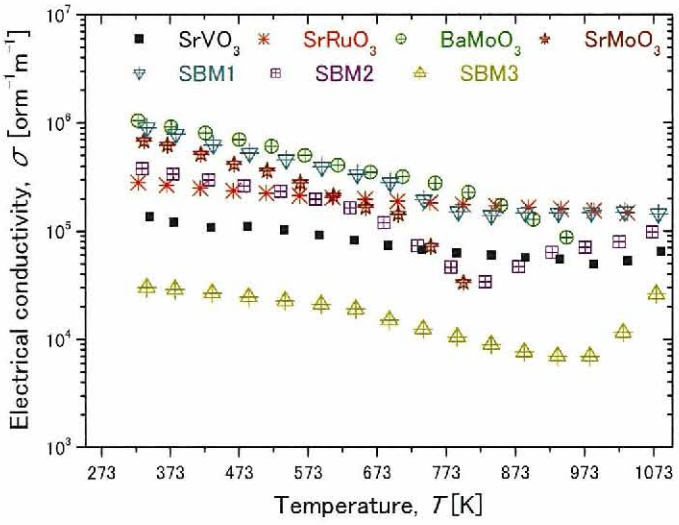

Fig. 2.23 Temperature dependence of the electric conductivity of perovskite type oxides

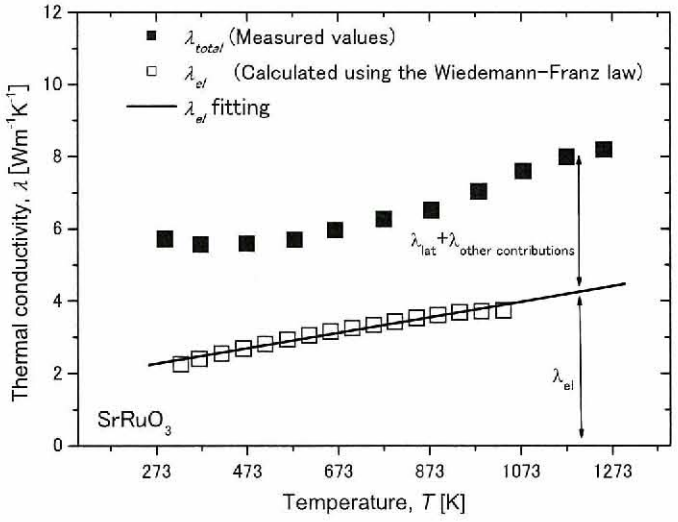

Fig. 2.24 Temperature dependence of the λ_{total}, λ_{lat}, and λ_{el}

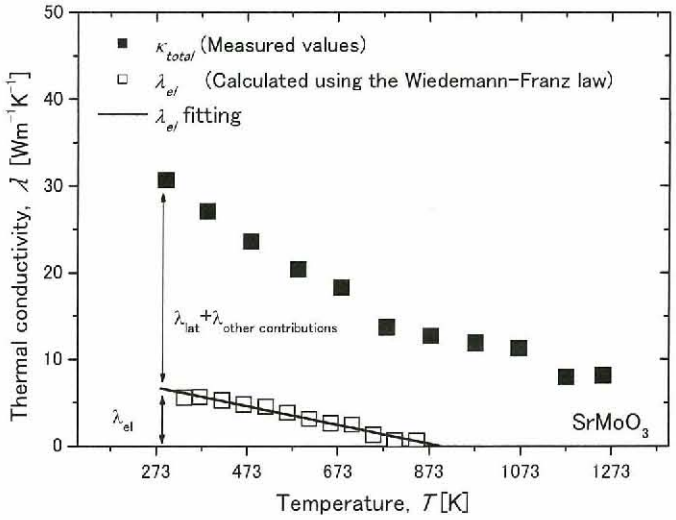

Fig. 2.25 Temperature dependence of the λ_{total}, λ_{lat}, and λ_{el}

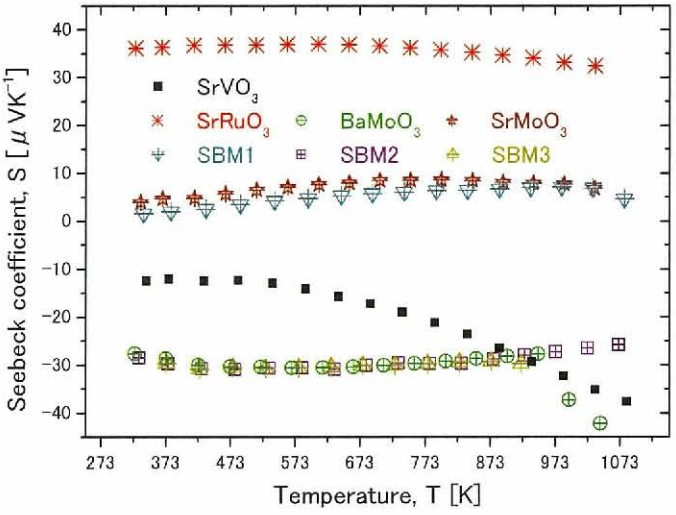

Fig. 2.26 Temperature dependence of the Seebeck coefficient for perovskite type oxides

2.3.1.5. Thermoelectric properties

The temperature dependence of the electrical resistivity ρ for perovskites is shown in Fig. 2.27, together with the data of other substances [106-110]. The values of the electrical resistivity of $SrRuO_3$, $SrMoO_3$, SBM1, SBM2, SBM3, and $BaMoO_3$ are respectively of an order of magnitude of 10^{-4} and 10^{-6} (Ωm), which is about same as that of state-of-the-art thermoelectric materials, such as Bi_2Te_3 and TAGS "$(GeTe)_{1-x}(AgSbTe_2)_x$" [107,110]. The electrical resistivity of the perovskites shows positive temperature dependence, indicating metallic behavior. The temperature dependence of electrical resistivity is changed at about 800 K. In addition, the color of the $SrMoO_3$ sample surface is changed after the measurement. It seems that the sample is oxidized above 800 K. The author had hope that alkaline molybdate solid solutions would have the equal electric resistivity compared with that of $BaMoO_3$. However $BaMoO_3$ performed the best because of it had the lowest electric resistivity.

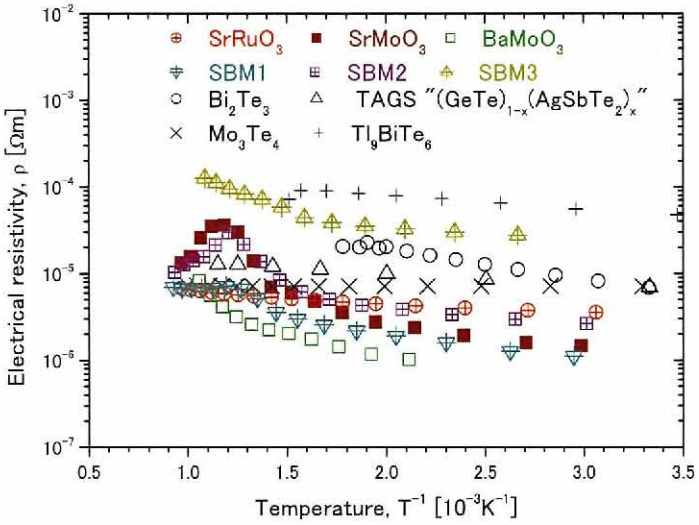

Fig. 2.27 Temperature dependence of the electrical resistivity for perovskites

The temperature dependence of the Seebeck coefficient S for perovskites is shown in Fig. 2.28, together with the data of other substances [106-110]. The Seebeck coefficient of $SrRuO_3$ and $SrMoO_3$ is positive in the whole temperature range, showing that the majority of charge carriers are holes. The Seebeck coefficient of $BaMoO_3$ is negative in the whole temperature range, showing that the majority of charge carriers are electrons. The values of the Seebeck coefficient of $SrRuO_3$, $SrMoO_3$, and $SrMoO_3$ are respectively around 30-40 μVK^{-1}, 30 μVK^{-1}, 4-9 μVK^{-1} in the whole temperature range, like metals. The value of the Seebeck coefficient is lower than those of state-of-the-art thermoelectric materials. Figure 2.29 shows the relationship between the electrical conductivity σ and Seebeck coefficient S of perovskites and other materials [107-110]. This figure gives an indication of the power factor $S^2\sigma$ (See Fig. 2.30.), which defines the electrical performance of the thermoelectric materials. It is known that the power factor is required to have an order of magnitude ($Wm^{-1}K^{-2}$) of about 10^{-3} for the materials used in the current devices. The maximum value of the power factor of $SrRuO_3$ is 4.0×10^{-4} $Wm^{-1}K^{-2}$ at around room temperature. On the other hand, making a solid solution rather lowered the value in the molybdate. The values of the power factor of $BaMoO_3$ do not reach the order of magnitude of 10^{-3}. The maximum value of the power factor of $BaMoO_3$ is about 8×10^{-4} $Wm^{-1}K^{-2}$ at around room temperature.

The temperature dependence of the thermal conductivity for perovskites is shown in Fig. 2.31, together with the published data of other substances [107-110]. The thermal conductivity of $SrRuO_3$ increases when temperature increases. On the other hand, the thermal conductivity of molybdates, such as $SrMoO_3$, SBM1, SBM2, SBM3, and $BaMoO_3$ decreases when temperature increases. At room temperature, it is high compared with that of state-of-the-art thermoelectric materials [107,110]. In molybdates, making a solid solution did not succeed in decreasing of the thermal conductivity. The dimensionless figure of merit ZT for perovskites

has been evaluated using the data of the electrical resistivity, Seebeck coefficient, and thermal conductivity. The ZT of $BaMoO_3$ is lower than those of state-of-the-art p-type thermoelectric materials, which is caused by the extremely high thermal conductivity. The maximum value of the thermoelectric figure of merit ZT is 0.015 at around 470 K. In order to utilize $BaMoO_3$ as an actual thermoelectric module, it is necessary to reduce the thermal conductivity. On the other hand, the ZT of $SrRuO_3$ is also lower than those of state-of-the-art p-type thermoelectric materials, which is caused by the low Seebeck coefficient and high thermal conductivity. The maximum value of the thermoelectric figure of merit ZT is 0.03 at around 573-773 K. In order to utilize $SrRuO_3$ as an actual thermoelectric module, it is necessary to optimize the carrier concentration and reduce the thermal conductivity.

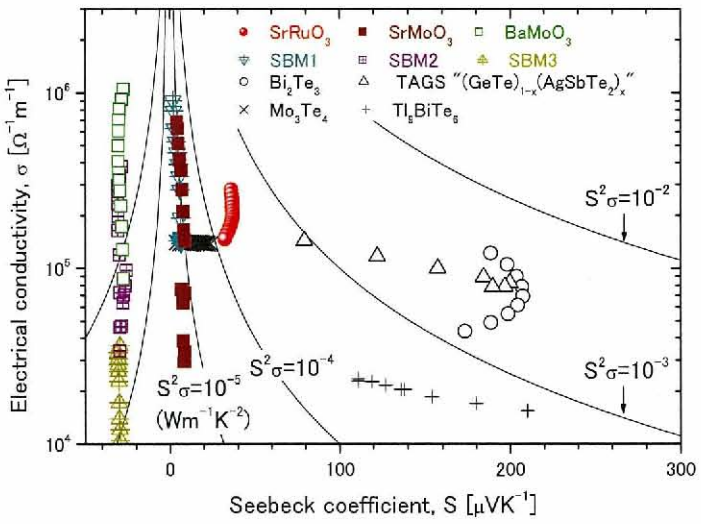

Fig. 2.29 Relationship between σ and S of perovskites.

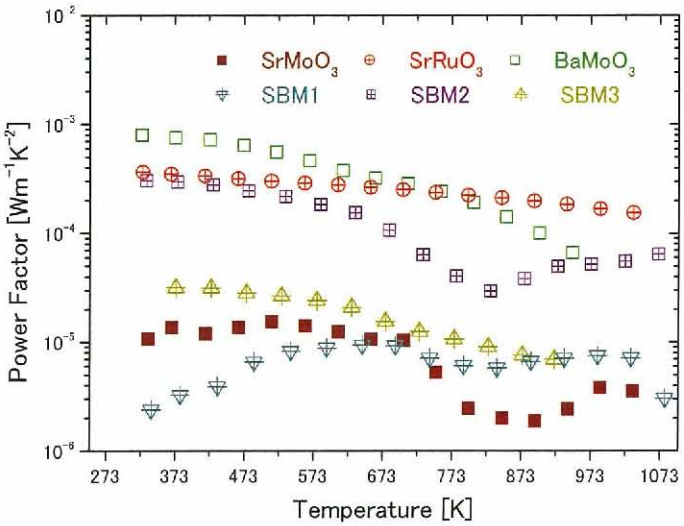

Fig.2.30 Temperature dependence of power factor for perovskites.

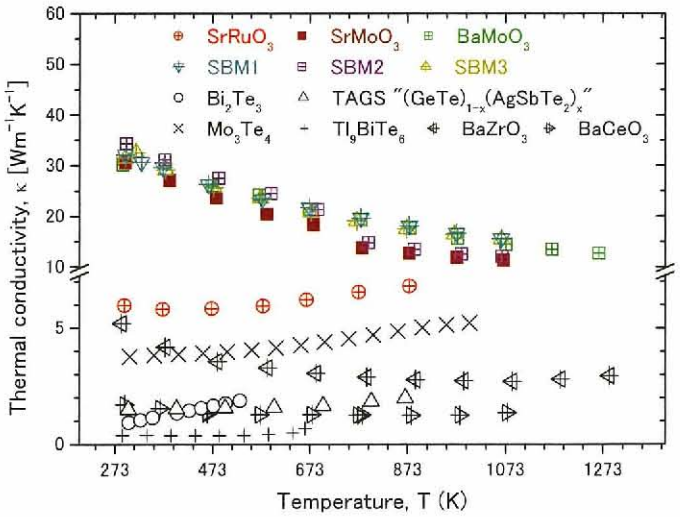

Fig. 2.31 Temperature dependence of the thermal conductivity for perovskites.

2.3.2. Alkaline earth and Yttrium oxides

2.3.2.1. Crystallography characteristics

From the powder XRD patterns of the samples at room temperature (Fig. 2.32), two results were obtained in the present study: the single phase of BaY_2O_4 with the crystal structure of space group *Pnab* [111], and SrY_2O_4, which indicates a single-phase isomorphous with the space group of Pnam [59,64]. The lattice parameters of BaY_2O_4 and SrY_2O_4 at room temperature evaluated from the XRD pattern are a = 1.0396 nm, b = 1.2113 nm, c = 0.3450 nm, and a = 1.0090 nm, b = 1.1901 nm, c = 0.3412 nm, respectively. The values of the lattice parameter were consistent with published data [111,112,113]. The sample bulk densities of BaY_2O_4 and SrY_2O_4 were approximately 88% and99 % of the theoretical X-ray density. On the other hand, the lattice parameter of $Ba_3Y_4O_9$ was evaluated from the XRD pattern to be a = 0.6117 nm, c = 2.5207 (Fig. 2.32). The values of the lattice parameters are in agreement with the published data [114]. The sample density of $Ba_3Y_4O_9$ was about 67 % of the theoretical density. The chemical composition determined by the EDX analysis does not deviate from the stoichiometric ratio. The sintered samples of SrY_2O_4, BaY_2O_4 and $Ba_3Y_4O_9$ show a white color. The sample characteristics of SrY_2O_4, BaY_2O_4 and $Ba_3Y_4O_9$ are summarized in Table 2.8.

Table 2.8 Sample characteristics and thermophysical properties

at R.T.			BaY_2O_4	SrY_2O_4	$Ba_3Y_4O_9$
Crystal system			Orthorhombic	Orthorhombic	Hexagonal
Lattice parameter	[nm]	a	1.0396	1.0090	0.6117
	[nm]	b	1.2113	1.1901	
	[nm]	c	0.3450	0.3412	2.5206
Relative density	[%T.D.]		88	99	67

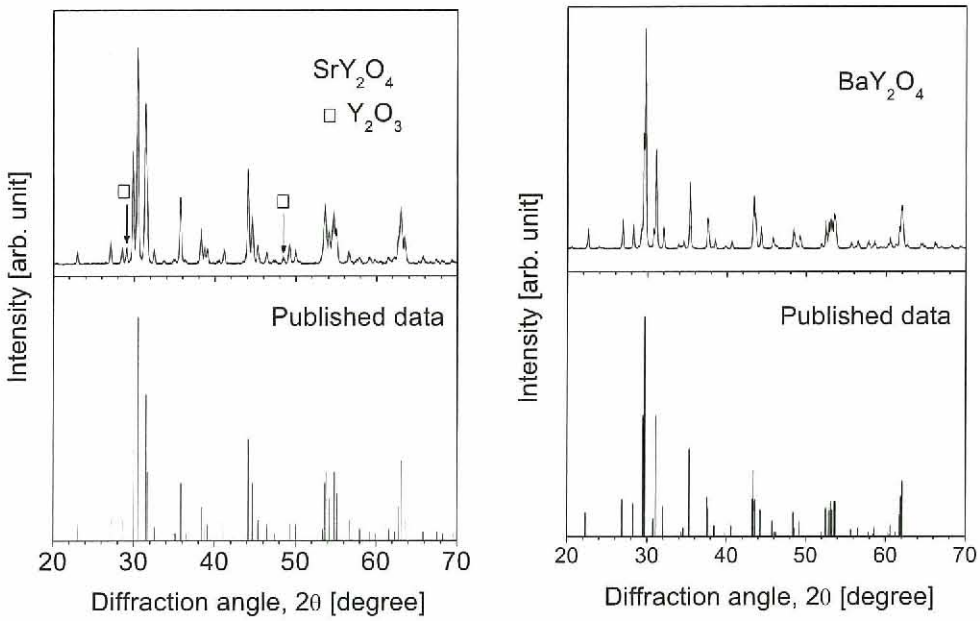

Fig. 2.32 XRD patterns of SrY_2O_4 and BaY_2O_4 [112,113]

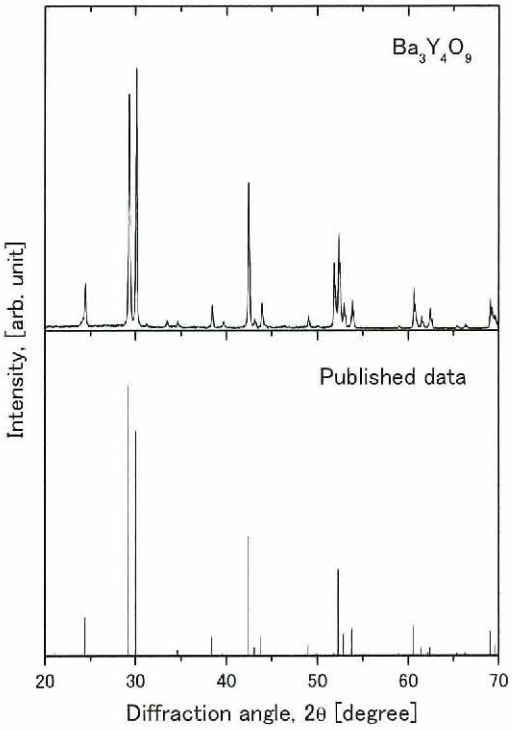

Fig. 2.33 XRD patterns of $Ba_3Y_4O_9$ [114]

Figure 2.34 shows the temperature dependences of unit cell parameters *a*, *b*, *c*, and volume *V* of SrY_2O_4 in the orthorhombic structure. All parameters increase smoothly with increasing temperature. The obvious phase transitions are not observed with HT-XRD analysis. The temperature dependences of lattice parameters can be expressed as a linear function of temperature. Between room temperature and 1273 K, the linear and volumetric thermal expansion coefficients (α_a, α_b, α_c, α_V, α_L) can be calculated as follows:

$$\alpha_a = \frac{1}{a_0}\left(\frac{\partial a(T)}{\partial T}\right)_P \quad (2.46)$$

$$\alpha_b = \frac{1}{b_0}\left(\frac{\partial b(T)}{\partial T}\right)_P \quad (2.47)$$

$$\alpha_c = \frac{1}{c_0}\left(\frac{\partial c(T)}{\partial T}\right)_P \quad (2.48)$$

$$\alpha_V = \frac{1}{V_0}\left(\frac{\partial V(T)}{\partial T}\right)_P \quad (2.49)$$

$$\alpha_L = \frac{1}{3}\alpha_V \quad (2.50)$$

where a_0, b_0, c_0, and V_0 are the lattice parameters at room temperature and *T* is in Kelvin. α_L is the average linear thermal expansion coefficient, which equals to one-third of α_V. These results are summarized in Table 2.9. It is found that the linear thermal expansion coefficient in a direction α_a is larger than those in b and c in directions α_b and α_c. The average linear thermal expansion coefficient α_L is 10.9×10^{-6} K^{-1} in the temperature range from 300 to 1273 K.

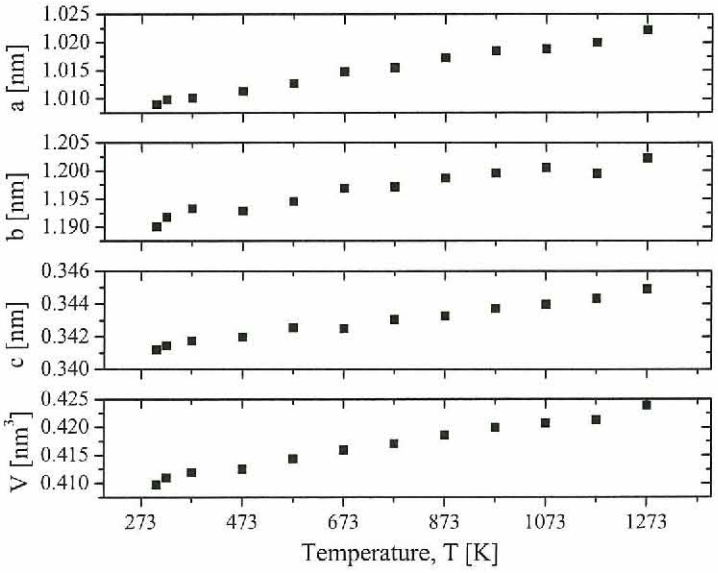

Fig. 2.34 Temperature dependence of the lattice parameters of SrY_2O_4

Table 2.9 Thermal expansion coefficients of SrY_2O_4

Linear thermal expansion coefficient (300 – 1273 K)	α_a [K^{-1}]	12.9×10^{-6}
	α_b [K^{-1}]	9.3×10^{-6}
	α_c [K^{-1}]	10.2×10^{-6}
Volumetric thermal expansion coefficient (300 – 1273 K)	α_V [K^{-1}]	32.8×10^{-6}
Average linear thermal expansion coefficient (300 – 1273 K)	α_L [K^{-1}]	10.9×10^{-6}

Figure 2.35 shows the thermal expansion behavior of BaY_2O_4 and SrY_2O_4. The lattice of the samples increases with temperature, indicating a positive thermal expansion in Fig. 2.35 (a). The linear thermal expansion coefficient increases with temperature as shown in Fig. 2.35 (b). The linear thermal expansion coefficient α_l can be calculated from the following equation using the measured thermal expansion:

$$\alpha_l = \frac{\partial a}{\partial T} \cdot \frac{1}{a_{298}}. \qquad (2.51)$$

The average linear thermal expansion coefficient α_l of BaY_2O_4 is 1.08 x 10^{-5} K^{-1} in the temperature range from 300 K to 1000 K. The average linear thermal expansion coefficient measured by a dilatometer in the temperature range between 300 and 1773 K is 10.7×10^{-6} K^{-1}, which is consistent with the HT-XRD analysis result (1.09 x 10^{-5} K^{-1}). These values are relatively larger than those of typical ceramic materials (for example 8.5 x 10^{-6} K^{-1} for Al_2O_3 at 298 K, 10 x 10^{-6} K^{-1} for YSZ, 9.7 x 10^{-6} K^{-1} for $SrZrO_3$ [85], and 9.1 x 10^{-6} K^{-1} for $La_2Zr_2O_7$ [115] from R.T. to 1273 K). The melting temperature of SrY_2O_4 determined by the thermal arrest method is 2413 K, which is slightly lower than that in published data [111]. The relationship between the liner thermal expansion coefficient and the melting temperature of SrY_2O_4 is shown in Fig. 2.36. In the figure, the data of other substances are plotted for comparisons. From this figure, it is confirmed that SrY_2O_4 has a moderate high thermal expansion coefficient as well as a moderate high melting temperature, compared with those of the typical oxide ceramics.

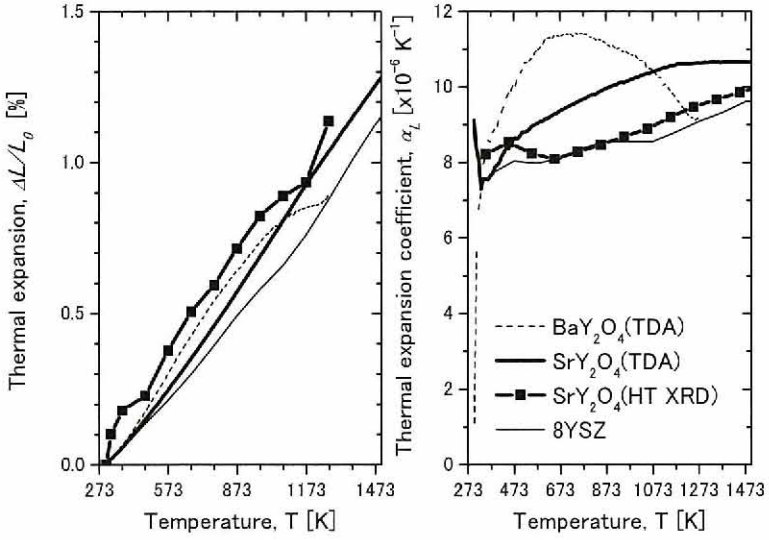

Fig. 2.35 Temperature dependence of the thermal expansion (a) and linear thermal expansion coefficient (b) from 300 to 1773 K for SrY_2O_4 and 8YSZ.

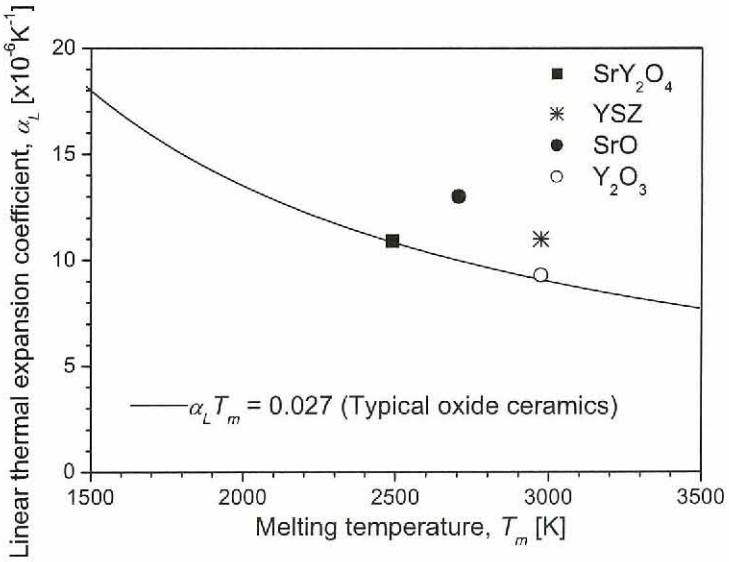

Fig. 2.36 Relationship between the linear thermal expansion coefficient and melting temperature for SrY_2O_4.

2.3.2.2. Mechanical properties

The values of the physical properties, such as elastic moduli and Debye temperature of BaY_2O_4 and SrY_2O_4, obtained in the present study are summarized in Table 2.10. It was observed that the values of mechanical properties for BaY_2O_4 are lower than those of SrY_2O_4. One of the reasons for this is the low sample density of BaY_2O_4. It is necessary to prepare a higher density sample of BaY_2O_4 in order to consider the characteristics in more detail because the physical properties are significantly affected by pores in the sample. The following relationship has been proposed to present the porosity dependence of the modulus:

$$M = M_0\left(1 - bP + cP^2\right), \qquad (2.55)$$

where M is the modulus at porosity P, M_0 is the zero-porosity modulus, and b and c are adjustable geometry parameters [117]. At sufficiently small porosity with the same value for b, the modulus can be shown as:

$$M = M_0\left(1 - bP\right), \qquad (2.56)$$

because cP^2 in Eq. (2.55) can be omitted. Young's moduli of SrY_2O_4 and BaY_2O_4 corrected to those with 100 %T.D. using $b = 2.9$ [119] (in which there are 16 data sets for 11 oxides) are 166 and 167 GPa, respectively. Those values are lower than those of the candidates, such as 269 GPa for $SrZrO_3$ [85], 245 GPa for ZrO_2 and 200 GPa for YSZ.

Table 2.10 Sample characteristics and thermophysical properties

			SrY_2O_4	BaY_2O_4	$Ba_3Y_4O_9$
Crystal system at R.T.			Orthorhombic	Orthorhombic	Hexagonal
Lattice parameter at R.T.	[nm]	a	1.0090	1.0396(4)	0.6117
	[nm]	b	1.1901	1.2112(8)	
	[nm]	c	0.3412	0.3450(2)	2.5206
Relative density	[%T.D.]		99	88	67
Average linear thermal expansion coefficient	[K^{-1}]	α_l	1.09 x 10^{-5}	1.08 x 10^{-5}	-
Longitudinal wave velocity	[m/s]	V_L	6175	5086	3856
Transverse wave velocity	[m/s]	V_S	3479	2901	2165
Young's modulus	[GPa]	E	162	108	77
Shear modulus	[GPa]	G	64	43	31
Compressibility	[GPa^{-1}]	β	8.61 x 10^{-3}	13.4 x 10^{-3}	2.42 x 10^{-2}
Debye temperature	[K]	θ_D	471	351	307
Vickers hardness	[GPa]	H_V	9.2 ±1.3	3.2 ±0.3	2.3
Thermal conductivity at R.T.	[$Wm^{-1}K^{-1}$]	κ	7.6 ±0.2	3.9 ±0.1	1.4

*The elastic modulii and Debye temperature are within 1 % uncertainty.

2.3.2.3. Thermal properties

The temperature dependence of the heat capacity of SrY_2O_4 obtained by the scanning method using the triple-cell DSC is shown in Fig. 2.37. The peaks from the phase transitions are not observed in the C_P curve of SrY_2O_4. In the temperature range between 300 and 1273 K, the empirical equation

for the C_P of SrY_2O_4 was determined by the experimental result as follows:

$$C_P = 186.6 - 0.0312T + 3.00\times10^{-5}T^2 - 2.51\times10^{-6}T^{-2} \quad (JK^{-1}mol^{-1}). \qquad (2.52)$$

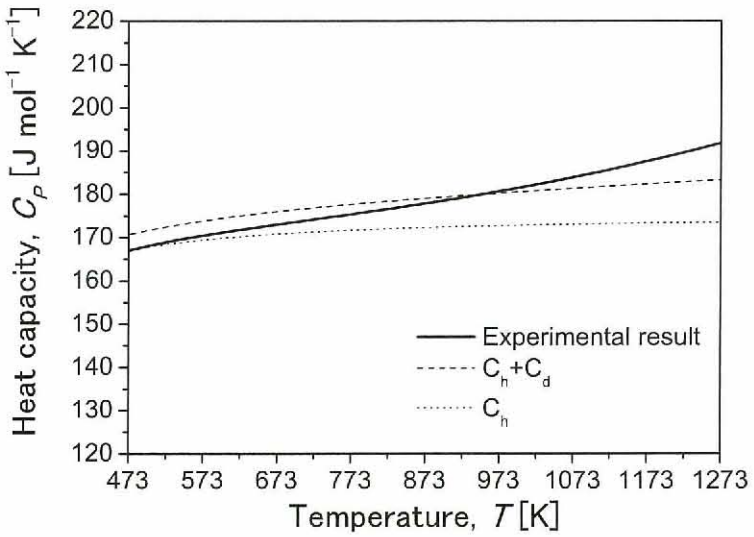

Fig. 2.37 Temperature dependence of the heat capacity of SrY_2O_4

The heat capacity at constant pressure C_P can be evaluated from the following relationship:

$$C_P = C_h + C_d + C_{others}, \qquad (2.53)$$

where C_h is the harmonic term, C_d the lattice dilatational term, and C_{others} the residual term. The harmonic term, C_h is expressed by using the Debye temperature, θ_D, as follows:

$$C_h = 3nRD\left(\frac{\theta_D}{T}\right), \qquad (2.54)$$

where n is the number of atoms per molecule, R the gas constant and $D(\theta_D/T)$ the Debye function. The lattice dilatational term C_d can be calculated from the linear thermal expansion coefficient α_L and compressibility β as follows:

$$C_d = \frac{(3\alpha_L)^2 V_m T}{\beta}, \qquad (2.55)$$

where V_m is the molar volume. The temperature dependencies of C_h and (C_h + C_d) of SrY_2O_4 is shown in Fig. 2.37. It was confirmed that the C_P of SrY_2O_4 measured by the DSC almost equals (C_h + C_d), while the other contribution appears around above 900 K.

The temperature dependences of the thermal diffusivity and thermal conductivity of BaY_2O_4 and SrY_2O_4 are shown in Fig. 2.38. The thermal conductivity of SrY_2O_4 was evaluated from the thermal diffusivity, heat capacity, and density. The thermal conductivity of BaY_2O_4 was evaluated from the thermal diffusivity, and the heat capacity was evaluated with Kopp-Neumann's law [116] using the heat capacities of BaO and Y_2O_3 [117], and the density of BaY_2O_4. The thermal conductivity of BaY_2O_4 and SrY_2O_4 is 3.9 $Wm^{-1}K^{-1}$ and 7.2 $Wm^{-1}K^{-1}$ at 300 K, respectively. The thermal conductivity decreases when temperature increases and reaches the value of 1.9 $Wm^{-1}K^{-1}$ and 3.4 $Wm^{-1}K^{-1}$ at 1200 K, respectively. This temperature dependence indicates that the phonon conduction is predominant. The thermal conductivity values of BaY_2O_4 are lower than those of SrY_2O_4 in the whole temperature range investigated in the present study. The thermal conductivity was corrected to 100 % of the theoretical density using the modified Bruggeman's equation and ϕ = 3/2,

$$\lambda = \lambda_0 (1-P)^{\phi}, \qquad (2.56)$$

where λ_0 is the zero-porosity thermal conductivity and ϕ is an empirical factor (i.e. ϕ = 2 for spheres, ϕ = 3/2 for closed pores with irregular shapes) [118]. The solid line represents the zero-porosity thermal conductivity of BaY_2O_4 and the dashed line represents the results of SrY_2O_4. Those values for BaY_2O_4 are slightly higher than that of YSZ (2 $Wm^{-1}K^{-1}$ at 1273 K) and $La_2Zr_2O_7$ (1.6 $Wm^{-1}K^{-1}$ at 1273 K) [119] though equivalent to those of $SrZrO_3$ [85]. A much lower thermal conductivity (<2 $Wm^{-1}K^{-1}$) is required to utilize this candidate material for the TBC application.

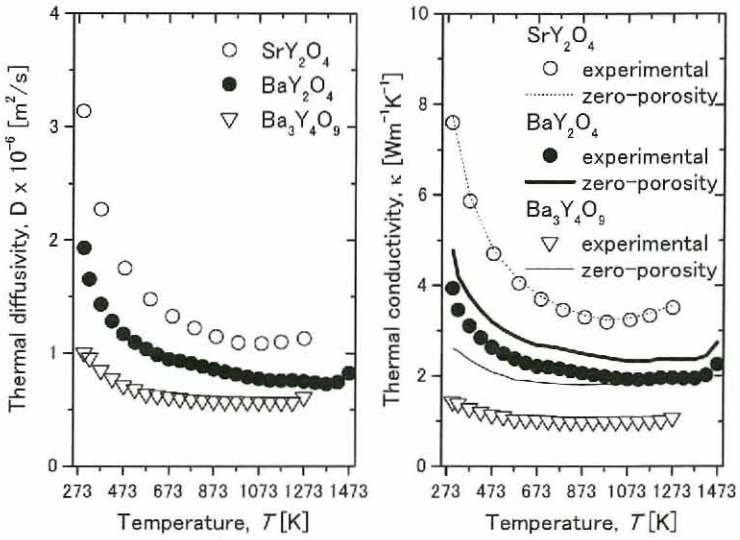

Fig. 2.38 Temperature dependence of (a) thermal diffusivities and (b) thermal conductivities of SrY_2O_4 and BaY_2O_4

BaY_2O_4 has an advantage compared to SrY_2O_4 from the viewpoint of the application for TBC materials, because TBC materials require a low thermal conductivity. Figure 2.38 shows that the thermal conductivity of BaY_2O_4 is obviously lower than that of SrY_2O_4. Generally, it is known that the presence of heavy atoms in the molecule reduces the thermal conductivity. Thus the difference between the thermal conductivity of BaY_2O_4 and SrY_2O_4 is due to the difference in the atomic weight between Ba and Sr. However it is not clear if BaY_2O_4 or SrY_2O_4 can be an alternative material to YSZ in the TBC application. Apparently, BaY_2O_4 shows equivalent properties to YSZ, such as a low thermal conductivity and a large thermal expansion. In addition, BaY_2O_4 is difficult to sinter, so this characteristic of the sintering resistance is an advantage to utilize the material as the TBC application. However materials used as the TBCs should have a combination of good thermal properties, good mechanical toughness, and good film characteristics. Therefore, it is contemplated that

further research is necessary to decide that whether BaY_2O_4 would be an advanced TBC material or not.

2.4. Material selection guidelines for low thermal conductivity materials

The systematic interests have possibilities to be applications of their properties in different branches of new engineering. Therefore the research of the thermophysical properties on material science is important and needed to contribute to the development of society. However it is also a fact that it takes too long to understand the properties because there are so many materials which have multielement compositions. For the screening of the candidate materials with low thermal conductivity, material selection was suggested by Clarke [120]. Generally, the thermal conductivity of a dielectric can be lowered toward its theoretical minimum by increasing the size of the unit cell, the presence of heavy atoms, amorphization, random atomic substitution, increased optic-acoustic coupling, and increasing the lattice symmetry [121]. The concept of a minimum thermal conductivity is a useful guideline to design materials with low thermal conductivity. A perfect harmonic crystal has no thermal resistance mechanism. Therefore the perfect harmonic crystal has infinite thermal conductivity. It is worth considering the lower limit of the thermal conductivity [122]. The minimum thermal conductivity can be expressed as, [123]

$$\kappa_{\min} = \left(\frac{\pi}{6}\right)^{1/3} k_B n^{2/3} \sum_i v_i \left(\frac{T}{\theta_i}\right)^2 \int_0^{\theta_i/T} \frac{x^3 e^x}{\left(e^x - 1\right)^2} dx . \qquad (2.57)$$

where, κ_{min} is the minimum thermal conductivity, k_B is the Boltzmann constant, n is the number density of atoms, v_i is the speed of sound, T is temperature, and θ_i is the cutoff frequency for each polarization expressed in degrees K. Using, approximations, the minimum thermal conductivity can be expressed as, [120]

$$\kappa_{\min} \to 0.87 k_B N_A^{2/3} \frac{m^{2/3} \rho^{1/6} E^{1/2}}{M^{2/3}}. \tag{2.58}$$

where, N_A is the Avogadro number, m is the number of atoms in the molecule, ρ is the density of the crystal structure, E is the value of Young's modulus, and M is the atomic weight of the molecule. The Debye temperature can be expressed as, [120]

$$\theta_D = 3.39 \frac{\hbar}{k_B} N_A^{1/3} \frac{m^{1/3} E^{1/2}}{M^{1/3} \rho^{1/6}}. \tag{2.59}$$

The values with no porosity evaluated from the above formulas are summarized in Table. 2.11. Figure 2.39 shows the comparison of normalized thermal conductivity versus normalized temperature for the oxide materials obtained in the present study. The measured thermal conductivity data in the present study was normalized to divide with the calculated minimum thermal conductivity. The temperature was also normalized to divide with the calculated Debye temperature. At the normalized temperature in excess of around 1.5, all the data becomes constant with the exception of $SrRuO_3$. It seems the electric conductivity affects the normalized temperature, as $SrRuO_3$ has ten times higher conductivity than $SrVO_3$. The normalized thermal conductivity of most materials reached excess values of around 2 at high temperature. In the selection process, the parameter does not include the combinations of thermal conductivity from the optical modes whose number increases as the number of atoms per unit cell increases. Therefore, the minimum thermal conductivity is estimated as a lower value than in reality. The accuracy is not good, but most materials show the same tendency of thermal conductivity. Therefore the concept of minimum thermal conductivity may help the screening process for the insulate candidate materials with low thermal conductivity. However it is fact that a new concept with no use of experimental data, such as elastic property, is needed.

Table 2.11 Caluculated minimum thermal conductivity and Debye temperatures for oxide materials

	K_{min} [W/mK]	θ_D [K]
$SrVO_3$	1.63	792
$SrMoO_3$	1.40	702
$SrRuO_3$	1.18	586
$SrHfO_3$	1.30	652
SBM1	1.29	650
SBM2	1.28	647
SBM3	1.27	644
$BaSnO_3$	1.29	670
$BaHfO_3$	1.15	559
SrY_2O_4	1.13	597
BaY_2O_4	1.08	581
$Ba_3Y_4O_9$	0.76	531

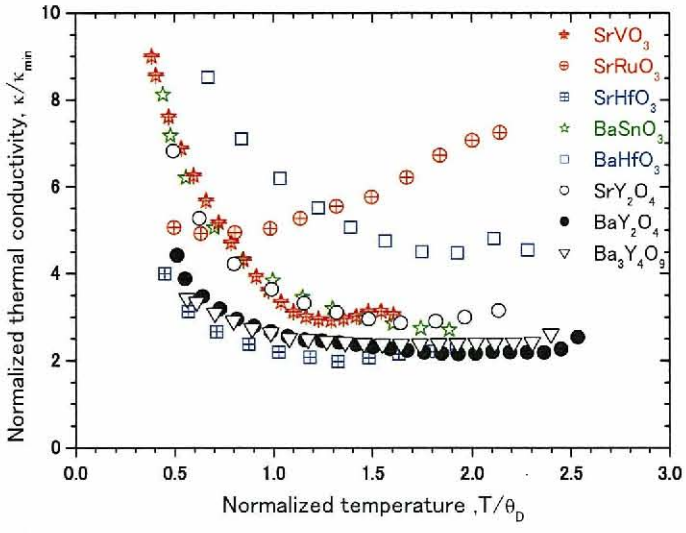

Fig. 2.39 Comparison of normalized thermal conductivity versus normalized temperature for the oxide materials obtained in the present study

2.5. Summary

In this study, thermophysical properties of Sr and Ba series perovskite type oxides and alkaline earth and yttrium oxide materials on bulk were systematically evaluated. $SrHfO_3$, $BaSnO_3$, $BaHfO_3$, SrY_2O_4, BaY_2O_4, and $Ba_3Y_4O_9$ show white, $SrVO_3$, $SrFeO_3$, and $SrRuO_3$ show black, and $Sr_{1-x}Ba_xMoO_3$ shows brown colors. In the present study, the phase transitions in $SrRuO_3$ and $SrHfO_3$ were observed from the HT-XRD analysis. $SrRuO_3$ undergoes phase transitions, from orthorhombic (*Pbnm*) to tetragonal (*I4/mcm*) at 800 K, and then transforms into cubic (*Pm3m*) at 950 K. $SrHfO_3$ undergoes phase transitions, from orthorhombic (*Pbnm*) to orthorhombic (*Cmcm*) at 800 K, and then transforms into tetragonal (*I4/mcm*) at 1000 K. On the other hand, the other oxide materials have no phase transition in the whole temperature range. The average linear thermal expansion coefficients α_l are 1.13×10^{-5} K^{-1} for $SrHfO_3$, 1.03×10^{-5} K^{-1} for $SrRuO_3$, 7.98×10^{-6} K^{-1} for $SrMoO_3$, 1.09×10^{-5} K^{-1} for SrY_2O_4, and 1.08×10^{-5} K^{-1} for BaY_2O_4 in the temperature range between 300 K and 1100 K, and 7.97×10^{-6} K^{-1} for $BaHfO_3$ in the temperature range between 300 K and 1500 K. The value of the thermal expansion of $SrHfO_3$ is slight higher than other perovskite type oxides. The peaks from the phase transitions are not observed in the C_P curves of $SrHfO_3$ and $SrRuO_3$.

The thermal conductivity of most perovskites with the exception of $SrRuO_3$ decreases when temperature increases. On the other hand, the thermal conductivity of $SrRuO_3$ increases when temperature increases and molybdates have very high thermal conductivity, which indicates that the electronic contribution is predominant. The melting temperature of $SrHfO_3$ (3200 K) is higher than that of other perovskites. For example, the melting temperature of $SrTiO_3$ is 2170 K, and that of $SrZrO_3$ is 2883 K. For the alkaline, Ba and Sr series perovskite type oxides, the products of α_l and T_m show approximately the same value ($\alpha_l \times T_m = 0.02$). However the thermal expansion value of $SrHfO_3$ is slightly higher than the other perovskites.

The thermal conductivity is dependent on the relation of the tolerance factor. Because it shows a linear correlation in each Sr and Ba series, the phonon conductivity is dependant on crystal symmetry. Low symmetry of crystal structure has a more advantage than a solute effect of heavy ions for the reduction of the thermal conductivity of materials. There are obvious correlations between the tolerance factor and elastic constants. It is considered that the symmetry of a crystal is relevant to inter ionic bonding states, therefore the tolerance factor has affected the elasticity-characteristic of the material.

The electrical resistivity of $SrVO_3$, $SrRuO_3$, and molybdates are respectively of an order of magnitude of 10^{-4} and 10^{-6} Ωm. The electrical resistivity of the perovskites shows positive temperature dependence, indicating metallic behavior. The Seebeck coefficient of $SrRuO_3$ and $SrMoO_3$ is positive, showing that the majority of charge carriers are holes. The Seebeck coefficient of $SrVO_3$ and $BaMoO_3$ is negative, showing that the majority of charge carriers is electron. The Seebeck coefficient values of $SrVO_3$,$SrRuO_3$, $SrMoO_3$, and $SrMoO_3$ are respectively around 10-40 μVK^{-1}, 30-40 μVK^{-1}, 30 μVK^{-1}, 4-9 μVK^{-1}. Making the solid solution rather lower than the value in molybdate. The thermal conductivity of $SrRuO_3$ increases when temperature increases. On the other hand, the thermal conductivity of molybdates decreases when temperature increases. In molybdates, making a solid solution did not succeed in the decrease of the thermal conductivity. The maximum value of the ZT in molybudates is 0.015 on $BaMoO_3$ at around 470 K. The maximum value of the ZT obtained in the present study is 0.03 on $SrRuO_3$ at around 573-773 K.

The thermal conductivity of $SrHfO_3$ is 5.2 $Wm^{-1}K^{-1}$ at room temperature, and it reaches to 2.5-3.0 $Wm^{-1}K^{-1}$ in high temperature. The thermal conductivity of $SrHfO_3$ at high temperature is slightly higher than the thermal conductivity of YSZ, around 2 $Wm^{-1}K^{-1}$. It is necessary to decrease it more to apply it as a new substitute for thermal barrier coating

material, a replacement of YSZ. $SrHfO_3$ is slightly higher than YSZ in both the linear thermal expansion coefficient and melting temperature. This particular base of thermal expansion coefficient and melting temperature has the possibility of practical use. The thermal conductivity of SrY_2O_4 decreases when temperature increases. The thermal conductivity of BaY_2O_4 was 3.9 $Wm^{-1}K^{-1}$ at 298 K, and decreases when temperature increases. The values of thermal conductivity of SrY_2O_4 at 300 and 1200 K are 7.6 and 3.4 $Wm^{-1}K^{-1}$, respectively. The average linear thermal expansion coefficients of SrY_2O_4 and BaY_2O_4 are $10.9x10^{-6}$ K^{-1} and 1.08×10^{-5} K^{-1}, respectively. SrY_2O_4 and BaY_2O_4 have a potential to be utilized as TBC materials because they have high temperature stability and a large enough thermal expansion coefficient. However, innovative TBCs require the overall performance, such as low thermal conductivity (<2 $Wm^{-1}K^{-1}$), high thermal expansion coefficient conductivity (>$9x10^{-6}$ K^{-1}), a stable phase, chemical resistance, a low sintering rate, and high fracture toughness. Therefore more systematic research using wide range tools, such as computer simulation screening and thermal cycle experiment, is needed for the development of new candidates of TBC and TE materials.

References

[1] J. J. Carbajo, G. L. Yoder, S. G. Popov, and V. K. Ivanov, "A review of the thermophysical properties of MOX and UO_2 fuels," *Journal of Nuclear Materials*, **299(3)** 181-198 (2001).

[2] H. Yapici, "Study on transmutation of minor actinides discharged from high burn-up PWR-MOX spent fuel in the force-free helical reactor," *Annals of Nuclear Energy*, **30(4)** 413-436 (2002).

[3] F. T. Ewart, R. G. Taylor, J. M. Horspool, and G. James, "The chemical effects of composition changes in irradiated oxide fuel materials. II. Fission product segregation and chemical equilibriums," *Journal of Nuclear Materials*, **61(3)** 254-70 (1976).

[4] H. Kleykamp, J. O. Paschoal, R. Pejsa, and F. Thummler, "Composition and structure of fission product precipitates in irradiated oxide fuels: correlation with phase studies in the molybdenum-ruthenium-rhodium-palladium and barium oxide-uranium dioxide-zirconium dioxide-molybdenum dioxide systems." *Journal of Nuclear Materials*, **130** 426-433 (1985).

[5] H. Kleykamp, "The chemical state of the fission products in oxide fuels," *Journal of Nuclear Materials*, **131(2-3)** 221-246 (1985).

[6] D.R. O'Boyle, F. L. Brown, and A. E. Dwight, "Analysis of fission product ingots formed in uranium-plutonium oxide irradiated in EBR-II," *Journal of Nuclear Materials*, **35(3)** 257-266 (1970).

[7] I. Sato, H. Furuya, T. Arima, K. Idemitsu, and K. Yamamoto, "Behavior of metallic fission products in uranium-plutonium mixed oxide fuel," *Journal of Nuclear Materials*, **273(3)** 239-247 (1999) 239.

[8] I. Sato, H. Furuya, T. Arima, K. Idemitsu, and K. Yamamoto, "Behavior of fission products zirconium and barium in fast reactor fuel irradiated to high burnup," *Journal of Nuclear Science and Technology*, **36(9)** 775-780 (1999).

[9] S. Yamanaka and K. Kurosaki, "Thermophysical properties of Mo-Ru-Rh-Pd alloys," *Journal of Alloys and Compounds*, **353(1-2)** 269-273 (2003).

[10] A. Weidenkaff, "Preparation and application of nanostructured perovskite phases," *Advanced Engineering Materials*, **6(9)** 709-714 (2004).

[11] R. Vassen, M. Dietrich, H. Lehmann, X. Cao, G. Pracht, F. Tietz, D. Pitzer, and D. Stover, "Development of oxide ceramics for an application as TBC," *Materialwissenschaft und Werkstofftechnik*, **32(8)** 673-677 (2001).

[12] H. Yokokawa and T. Horita, "Cathods," *High Temperature Solid Oxide Fuels Cells*, 119-147 (2003).

[13] M. Parvari, C. Petit, and A. Kinnemann, "Perovskite systems and application in catalysis," *Catalysis Research at the Cutting Edge*, 165-197 (2005).

[14] J. G. Bednorz and K. A. Mueller, "Strontium calcium titanate (Sr1-xCaxTiO3): an XY quantum ferroelectric with transition to randomness," Physical Review Letters, 52(25) 2289-2292 (1984).

[15] H. P. R. Frederikse, W. R. Thurber, and W. R. Hosler, "Electronic transport in strontium titanate," *Physical Review*, **134(2A)** A442-445 (1964).

[16] C. S. Koonce, M. L. Cohen, J. F. Schooley, W. R. Hosler, and E. R. Pfeiffer, "Superconducting transition temperatures of semiconducting strontium titanate," *Physical Review*, **163(2)** 380-90 (1967).

[17] V. E. Henrich, "The surfaces of metal oxides," *Reports on Progress in Physics*, **48(11)** 1481-541 (1985).

[18] H. Muta, K. Kurosaki, and S. Yamanaka, "Thermoelectric properties of rare earth doped $SrTiO_3$," *Journal of Alloys and Compounds*, **350(1-2)** 292-295 (2003).

[19] S. A. Kivelson, "Superconducting materials. Superconductivity on the verge of catastrophe," *Nature Materials*, **5(5)** 343-344 (2006).

[20] Y. M. Tsau, Y. C. Chen, H. F. Cheng, I. N. Lin, "Ferroelectric (Ba,Sr)TiO_3 and Pb(Zr,Ti)O_3 thin films prepared by pulsed laser deposition," *Journal of the European Ceramic Society*, **21(10-11)** 1561-1564 (2001).

[21] S. Zahi, R. Bouaziz, N. Abdessalem, and A. Boutarfaia, "Dielectric and piezoelectric properties of $PbZrO_3$-$PbTiO_3$-$Pb(Ni_{1/3},Sb_{2/3})O_3$ ferroelectric ceramic system," *Ceramics International*, **29(1)** 35-39 (2003).

[22] S. Yan, P. Lu, H. Ma, Q. Jia, and X. Wang, "Thermoelectric power in three lanthanum barium copper oxides," *Solid State Communications*, **64(4)** 537-539 (1987).

[23] F. Iga, Y. Nishihara, J. Sakurai, and M. Ishikawa, "Specific heat and thermoelectric power of Mott transition compound $Y_{0.61}Ca_{0.39}TiO_3$," *Physica B: Condensed Matter*, **237-238** 14-15 (1997).

[24] K. Kobayashi, S. Yamaguchi, M. Mukaida, and T. Tsunoda, "Thermoelectric power of titanate and ferrite with the cubic perovskite structure," *Solid State Ionics*, **144(3,4)** 315-320 (2001).

[25] S. A. Sunsine, L. F. Schneemeyer, J. V. Waszczak, D. W. Murphy, S. Miraglia, A. Santoro, and F. Beech, "Superconductivity in lanthanum barium cuprate perovskites," *Journal of Crystal Growth*, **85(4)**, 632-638 (1987).

[26] C. Bougerol-Chaillout, P. Bordet, S. Kazakov, J. Pshirkov, S. N. Putilin, E. V. Antipov, and M. Nunez-Regueiro, "Structural studies of new superconducting bismuthates $(Sr,K)BiO_3$," *Physica C: Superconductivity*, **341-348** 1813-1816 (2000).

[27] E. V. Antipov, N. R. Khasanova, J. S. Pshirkov, S. N. Putilin, C. Bougerol, O. I. Lebedev, G. Van Tendeloo, A. N. Baranov, and Y. W. Park, "The superconducting bismuth-based mixed oxides," Current Applied Physics, **2** 425-430 (2002).

[28] V. V. Kharton, A. A. Yaremchenko, A. P. Viskup, G. C. Mather, E. N. Naumovich, and F. M. B. Marques, "Ionic and p-type electronic conduction in LaGa(Mg,Nb)O3-δ perovskites," *Solid State Ionics*, **128(1-4)** 79-90 (2000).

[29] V. M. Goldschmidt, T. Barth, G. Lunde, and W. Zachariasen, "Geochemical distribution law of the elements. VII. Summary of the chemistry of crystals," *Skrifter Norske Videnskaps-Akad. Oslo, Mat.-Nat. Kl.* No. 2 117 pp (1926).

[30] A. M. Glazer, "Classification of tilted octahedra in perovskites," *Acta Crystallographica, Section B: Structural Crystallography and Crystal Chemistry*, **28(Pt. 11)** 3384-3392 (1972).

[31] A. M. Glazer, "Simple ways of determining perovskite structures," *Acta Crystallographica, Section A: Crystal Physics, Diffraction, Theoretical and General Crystallography*, **A31(6)** 756-762 (1975).

[32] P. M. Woodward, "Octahedral Tilting in Perovskites. II. Structure Stabilizing Forces," *Acta Crystallographica, Section B: Structure Science*, **B53(1)** 44-66 (1997).

[33] C. J. Howard and H. T. Stokes, "Group-Theoretical Analysis of Octahedral Tilting in Perovskites," *Acta Crystallographica, Section B: Structure Science*, **B54(6)** 782-789 (1998).

[34] M. P. Jorba, G. Tilloca, and R. Collongues, "Structure and properties of strontium zirconate; study of the phase diagram ZrO_2-SrO; extension of the investigation to other systems [of type] MO_2-M'O," Intern. Symp. Magnetohydrodyn. Elec. Power Generation, Papers, Commun., Paris, 3 1185-1197 (1964)

[35] A. V. Shevchenko , L. M. Lopato, G. I. Gerasimyuk, Z. A. Zaitseva, "Reactions in the systems hafnium dioxide - stronium oxides, hafnium dioxide-barium oxide and zirconium dioxide-barium oxide in the regions with a high content of a high content of hafnium dioxide (zirconium dioxide)," *Izvestiya Akademii Nauk SSSR, Neorganicheskie Materialy*, **23(9)** 1495-1499 (1987).

[36] B. J. Kennedy, C. J. Howard, and B. C. Chakoumakos, "High-temperature phase transitions in $SrHfO_3$," *Physical Review B: Condensed Matter and Materials Physics*, **60(5)** 2972-2975 (1999).

[37] D. Kim, B.L. Zink, F. Hellman, S. McCall, G. Cao, and J.E. Crow, "Mean-field behavior with Gaussian fluctuations at the ferromagnetic phase transition of $SrRuO_3$," *Physical Review B: Condensed Matter and Materials Physics*, **67(10)** 100406/1-100406/4 (2003).

[38] D. Kirillov, Y. Suzuki, L. Antognazza, K. Char, I. Bozovic, and T.H. Geballe, "Phonon anomalies at the magnetic phase transition in $SrRuO_3$," *Physical Review B: Condensed Matter*, **51(18)** 12825-12828 (1995).

[39] C. L. Chen, Y. Cao, Z. J. Huang, Q. D. Jiang, Z. Zhang, Y. Y. Sun, W. N. Kang, L. M. Dezaneti, W. K. Chu, and C. W. Chu, "Epitaxial SrRuO3 thin films on (001) $SrTiO_3$," *Applied Physics Letters*, **71(8)** 1047-1049 (1997).

[40] X. Fang and T. Kobayashi, "Characterization of $SrRuO_3$ thin film grown by laser ablation at temperatures above 400° C," *Journal of Applied Physics*, **90(1)** 162-166 (2001).

[41] J. J. Neumeier, A. L. Cornelius, and K. Andres, "Thermodynamic investigation of the magnetic phase transitions of $CaMnO_3$ and $SrRuO_3$," *Physical Review B: Condensed Matter and Materials Physics*, **64(17)** 172406/1-172406/3 (2001).

[42] F. Castelpoggi, L. Morelli, H. R. Salva, S. L. Cuffini, R. Carbonio, and R. D. Sanchez, "Specific heat measurement of the magnetroresistant perovskite $SrRuO_3$," *Solid State Communications*, **101(8)** 597-599 (1997).

[43] R. Agarwal, Z. Siley, and V. Venugopal, "Calorimetric investigations of $SrMoO_3$ and $BaMoO_3$ compounds," *Journal of Alloys and Compounds*, **282(1-2)** 231-235 (1999).

[44] L. H. Brixner, "X-ray study and electrical properties of the system $Ba_xSr_{(1-x)}MoO_3$," *Journal of Inorganic and Nuclear Chemistry*, **14** 225-230 (1960).

[45] Y. S. Lee, J. S. Lee, T. W. Noh, D. Y. Byun, K. S. Yoo, K. Yamaura, and E. Takayama-Muromachi, "Systematic trends in the electronic structure parameters of the 4d transition-metal oxides $SrMO_3$ (M=Zr, Mo, Ru, and Rh)," *Physical Review B: Condensed Matter and Materials Physics*, 67(11) 113101/1-113101/4 (2003).

[46] H. H. Wang, G. Z. Yang, D. F. Cui, H. B. Lu, T. Zhao, F. Chen, Y. L. Zhou, Y. C. Lan, Y. Ding, L. Chen, X. L. Chen, and J. K. Liang, Journal of Vacuum Science & Technology, A: Vacuum, Surfaces, and Films, "Epitaxial growth and electric characteristics of $SrMoO_3$ thin films," **19(3)** 930-933 (2001).

[47] H. Mizoguchi, K. Fukumi, N. Kitamura, T. Takechi, J. Hayakawa, H. Yanagi, H. Hosono, and H. Kawazoe, "Electronic structure of polycrystalline $AMoO_3$ (A = Sr or Ba)," *Journal of Applied Physics*, **85(9)** 6502-6505 (1999).

[48] H. Mizoguchi, N. Kitamura, K. Fukumi, T. Mihara, J. Nishii, M. Nakamura, N. Kikuchi, H. Hosono, and H. Kawazoe, "Optical properties of $SrMoO_3$ thin film," *Journal of Applied Physics*, **87(9, Pt. 1)** 4617-4619 (2000).

[49] B. Jaffe, W. R. Cook and H. Jaffe. In: (3rd. edn. ed.),Piezoelectric Ceramics, Academic Press, New York/London (1971).

[50] M. G. Smith, J. B. Goodenough, A. Manthiram, R. D. Taylor, W. Peng and C. W. Kimbal "Tin and antimony valence states in barium tin antimony oxide ($BaSn_{0.85}Sb_{0.15}O_{3-\delta}$)," *Journal of Solid State Chemistry*, **98** 181-186 (1992).

[51] G. Larramona, C. Gutiérrez, M. R. Nunes and F. M. A. da Costa, "Characterization of the mixed perovskite barium tin antimony oxide ($BaSn_{1-x}Sb_xO_3$) by electrolyte electroreflectance, diffuse reflectance, and x-ray photoelectron spectroscopy," *Journal of the Chemical Society, Faraday Transactions 1: Physical Chemistry in Condensed Phases*, **85(4)** 907-916 (1989).

[52] Y. Shimizu, Y. Fukuyama, T. Narikiyo, H. Arai, and T. Seiyama, "Perovskite-type oxides having semiconductivity as oxygen sensors," *Chemistry Letters*, **(3)** 377-380 (1985).

[53] B. Ostrick, M. Fleischer, U. Lampe and H. Meixner, "Preparation of stoichiometric barium stannate thin films: Hall measurements and gas sensitivities," *Sensors and Actuators, B: Chemical*, **B44(1-3)** 601-606 (1997).

[54] X. Q. Cao, R. Vassen, W. Jungen, S. Schwartz, F. Tietz, and D. Stover, "Thermal stability of lanthanum zirconate plasma-sprayed coating," *Journal of the American Ceramic Society*, **84(9)** 2086-2090 (2001)

[55] B. Saruhan, P. Francois, K. Fritscher, U. Schulz, "EB-PVD processing of pyrochlore-structured $La_2Zr_2O_7$-based TBCs," *Surface and Coatings Technology*, **182(2-3)** 175-183 (2004).

[56] S. G. Tresvyatskii, L. M. Lopato, A. E. Kushchevskii, and A. V. Shevchenko, "Phase diagrams of yttrium sesquioxide-strontium oxide and ytterbium sesquioxide-strontium oxide systems," *Izvestiya Akademii Nauk SSSR, Neorganicheskie Materialy*, **7(10)** 1808-1811 (1971).

[57] Hk. Müller-Buschbaum, "Zur Kenntnis von SrY_2O_4," *Zeitschrift für anorganische und allgemeine Chemie*, 358**(3-4)** 138-146 (1968).

[58] JCPDS 32-1272.

[59] J. G. Pepin, "Crystal data for $SrRE_2O_4$ (RE = rare earth + Y, In)," *Journal of Applied Crystallography*, **14(1)** 70-71 (1981).

[60] S. Arul Antony, K. S. Nagaraja, G. L. N. Reddy, and O. M. Sreedharan, "A polymeric gel cum auto-combustion method for the lower temperature synthesis of SrR_2O_4 (R = Y, La, Sm, Eu, Gd, Er or Yb)," *Materials Letters*, **51(5)** 414-419 (2001).

[61] S. Arul Antony, R. Pankajavalli, K. S. Nagaraja and O. M. Sreedharan, "High temperature stability of SrY_2O_4 by SrF_2-based emf. method," *Materials Letters*, **57(2)** 469-474 (2002).

[62] W. Xu, W. Jia, I. Revira, K. Monge, and H. Liu, "Optical properties of multiple sites of Eu^{3+} in SrY_2O_4 single-crystal fibers," *Journal of the Electrochemical Society*, **148(12)** H176-H178 (2001).

[63] S. J. Park, C. H. Park, B. Y. Yu, H. S. Bae, C. H. Kim, and C. H. Pyun, "Structure and luminescence of SrY_2O_4:Eu," *Journal of the Electrochemical Society*, **146(10)** 3903-3906 (1999).

[64] W. Kwestroo, H. A. M. Van Hal, and C. Langereis, "Compounds in the system barium oxide-yttrium oxide", *Materials Research Bulletin*, **9(12)** 1631-1637 (1974).

[65] G. A. Costa, M. Ferretti, M. L. Fornasini, E. A. Franceschi, and G. L. Olcese, "The crystal structure of barium yttrium oxide (BaY_2O_4), isotypic with strontium yttrium oxide (SrY_2O_4)", *Powder Diffraction*, **4(1)** 24-25 (1989).

[66] V. Massarotti, D. Capsoni, M. Bini, A. Altomare, and A. G. G. Moliterni, "X-ray diffraction study of polycrystalline Y_2BaO_4. A test of the new EXPO program," *Zeitschrift fuer Kristallographie*, **214(4)** 200-204 (1999).

[67] L. M. Lopato, I. M. Maister, and A. V. Shevchenko, "Physiocochemical interaction of dysprosium, yttrium, and ytterbium oxides with barium oxide," *Izvestiya Akademii Nauk SSSR, Neorganicheskie Materialy*, **8(5)** 861-864 (1972).

[68] L. M. Kovba, L. N. Lykova, and E. V. Antipov, "Barium oxide-yttrium oxide system," *Zhurnal Neorganicheskoi Khimii*, **28(3)** 724-727 (1983).

[69] S. Dash, Z. Singh, R. Prasad, and D. D. Sood, "The standard molar Gibbs energy of formation of barium molybdate ($BaMoO_3$(s))," *Journal of Nuclear Materials*, **207** 350-2 (1993).

[70] I. J. McColm, "Ceramic Hardness", Plenum Pub Corp (1990) 6.

[71] Y. Takahashi and M. Asou, "Development of a high-temperature differential scanning calorimeter equipped with a triple-cell system," *Thermochimica Acta*, **223(1-2)** 7-22 (1993).

[72] Japan Thermal Measurement Society, Thermodynamics data base for personal computer MALT2.

[73] JCPDS card, 8-482.($SrMoO_4$)

[74] JCPDS card, 29-193.($BaMoO_4$)

[75] JCPDS card, 24-1224.($SrMoO_3$)

[76] JCPDS card, 34-324.($BaMoO_3$)

[77] F. Kanazawa, Kagaku Sousetsu, 32 (1997) 7.

[78] R. D. Shannon, "Revised effective ionic radii and systematic studies of interatomic distances in halides and chalcogenides," *Acta Crystallographica, Section A: Crystal Physics, Diffraction, Theoretical and General Crystallography*, **A32(5)** 751-67 (1976).

[79] B. C. Chakoumakos, S. E. Nagler, S. T. Misture, and H. M. Christen, "High-temperature structural behavior of $SrRuO_3$," *Physica B: Condensed Matter (Amsterdam)*, **241-243** 358-360 (1998).

[80] B. J. Kennedy and B. A. Hunter, "High-temperature phases of $SrRuO_3$," *Physical Review B: Condensed Matter and Materials Physics*, **58(2)** 653-658 (1998).

[81] J. P. Schreckenbach, N. Meyer, G. Marx, B. T. Lee, and W. M. Kriven, "Strontium hafnate phases by anodic spark conversion," Applied Surface Science, **205(1-4)** 97-101 (2003)

[82] N. D. Zhigadlo, P. Odier, J. Ch. Marty, P. Bordet, and A. Sulpice, "High-temperature phase changes in $RuSr_2GdCu_2O_8$ and physical properties," *Physica C: Superconductivity and Its Applications (Amsterdam, Netherlands)*, **387(3&4)** 347-358 (2003).

[83] N. Sata, H. Matsuta, Y. Akiyama, Y. Chiba, S. Shin, and M. Ishigame, "Fabrication of proton conducting thin films of $SrZrO_3$ and $SrCeO_3$ and their fundamental characterization," *Solid State Ionics*, **97(1-4)** 437-441 (1997).

[84] S. Yamanaka, K. Kurosaki, T. Oyama, H. Muta, M. Uno, T. Matsuda, and S. Kobayashi, "Thermophysical properties of perovskite-type strontium cerate and zirconate," *Journal of the American Ceramic Society*, 88(6) 1496-1499 (2005)

[85] JCPDS 42-39 $SrVO_3$.

[86] S. Yamanaka, M. Fujikane, T. Hamaguchi, H. Muta, T. Oyama, T. Matsuda, S. Kobayashi, and K. Kurosaki, "Thermophysical properties of $BaZrO_3$ and $BaCeO_3$," *Journal of Alloys and Compounds*, **359(1-2)** 109-113 (2003).

[87] S. Yamanaka, K. Kurosaki, T. Matsuda, and S. Kobayashi, "Thermal properties of $SrCeO_3$," *Journal of Alloys and Compounds*, **352(1-2)** 52-56 (2003).

[88] S. Yamanaka, T. Matsuda, K. Kurosaki, and M. Uno, "Thermo-chemical and -physical properties of $BaMO_3$," *Journal of Nuclear Science and Technology*, **Suppl. 3**, 709-712 (2002).

[89] L.G. Van Uitert, H. M. O'Bryan, M. E. Lines, H. J. Guggenheim, and G Zydzik, "Thermal expansion - an empirical correlation," *Materials Research Bulletin*, **12(3)** 261-268 (1977).

[90] K. Yamada, S. Yamanaka, and M. Katsura, "Effects of porosity on elastic modulus of UO_2," *Technology Reports of the Osaka University*, **47(2283-2300)** 181-186 (1997).

[91] M. Fukuhara and I. Yamauchi, "Temperature dependence of the elastic moduli, dilational and shear internal frictions and acoustic wave velocity for alumina, (Y)TZP and '-Sialon ceramics," *Journal of Materials Science*, **28(17)** 4681-4688 (1993).

[92] K. Tanaka, H. Koguchi, and T. Mura, "A dislocation model for hardness indentation problems. II," *International Journal of Engineering Science (Oxford, United Kingdom)*, **27(1)** 11-27 (1989).

[93] S. Yamamoto and T. Tanabe, "New Materials Science: Comprehension Based on Quantum Mechanics. (Atarashii Zairyo Kagaku: Ryoshi Rikigaku ni motozuku Toitsuteki Rikai)," Shouwadou, Kyoto, (1990).

[94] S. Yamanaka, K. Yamada, T. Tsuzuki, T. Iguchi, M. Katsura, Y. Hoshino, and W. Saiki, "Mechanical and thermal properties of uranium intermetallic compounds," *Journal of Alloys and Compounds*, **271-273** 549-556 (1998).

[95] K. Yamada, S. Yamanaka, and M. Katsura, "Physico-chemical properties of $(U,Ce)O_2$," *Journal of Alloys and Compounds*, **275-277** 725-729 (1998).

[96] M. A. Lopes, R. F. Silva, F. J. Monteiro, and J. D. Santos, "Microstructural dependence of Young's and shear moduli of P_2O_5 glass reinforced hydroxyapatite for biomedical applications," *Biomaterials*, **21(7)** 749-54 (2000).

[97] H. J. Frost, Deformation-Mechanism Maps, P`ergamon Press, Oxford, (1982).

[98] F. A. Lindemann, "The Calculation of Molecular Vibration Frequencies," Physik. Z. 11 609-12 (1910).

[99] The Chemical Society of Japan ed., Kikan Kagaku Sousetsu, Perovskite-Related Compounds, No. 32, (1997) p. 37.

[100] K. Yamada, S. Yamanaka, T. Nakagawa, M. Uno, and M. Katsura, "Study of the thermodynamic properties of $(U, Ce)O_2$," *Journal of Nuclear Materials*, **247** 289-292 (1997).

[101] A. Bartolotta, G. Carini, G. D'Angelo, A. Fontana, F. Rossi, G. Tripodo, "Low-energy vibrational dynamics of hydrogenated silica gels," *Journal of Non-Crystalline Solids*, **245** 9-14 (1999).

[102] P. Dougier, J. C. C. Fan and J. B. Goodenough, "Magnetic, electrical, and optical properties of perovskite-type strontium vanadate ($SrVO_{2.90}$ and $SrVO_3$) phases," *Journal of Solid State Chemistry*, **14(3)** 247-59 (1975).

[103] B. K. Moon and H. Ishiwara, "Epitaxial growth of conductive strontium vanadate films on silicon(100) substrates and their electrical resistivities," *Journal of Crystal Growth*, **162(3/4)** 154-160 (1996).

[104] Y. C. Lan, X. L. Che, and M. He, "Structure, magnetic susceptibility and resistivity properties of $SrVO_3$," *Journal of Alloys and Compounds*, **354(1-2)** 95-98 (2003).

[105] V. Giannakopoulou, P. Odier, J.M. Bassat and J.P. Loup, "$SrVO_3$ and Sr_2VO_4, electrical properties below and above room T," *Solid State Communications*, **93(7)** 579-583 (1995)

[106] K. Kurosaki, T. Oyama, H. Muta, M. Uno, and S. Yamanaka, "Thermoelectric properties of perovskite type barium molybdate," *Journal of Alloys and Compounds*, **372(1-2)** 65-69 (2004).

[107] D. M. Rowe, CRC Handbook of Thermoelectrics (CRC Press, New York, 1995).

[108] K. Kurosaki, A. Kosuga, and S. Yamanaka, "Thermoelectric properties of Chevrel phase $Mo_6Te_{8-x}S_x$," *Journal of Alloys and Compounds*, **351(1-2)** 208-211 (2003).

[109] S. Yamanaka, A. Kosuga, and K. Kurosaki, "Thermoelectric properties of Tl_9BiTe_6," *Journal of Alloys and Compounds*, **352(1-2)** 275-278 (2003).

[110] R. S. Caputo and V. C. Truscello, "Two-watt radioisotope power generators for underwater applications," *Intersoc. Energy Convers. Eng. Conf. Proc.*, 9th, 637-45 (1974).

[111] S. G. Tresvyatskii, L. M. Lopato, A. E. Kushchevskii, A. V. Shevchenko, "Phase diagrams of yttrium sesquioxide-strontium oxide and ytterbium sesquioxide-strontium oxide systems," *Izvestiya Akademii Nauk SSSR, Neorganicheskie Materialy*, **7(10)** 1808-1811 (1971).

[112] JCPDS 32-1272. SrY_2O_4

[113] JCPDS 27-44. BaY_2O_4

[114] JCPDS 38-1377. $Ba_3Y_4O_9$

[115] R. Vassen, X. Cao, F. Tietz, D. Basu, D. Stöver, "Zirconates as new materials for thermal barrier coatings," *Journal of the American Ceramic Society*, **83(8)** 2023-2028 (2000).

[116] F. Seitz, "The Modern Theory of Solids," New York ; London : McGraw-Hill, 38 (1940).

[117] *The SGTE Pure Substance and Solution databases*, GTT-DATA SERVICES, (1996).

[118] B. Schulz, "Thermal conductivity of porous and highly porous materials." *High Temperatures - High Pressures*, **13(6)** 649-60 (1981) 649-60.

[119] E. A. Dean and J. A. Lopez, "Empirical dependence of elastic moduli on porosity for ceramic materials," *Journal of the American Ceramic Society*, **66(5)** 366-70 (1983).

[120] D. R. Clarke, "Materials selection guidelines for low thermal conductivity thermal barrier coatings," *Surface and Coatings Technology*, **163-164** 67-74 (2003).

[121] G. A. Slack, "The thermal conductivity of nonmetallic crystals," *Solid Atate Physics*, **34** 1-71 (1979)

[122] T. M. Tritt ; Editor. "Thermal Conductivity : Theory, Properties, and Applications." 290 pp. (Kluwer Academic/Plenum Publishers, New York, N. Y.) USA. (2004)

[123] D. G. Cahill, S. K. Watson, and R. O. Pohl, "Lower limit to the thermal conductivity of disordered crystals," *Physical Review B: Condensed Matter and Materials Physics*, **46(10)** 6131-40 (1992)

Chapter 3

Fabrication and physical properties of oxide films

In this chapter, the author described the thermal conductivity of TiO_2 and ZrO_2 films with different microstructures prepared by metal-organic chemical vapor deposition (MOCVD). This atomistic deposition method can provide highly pure materials with microstructure at atomic or nanometer-scale levels. The author then discusses the microstructure and thermal conductivity.

3.1. Introduction

The thermal conductivity of oxide films is very important in various engineering areas, such as TBCs [1,2] and TEs [3,4]. In TBC applications, a low thermal conductivity will provide greater insulation and permit both higher turbine operating temperatures and higher thermal efficiency. In TE applications, an effective material must have a low thermal conductivity in order to maintain a temperature gradient in the material. Therefore, the reduction of thermal conductivity has been attempted in both TBC and TE research to increase system reliability and performance [3,4]. Generally, a material's thermal conductivity is determined by not only the atomic scale structure, such as the chemical composition and the crystal structure, but also the microstructure. In other words, it is possible to control the thermal conductivity by tuning the material's microstructures, such as nanopores, nanoclacks, microclacks and morphology. Accurate knowledge of the thermal conductivity of films with different microstructures is important.

Titanium dioxide (TiO_2) films [5,6] are widely used in various engineering areas such as optical [7] and electrical device applications [8] and photocatalysts [9], yet their thermal conductivity has been scarcely reported. TiO_2 is not a suitable material for TBC and TE applications. However the microstructure design of TiO_2 contributes actively to the application. Zirconium dioxide (ZrO_2) films are widely used in various engineering applications, such as TBCs [10], dielectric layers [11], sensors

[12] and fuel cells [13], because of their heat resistance, environmental resistance, high strength and ion conducting. The relationships between physical properties and microstructures of undoped zirconium films have rarely been established, until now. In these days, only the relationship on mechanical property was reported [14]. ZrO_2 composed of Zr^{4+} and O^{2-} ions is ionic crystal. The crystal structure at high temperature is a fluorite structure. The Zr^{4+} ion is much smaller in comparison to the O^{2-} ion, that as the thermal vibration of a crystal lattice goes down, the cubic structure transforms to a tetragonal, then to a monoclinic structure. For TBC and TE applications, the reduction of thermal conductivity has been attempted in order to increase the reliability and performance of the materials.

3.2. Experimental procedures

3.2.1. Sample preparation

A vertical cold-wall-type low-pressure MOCVD apparatus was used to prepare the films. Figure 3.1 shows the schematic view of the apparatus. $Ti(O\text{-}i\text{-}C_3H_7)_4$ (titanium tetra-iso-propoxide [TTIP]; 99.999%, Kojundo Chemical Laboratory) and $Zr(O\text{-}t\text{-}C_4H_9)_4$ (Zirconium tetra-tertiary-butoxide [ZTB]; 99.99%, Kojundo Chemical Laboratory) were used as precursors, vaporized at 338 K and 336 K (1 Torr of the vapor pressure), and carried with high-purity argon (99.9999%) gas at a flow rate of 50 ml/min. The precursor vapor was mixed with high-purity oxygen (99.9999%) gas at a flow rate of 100 ml/min and pre-heated at 353, 433 K before being introduced into the reactor. The total gas pressure in the reactor was controlled by the pumping speed wile using a rotary pump (ULVAC, G-100D). The films were deposited on fused silica (20x20x1 mm) for characterizations, and on borosilicate glasses (2.5x12.5x0.03 mm, D-263, Schott Desag) for thermal conductivity measurements under total pressures of 150 and 660 Pa for TiO_2 and ZrO_2, and on a (100) face of NaCl single crystal (20x20x2 mm, Furuuchi

Chemical) substrate under a total pressure of 150 Pa for TiO_2. TiO_2 thin films were deposited on titanium plates (99.5%, 20x20x1 mm, Nilaco) and platinum plates (99.98%, 20x20x1 mm, Nilaco). The plates were buffed with alumina compounds whose sizes were 0.05 microns after polishing with #1200 SiC paper. The substrates were washed in acetone with ultrasonic cleaning. The substrate-free TiO_2 film was prepared by removing the NaCl substrate in deionized water (See Fig.3.2.). For TiO_2 deposition, the deposition temperature and time were chosen to be 673, 773, 873 K and 1, 2, 3 hours, respectively. For ZrO_2 deposition, the substrates were heated from 573 to 873 K and the deposition time was chosen to be 1 hour.

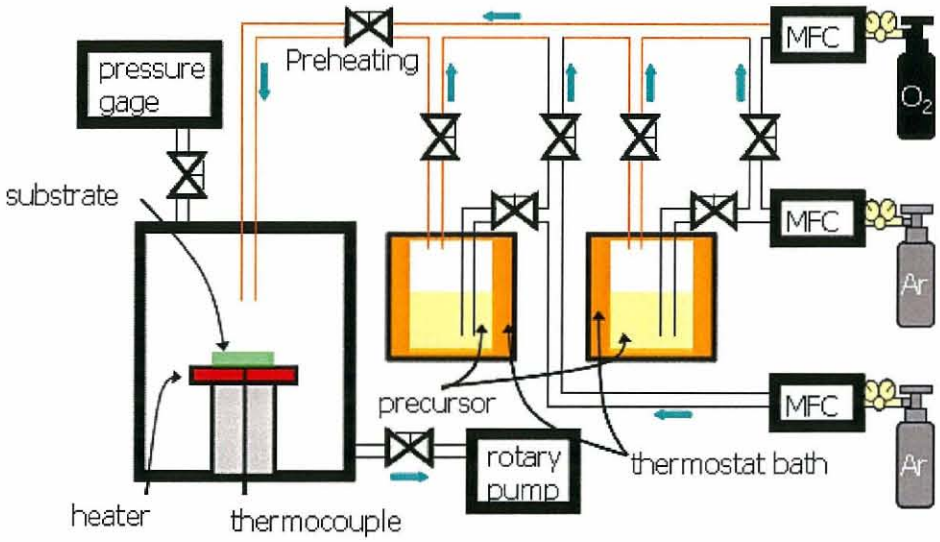

Fig. 3.1 Schematic view of MOCVD aparatus

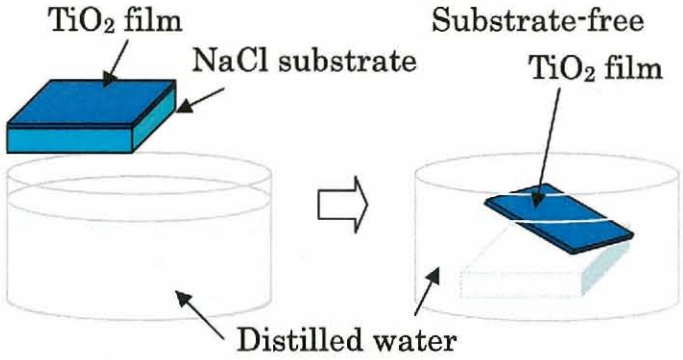

Fig. 3.2 Schematic view of the preparation method of substrate-free TiO_2 film

3.2.2. Sample characteristics

The XRD using Cu Kα radiation was performed to reveal the growth orientation of the films on borosilicate glasses and fused silica substrates. The morphology of the films on borosilicate glasses and fused silica substrates were observed by a field-emission scanning electron microscope (FE-SEM). The thicknesses of the films and grain size on the top surface were evaluated from the FE-SEM images. To determine the composition of the films on fused silica substrates, 2.6 MeV p+ and 1.0 MeV d+, whose beams were generated by a 5SDH-2 tandem Pelletron accelerator in Kobe University, were used for Rutherford backscattering spectroscopy (RBS) and nuclear reaction analysis (NRA), respectively (See Fig.3.3.). RBS and NRA can detect minute impurities with high accuracy, since the analysis uses the interaction of the ion beam and the solid. RBS and NRA are useful methods of analysis for quantification of heavy elements and light elements, respectively. The principle of RBS is based on the fact that the Rutherford scattered ion energy into the direction of an atom that is different in atomic weight. The energy E_1 of the scattered particle detected with the detection angle of θ is expressed by the energy and momentum conservation laws as,

$$E_1 = \left\{ \frac{M_1 \cos\theta + (M_2^{\,2} - M_1^{\,2} \sin^2\theta)^{1/2}}{M_1 + M_2} \right\}^2 E_0, \qquad (3.1)$$

where M_1, M_2 and E_0 are a mass of an incident ion, a mass of an atom at rest and an incident energy. The scattered particle then loses the kinetic energy by the time it reaches to the surface. The energy loss ΔE_1 is as follows,

$$\Delta E_1 = \int_0^{x/\sin(\theta-\theta_0)} \left(-\frac{dE}{dx} \right) dx. \qquad (3.2)$$

The differential scattering cross section is expressed by

$$\frac{d\sigma_s(E)}{d\Omega} = \left(\frac{Z_1 Z_2 e^2}{4E_1} \right)^2 \frac{4}{\sin^4\theta} \frac{\left[\left\{ 1 - \left((M_1/M_2)\sin\theta \right)^2 \right\}^{1/2} + \cos\theta \right]^2}{\left\{ 1 - \left((M_1/M_2)\sin\theta \right)^2 \right\}^{1/2}}. \qquad (3.3)$$

where $d\sigma_s(E)/d\Omega$ is the angular differential scattering cross section, E is the energy generated when the ion impacts with a particle, and e is the charge of electron, e^2=14.4 eVÅ. On the other hand, products of a nuclear reaction taking place at the depth x are traced in NRA. The yield dY of the lighter reaction products originating in the region between depths x and $x + dx$ is expressed by,

$$dY = Q\frac{d\sigma_f(E)}{d\Omega}N dx \Delta\Omega, \qquad (3.4)$$

where Q is the reaction Q-value (the difference in static energy between the states of the beginning and the end of the reaction), $\sigma_f(E)$ is the total nuclear fusion cross section in CMS, Ω is the solid angle and N is the number of target atoms per unit volume. No filter was located on the solid-state detector (SSD) for RBS positioned at an angle of 160 degrees with 2.1 m steradians of a solid angle. The SSD for NRA positioned at an angle of 140 degrees with 2.1 m steradians was set up with an Al filter (12.5 μm thickness). The details of the RBS and NRA measurements can be found in the references [15-17].

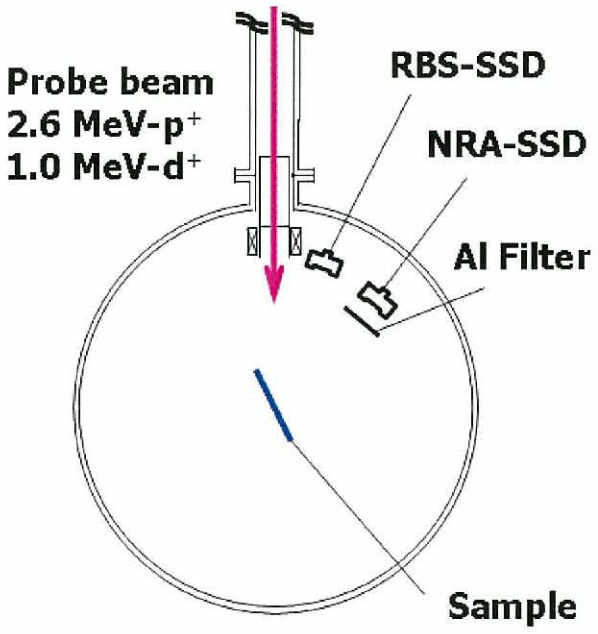

Fig. 3.3 Schematic view of experimental apparatus used for RBS and NRA

3.2.3. Thermal properties

The thermal conductivity of the in-plane direction of the substrate-free TiO_2 film, and of TiO_2 and ZrO_2 films on borosilicate glasses was measured by an alternating current (AC) calorimetric method [18] (Laser PIT, ULVAC) in the temperature range of 300 to 470 K. Samples are heated by a modulated laser beam. In a one-dimensional system, the equation of heat conduction is given by,

$$\frac{\partial T}{\partial t} = D\frac{\partial^2 T}{\partial x^2}, \tag{3.5}$$

where T is the temperature, t is time, D is the thermal diffusivity of the sample, and x is the distance from the irradiated position. The temperature wave at $x = 0$ is given as

$$T = T_0 \exp(i\omega t), \tag{3.6}$$

where T_0 is a constant and ω is the angular frequency. The heat conduction equation is solved and the temperature wave at x is given by

$$T = T_0 \exp(-kx)\exp[i(\omega t - kx)], \tag{3.7}$$

where $1/k$ is the thermal diffusion length. As the irradiated portion of the sample x changes, the ac temperature response is measured by a thermocouple attached to the opposite face of the sample [19]. By analyzing the amplitude decay and the phase shift of the ac temperature as a function of the spatial distance between the irradiated portion and the thermocouple, the logarithmic decrement of the amplitude k_a and phase shift increment k_p can be obtained. If there is no heat loss from the surfaces, k_a and k_p do not coincide with each other. When the thermal diffusivity of a sample is low, heat loss effects should be taken into account, and true k can be obtained from the following equation [20].

$$k = \sqrt{k_a k_p}\,. \tag{3.8}$$

The thermal diffusivity of the sample can be derived from the following equation,

$$k = \sqrt{\frac{\omega}{2D}} = \sqrt{\frac{\pi f}{D}} \tag{3.9}$$

where f is the frequency of the laser. From this result, true thermal diffusivity can be obtained from the amplitude and the phase of ac temperature. When a film is deposited on a half-surface of the rectangular substrate, the apparent thermal diffusivities of the deposited region (film + substrate) D_{012} and the non-deposited region (substrate) D_{01} are expressed by the following equations.

$$D_{012} = \frac{D_0 C_0 d_0 + D_1 C_1 d_1 + D_2 C_2 d_2}{C_0 d_0 + C_1 d_1 + C_2 d_2} \tag{3.10}$$

$$D_{01} = \frac{D_0 C_0 d_0 + D_1 C_1 d_1}{C_0 d_0 + C_1 d_1} \tag{3.11}$$

where suffixes 0, 1, and 2 denote the blackening layer, substrate layer, and film layer, respectively. Eq. (3.12) is obtained by Eq. (3.10) and Eq. (3.11). The thermal conductivity of the film, λ_2, is then given by Eq. (3.13).

$$(D_{012} - D_{01})(C_0 d_0 + C_1 d_1) + D_{012} C_2 d_2 = D_2 C_2 d_2 \tag{3.12}$$

$$\lambda_2 = D_2 C_2 = D_{01} C_1 \left\{ \frac{C_2}{C_1} + \left(\frac{C_2}{C_1} + \frac{C_0 d_0}{C_1 d_2} + \frac{d_1}{d_2} \right) \left(\frac{D_{012}}{D_{01}} - 1 \right) \right\} \tag{3.13}$$

where C are the specific heat capacities per unit volume of solids. Assuming that the thickness of the blackening layer is too small to compare with the thickness of the film layer, Eq. (3.13) can be reduced to Eq. (3.14).

$$\lambda_2 = D_{01} C_1 \left\{ \frac{C_2}{C_1} + \left(\frac{C_2}{C_1} + \frac{d_1}{d_2} \right) \left(\frac{D_{012}}{D_{01}} - 1 \right) \right\} \tag{3.14}$$

The thermal conductivity of the film, λ_2 was determined by using Eq. (3.14). The thermal diffusivities of the deposited region (thin film+substrate), D_{012}, and the non-deposited region (substrate), D_{01}, were determined by the measurement. The thickness of the substrate and the thin film, d_1 and d_2, were determined by SEM images. When the specific heat capacity per unit volumes of the substrate, C_1 and of the sample, C_2, are known, the ratio of the specific heat capacity per unit volume, C_2/C_1, are can be calculated. The

specific heat capacity per unit mass of a solid is the same regardless of its crystalline or other state, but the densities can differ depending on the amorphous or crystalline state and other factors. Assuming that there is no difference in chemical composition between the bulk material and the film, and that there are no significant vacancies in the film, the specific heat capacity per unit mass of the film will be the same as that of the bulk material. The experiment was performed in the frequency range of 0.1 to 0.5 Hz. The measurement was performed under a vacuum (<0.01 Pa), produced using a turbo-molecular pump, to eliminate the effect of air layers.

The substrate and frame materials are borosilicate glass of D263 having thicknesses of 30 and 200 μm respectively, supplied by DESAG (Schott Group). The substrate was processed to a width of 2.5 mm with no uniformity less than ±0.3 %, and has a length of 12.5 mm. It has a specific heat capacity per unit volume of 1.80×10^{6} $J\cdot m^{-3}\cdot K^{-1}$ and a thermal diffusivity of 5.6×10^{-7} $m^{2}\cdot s^{-1}$ [21]. The whole surface of the deposited sample was coated with less than 100 nm-thick bismuth by physical vapor deposition (PVD), such as the plasma sputtering method and the resistance heating method. A thermocouple was attached to the central opposite sample.

3.3. Results and Discussion

3.3.1. Morphology

The state of TiO_2 films and the interface adherence between the films and fused silica substrates, deposited in neither the deposition temperature of 673, 773 K nor the pre-heated at 353 K, were not exact to measure thermal conductivity. Therefore the deposition temperature and the pre-heated temperature for the deposition on fused silica, and borosilicate glasses for the measurement of thermal conductivity were determined to be 873 K and 433 K, respectively. Figure 3.3 shows the FE-SEM images of the TiO_2 films

deposited on fused silica substrate under a total pressure of 150 Pa in the deposition temperature of 873 K and the pre-heat temperature of 433 K for a deposition time of an hour. The faceted texture of the surface (Fig. 3.3(a)) and the dense texture of the cross section (Fig. 3.3(b)) were obtained in the film deposited at 150 Pa. The rough area in the middle of the SEM images indicates the TiO_2 film. The smooth area in the lower side of the SEM images indicates the fused silica substrate. Figure 3.4 shows the FE-SEM images of the TiO_2 films deposited on fused silica substrate under a total pressure of 660 Pa in the deposition temperature of 873 K and the pre-heat temperature of 433 K for a deposition time of an hour. The top surface of the film deposited at 660 Pa reveals a similar faceted texture with the film deposited at 150 Pa (See Fig. 3.4(a).). On the other hand, a cross sectional morphology of the film deposited at 660 Pa (See Fig. 3.4(b).) shows a different tendency. The majority of the texture reveals the columnar texture with feather-like striations (Fig. 3.4.(c-d)). The dendritic texture (Fig. 3.4(e-f)) was obtained particularly in the upper part of the feather-like texture. Figure 3.4.(d) and Fig. 3.4.(f) are expanded SEM images of the squared areas in Fig. 3.4.(c) and Fig. 3.4.(c-d), respectively. Jung et al. reported that small particle crystals were observed in the bottom of the deposited film and small columnar crystal was grown and increasing in size with the crystal growth, because the surface area did not increase with the crystal growth [22]. The first phase of the crystal growth, crystal nucleation, occurred. The nuclei grew and coalesced to grow a small size columnar structure which was finally grown to a large-size columnar structure. The thickness of films deposited at 150 Pa (dense texture) and 660 Pa (feather-like texture) have 18.2 μm and 24.2 μm, respectively. Generally, a fast deposition is caused by a high deposition temperature and high supersaturation. In addition, the high supersaturation interferes with the diffusion on the surface. Therefore, higher pressure produces a more complex texture in the present study. The feather-like texture at high pressure was always obtained with a higher

growth rate than the dense texture at low pressure using the same deposition time. The higher pressure (surpersaturation) brought a multinucleation growth. Therefore the columnar texture of the film deposited on borosilicate substrates at 660 Pa was obtained by the growth of a small nucleus. On the other hand, the lower pressure (surpersaturation) gave a single nucleation growth. Therefore the dense texture of the film deposited at 150 Pa was obtained by the collision and merging of enlarged islands with adjoining ones. In the present case, changing the reaction parameter (total pressure) brought the change in the morphology. Only the career gas was changed to N_2 in the total deposition pressure of 150 Pa. The FE-SEM images of the film deposited with using N_2 career gas is shown in Fig. 3.5. The morphology was similar with the morphology deposited using Ar gas. However, the thickness of the film was a smaller value, 5.2 μm. Therefore the difference in career gas influences the deposition rate. The result shows that N_2 gas blocks the crystal growth, because the absorptive capacity of N_2 is higher than that of Ar.

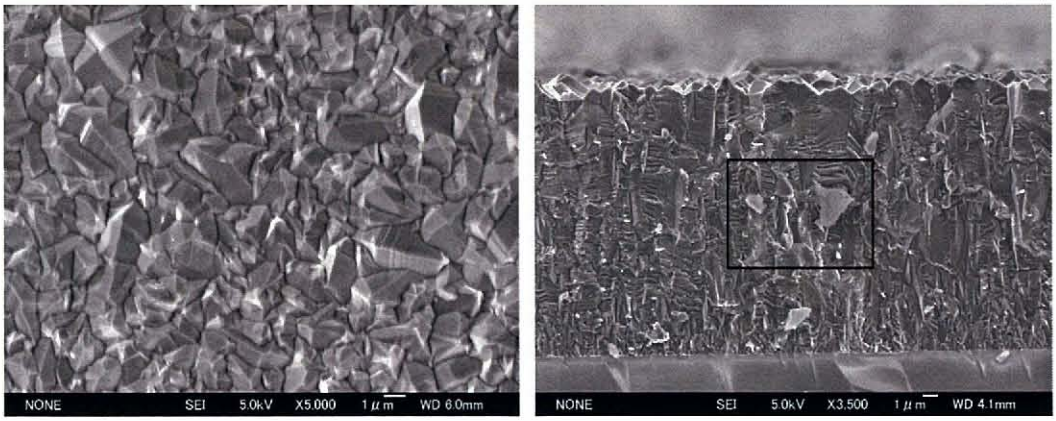

(a) (b)

Fig. 3.3 Surface (a) and cross-sectional (b) SEM images of the film deposited at 150 Pa on fused silica. The rough area in the middle of the pictures is deposited TiO_2 film. The smooth area in the lower side of the pictures is the fused silica substrate.

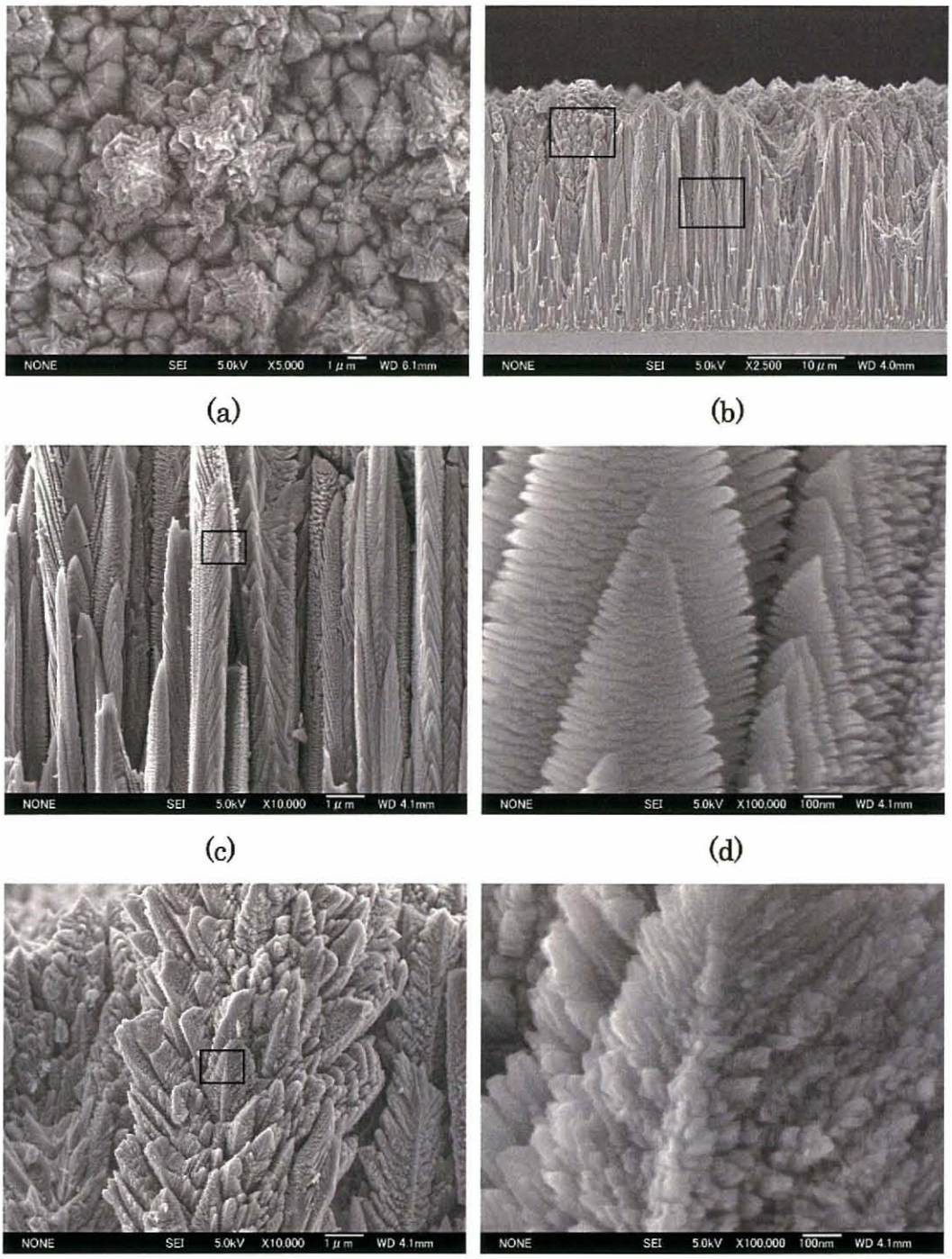

Fig. 3.4 Surface (a) and cross-sectional (b-f) SEM images of the film deposited at 660 Pa on fused silica. (d) and (f) are enlarged pictures of the squared areas in (c) and (c-d), respectively.

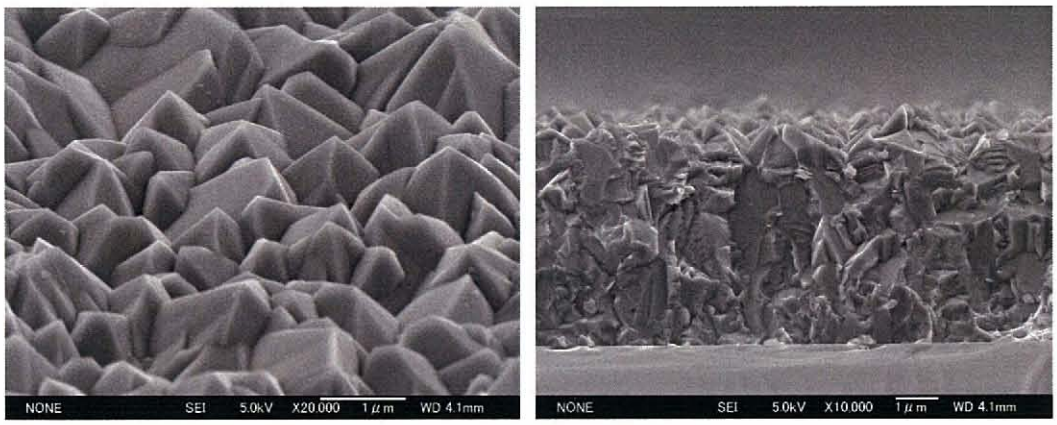

(a) (b)

Fig. 3.5 Surface (a) and cross-sectional (b) SEM images of the film deposited using N_2 carrier gas at 150 Pa on fused silica.

Figure 3.6 shows the FE-SEM images of the TiO_2 films deposited at 150 Pa in a deposition time from 1 hour to 3 hours, and 660 Pa for a deposition time from 1 hour to 2 hours on borosilicate glasses. The TiO_2 films deposited 150 Pa with borosilicate glasses indicated similar morphology with the texture of TiO_2 films on fused silica substrate. The surface of each film shows similar faceted texture. The every cross section of the films deposited at 150 Pa shows dense texture. The majority of the cross sectional morphology of the film deposited at 660 Pa reveals the columnar texture with feather-like striations partly obtaining the dendritic texture. The thickness and grain size of films with borosilicate glasses increased with increasing deposition time. The values are summarized in Table. 3.1. An average deposition rate was evaluated from each thickness. The films deposited at 150 Pa (dense texture) have an average deposition rate of 3.2 $\mu m\ h^{-1}$. On the other hand, the films deposited at 660 Pa (feather-like texture) have an average deposition rate of 5.7 $\mu m\ h^{-1}$.

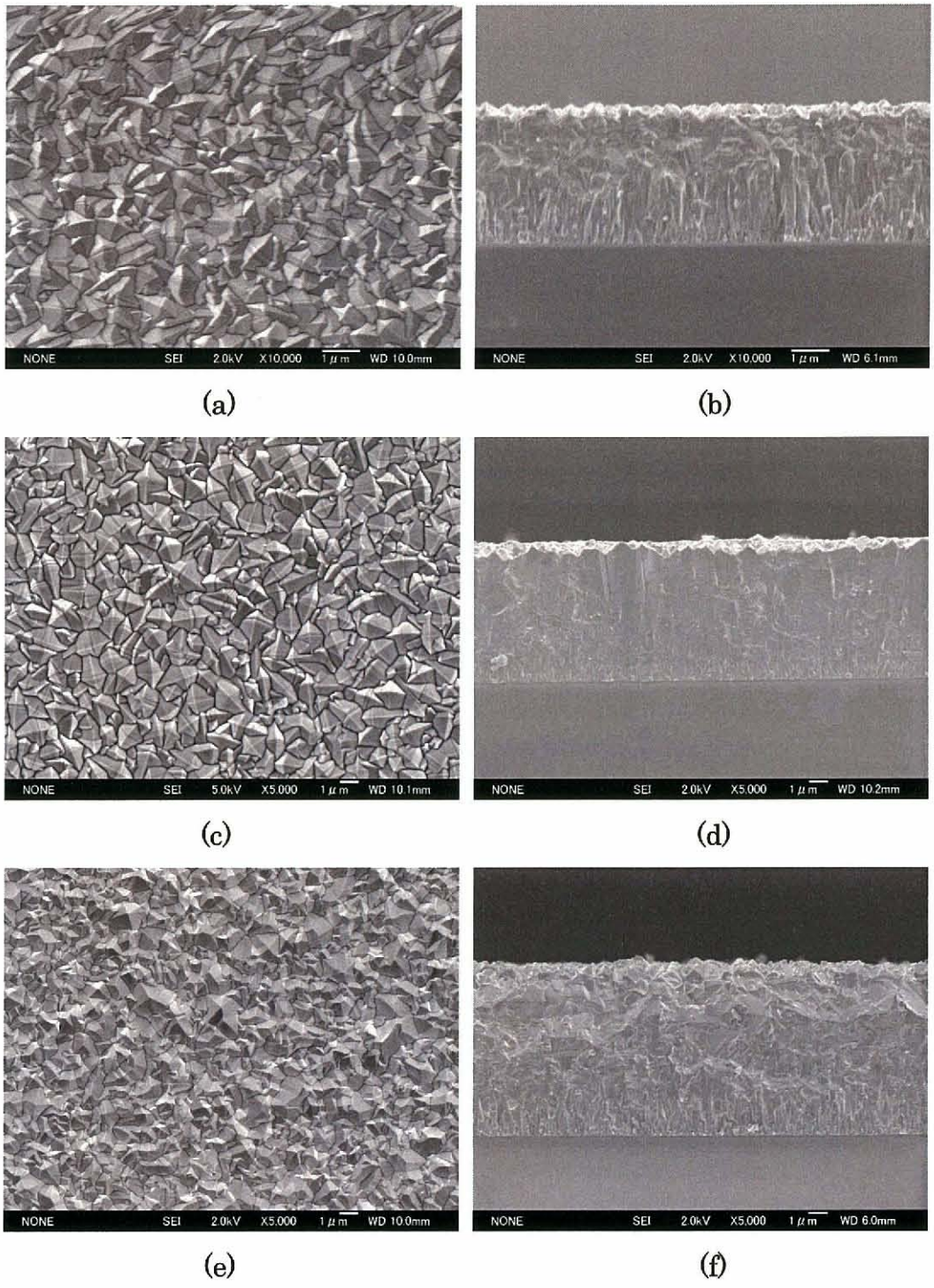

Fig. 3.6 Surface (a,c,e,g,i) and cross-sectional (b,d,f,h,j) SEM images of the film deposited on borosilicate glass. (a,b) TiO_2 film deposited in 150 Pa for 1 hr, (c,d) TiO_2 film deposited in 150 Pa for 2 hrs, (e,f) TiO_2 film deposited in 150 Pa for 3 hrs, (g,h) TiO_2 film deposited in 660 Pa for 1 hr, (i,j) TiO_2 film deposited in 660 Pa for 2 hrs.

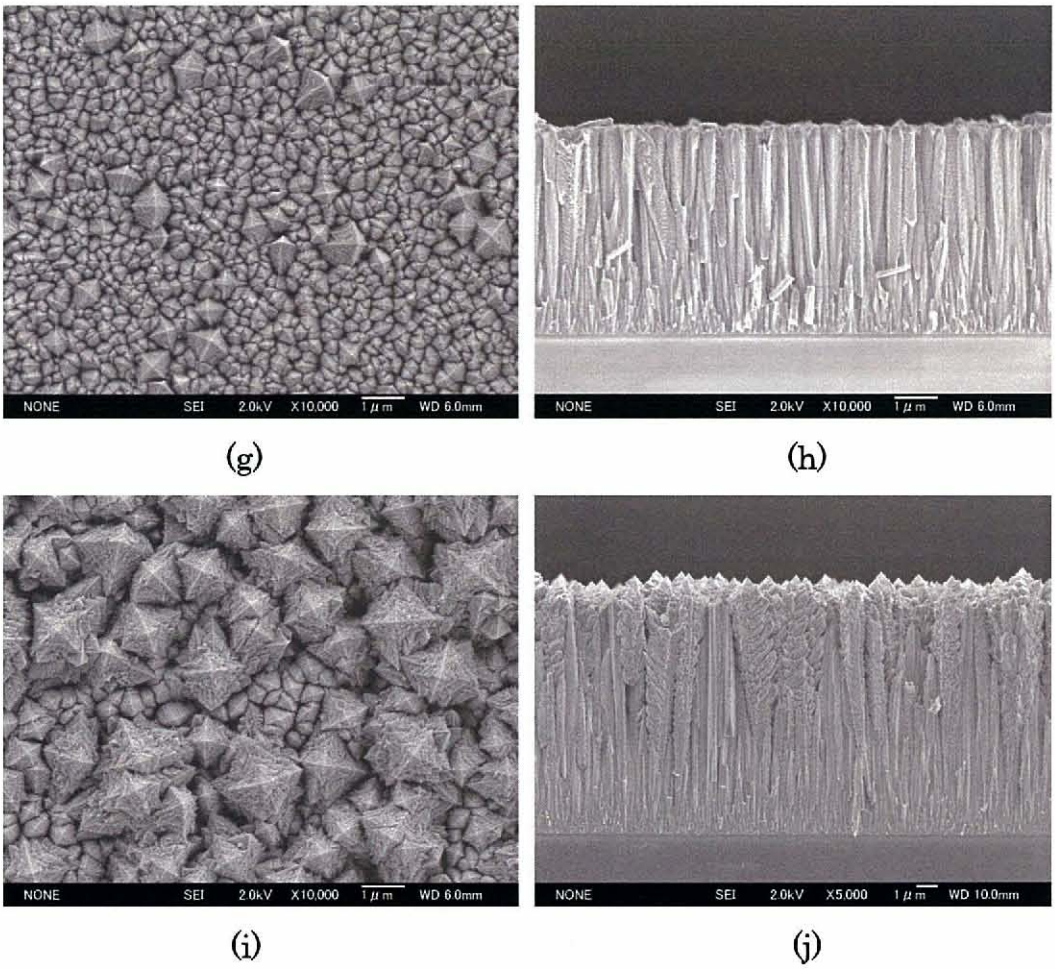

Fig. 3.6 Surface (a,c,e,g,i) and cross-sectional (b,d,f,h,j) SEM images of the film deposited on borosilicate glass. (a,b) TiO_2 film deposited in 150 Pa for 1 hr, (c,d) TiO_2 film deposited in 150 Pa for 2 hrs, (e,f) TiO_2 film deposited in 150 Pa for 3 hrs, (g,h) TiO_2 film deposited in 660 Pa for 1 hr, (i,j) TiO_2 film deposited in 660 Pa for 2 hrs.

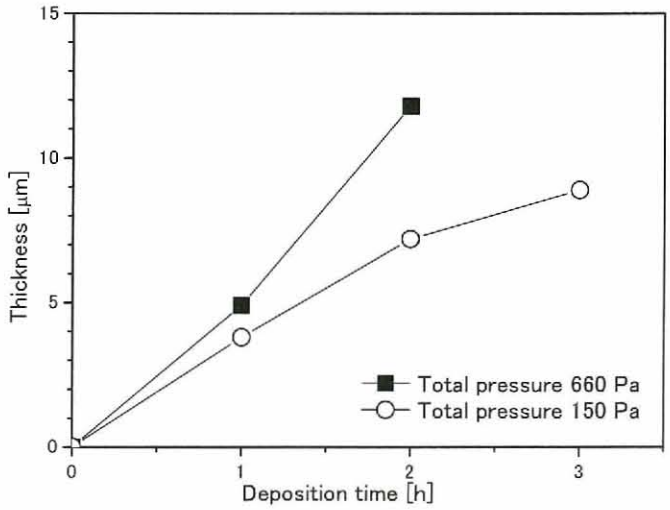

Fig. 3.7 TiO_2 film thickness versus deposition time for the exposures of 150 Pa and 660 Pa at the deposition temperature of 873 K.

Table 3.1 Preparation conditions, textural characteristics, and thermal conductivity values at room temperature of TiO_2 films deposited on borosilicate substrates.

Total pressure [Pa]	Deposition time [hour]	Morphology	Film thickness [μm]	Grain size [μm]	Thermal conductivity at R.T. [$Wm^{-1}K^{-1}$]
150	1	Dense texture	3.8	360	5.1
150	2		7.2	490	6.3
150	3		8.9	750	6.7
660	1	feather-like texture	4.9	210	0.24
660	2		11.8	730	0.57

Figure 3.8(a,b) shows the cross-sectional SEM images of the TiO_2 film deposited on NaCl substrate and the substrate-free TiO_2 film deposited at 150 Pa. The rough area in the middle of the SEM images is deposited TiO_2 film. The smooth area in the lower side of the SEM images is the NaCl single crystal substrate. The morphology is a similar texture with the film deposited at 150 Pa on fused silica and borosilicate substrates. However, the microstructure shows a softer grain boundary than the film deposited on borosilicate substrates, and a smooth surface without a faceted texture. The thickness of the substrate-free film was 20.0 μm. The deposition rate using NaCl substrate is higher than those using borosilicate substrates because the nucleation mechanism is different. It is probable that the growth of the films deposited on borosilicate substrates and NaCl substrates are the Volmer-Weber regime and the Frank-van der Merve regime due to the difference in substrates, respectively. The formation of a faceted texture on borosilicate substrates brought a lower deposition rate than that on NaCl substrates. It seems that the ionic structure and the surface condition of the substrates gave the smooth surface and the higher deposition rate.

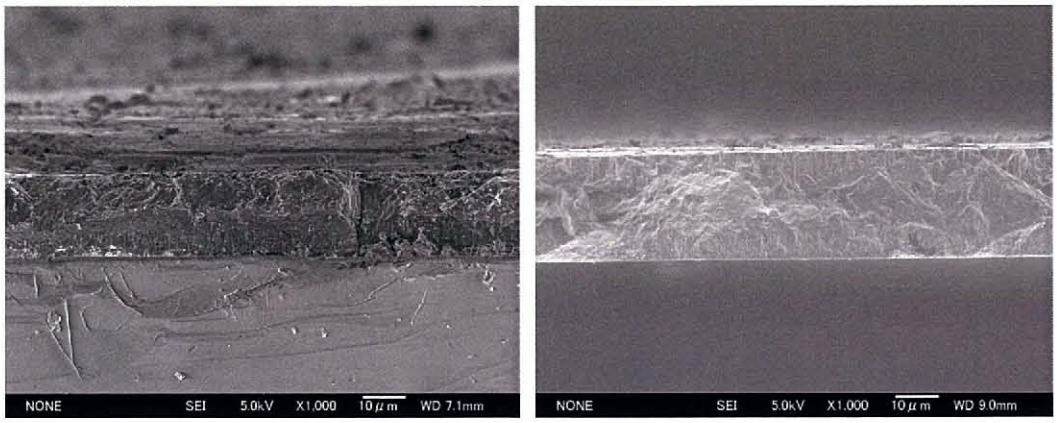

(a) (b)

Fig. 3.8 Cross-sectional SEM images of fractured (a) TiO_2 film on NaCl single crystal and (b) substrate-free TiO_2 film. (a) The rough area in the middle of the pictures is deposited TiO_2 film. The smooth area in the lower side of the images is the NaCl single crystal substrate.

Figure 3.9a shows the FE-SEM images of the TiO_2 films deposited on Pt substrate under a total pressure of 150 Pa in the deposition temperature of 673 K and 873 K and the pre-heat temperature of 433 K in a deposition time of an hour. The deposition temperature, the deposition time and film thickness of subscripts of (a,b), (c,d) and (e,f) are 673 K, 673 K and 873 K, 3 min, 9 min and 3 min, and 190 nm, 600 nm and 520 nm. The thickness was increasing when both increasing deposition time and deposition temperature. The morphology of the surface was faceted texture in all deposition conditions. The dense texture of cross sectional morphology was obtained at 673 K. The columnar texture of cross sectional morphology was obtained at 873 K.

Figure 3.9b shows the FE-SEM images of the TiO_2 films deposited on Ti substrate under a total pressure of 150 Pa in the deposition temperature of 673 K and the pre-heat temperature of 433 K in a deposition time of an hour. In some sample preparations, the carrier gas was bypassed from the bubbler. The volume of total Ar gas, bubbled carrier gas and bypassed dilution gas was kept at 50 sccm. The rate of bubbled Ar of subscripts of (g,h), (i,j) and (k,l) are 50 sccm, 50 sccm and 15 sccm. The deposition time and film thickness of subscripts of (g,h), (i,j) and (k,l) are 9 min, 15 min and 30 min, and 170 nm, 350 nm and 420 nm. The thickness was increasing with increasing deposition time. The morphology of surface was changed from a circular texture to a faceted texture with increasing deposition time. The dome-shaped dense texture of cross sectional morphology was obtained in all deposition conditions.

Figure 3.9c shows the FE-SEM images of the TiO_2 films deposited on Ti substrate under a total pressure of 150 Pa in the deposition temperature of 773 K and the pre-heat temperature of 433 K in a deposition time of an hour. The rate of bubbled Ar of subscripts of (m,n), (o,p), (q,r), (s,t) and (u,v) are 50 sccm, 50 sccm, 25 sccm, 25 sccm and 15 sccm. The deposition time and film thickness of subscripts of (m,n), (o,p), (q,r), (s,t) and (u,v) are 5 min,

6 min, 8 min, 15 min and 15 min, and 150 nm, 390 nm, 210 nm, 560 nm and 620 nm. The thickness was increasing with increasing deposition time. The columnar texture of cross sectional morphology was obtained in the whole deposition conditions.

Figure 3.9d shows the FE-SEM images of the TiO_2 films deposited on Ti substrate under a total pressure of 150 Pa in the deposition temperature of 873 K and the pre-heat temperature of 433 K in a deposition time of an hour. The deposition time and film thickness of subscripts of (w,x) and (y,z) are 1 min and 3 min, and 200 nm and 680 nm. The thickness was increasing with increasing deposition time. The morphology of the surface was a faceted texture. The columnar texture of cross sectional morphology was obtained in all deposition conditions.

Figure 3.10 shows the relationship between the thickness and deposition time. The film thickness was linearly increasing with the deposition time. The deposition rate calculated from the experimental results is shown in Fig. 3.11. The deposition rate deposited on Pt is extremely higher than the deposition rate deposited on Ti. From the relationship between the deposition rate and substrate temperature, the activation energy can be determined. The activation energy deposited on Pt and Ti with the bubbling gas rate of 50 sccm and 15 sccm was determined to be 27.1 kJ mol^{-1}, 57.2 kJ mol^{-1} and 57.3 kJ mol^{-1}. The activation energy means the energy required to excite it from the ground state of the starting material to the transition state of the reaction. The activation energy of the deposition on Pt is approximately 30 kJ mol^{-1} lower than that of the deposition on Ti by the catalysis of Pt. Therefore it seems that the average deposition rate on Pt is higher than the average deposition rate on Ti.

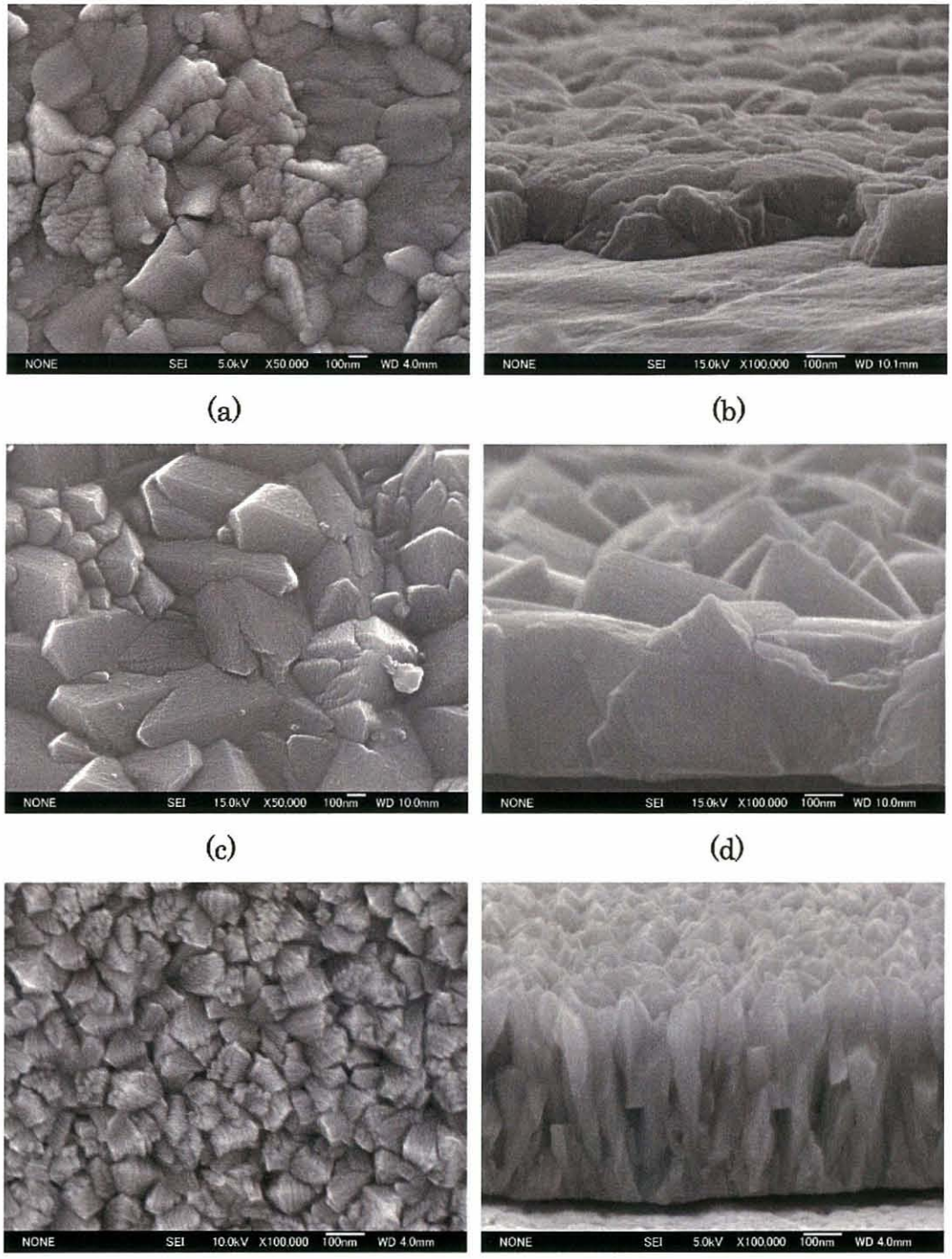

Fig. 3.9a Surface (a,c,e) and cross-sectional (b,d,f) SEM images of the TiO_2 film deposited on Pt in 150 Pa at the deposition temperature of 673 K (a-d) and 873 K (e,f). (a,b) deposited at 673 K for 3 min, (c,d) deposited at 673 K for 9 min, (e,f) deposited at 873 K for 3 min

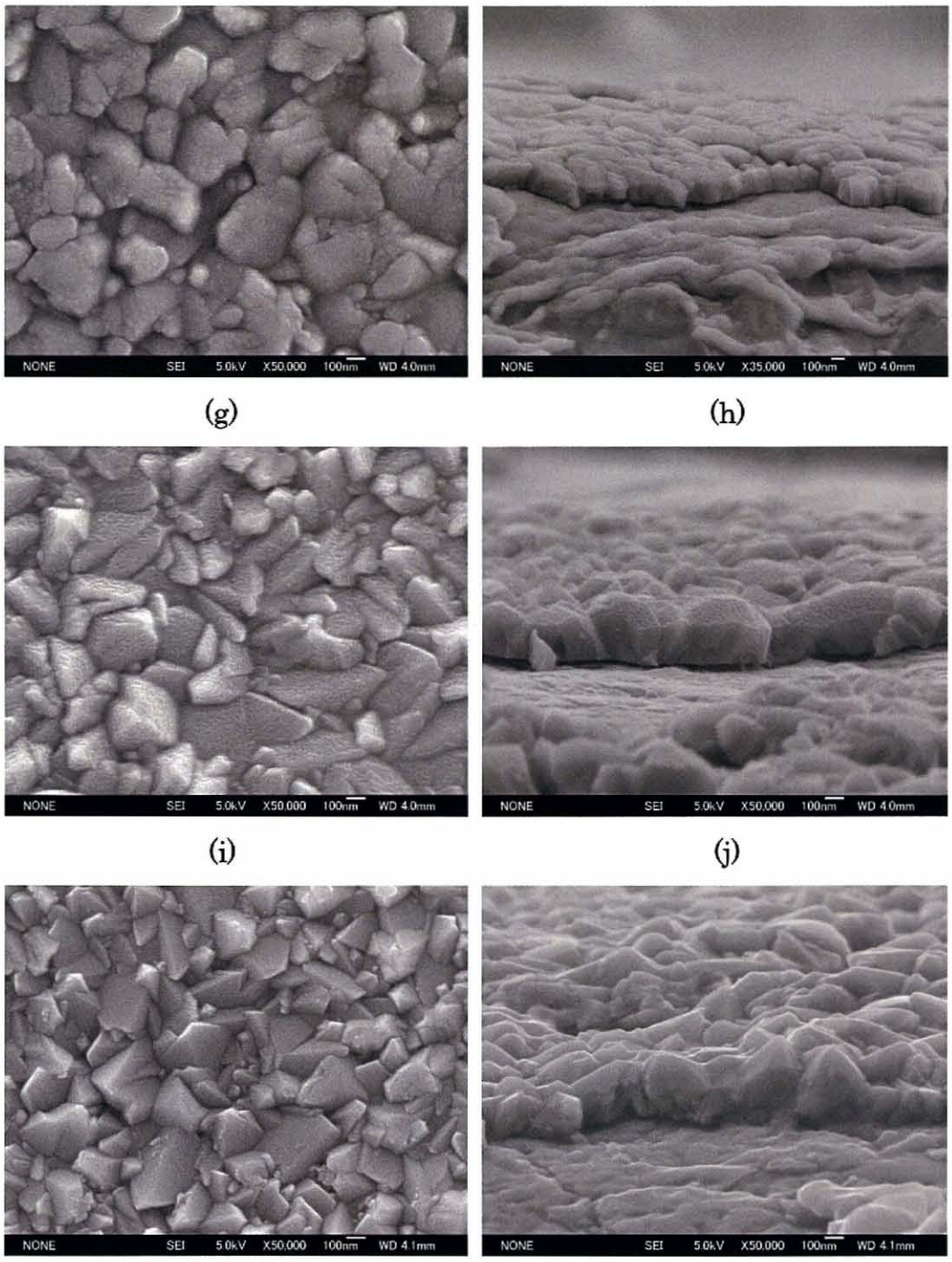

Fig. 3.9b Surface (g,i,k) and cross-sectional (h,j,l) SEM images of the TiO_2 film deposited on Ti in 150 Pa at the deposition temperature of 673 K. (g,h) deposited for 9 min with 50 sccm, (i,j) deposited for 15 min with 50 sccm, (k,l) deposited for 3 min with 15 sccm

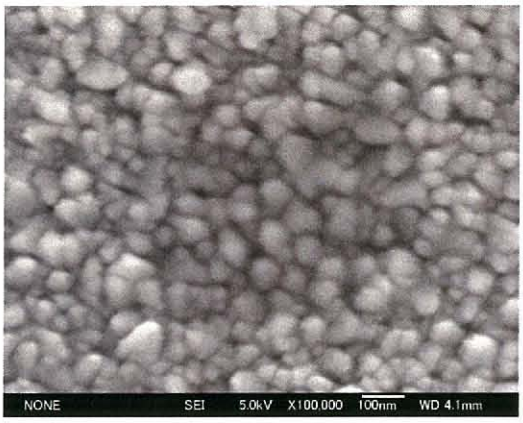
NONE SEI 5.0kV X100,000 100nm WD 4.1mm

(m)

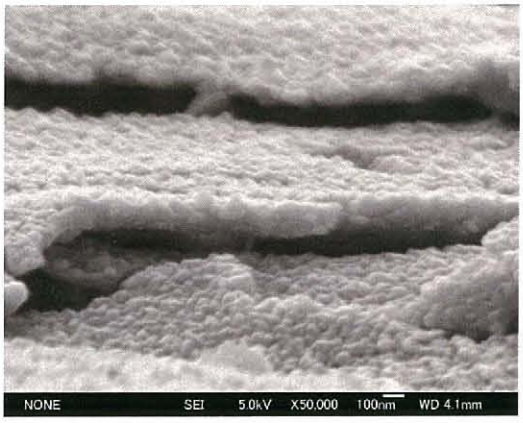
NONE SEI 5.0kV X50,000 100nm WD 4.1mm

(n)


NONE SEI 5.0kV X50,000 100nm WD 4.0mm

(o)

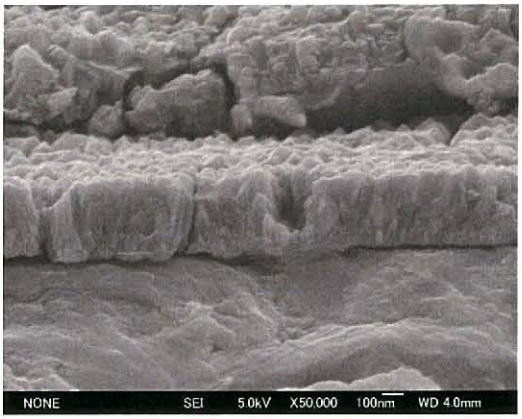
NONE SEI 5.0kV X50,000 100nm WD 4.0mm

(p)


NONE SEI 5.0kV X100,000 100nm WD 4.1mm

(q)


NONE SEI 5.0kV X50,000 100nm WD 4.1mm

(r)

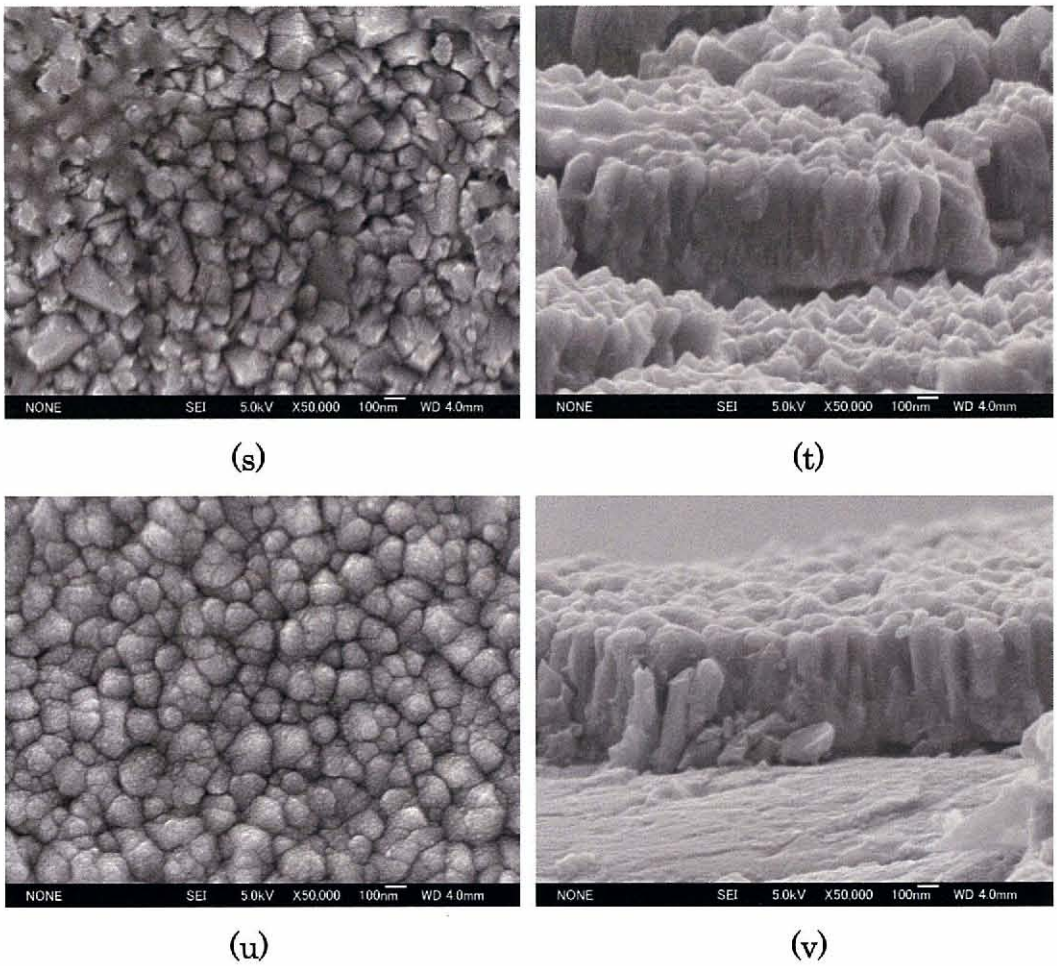

Fig. 3.9c Surface (m,o,q,s,u) and cross-sectional (n,p,r,t,v) SEM images of the TiO_2 film deposited on Ti in 150 Pa at the deposition temperature of 773 K. (m,n) deposited for 5 min with 50 sccm, (o,p) deposited for 6 min with 50 sccm, (q,r) deposited for 8 min with 25 sccm, (s,t) deposited for 15 min with 25 sccm, (u,v) deposited for 15 min with 15 sccm

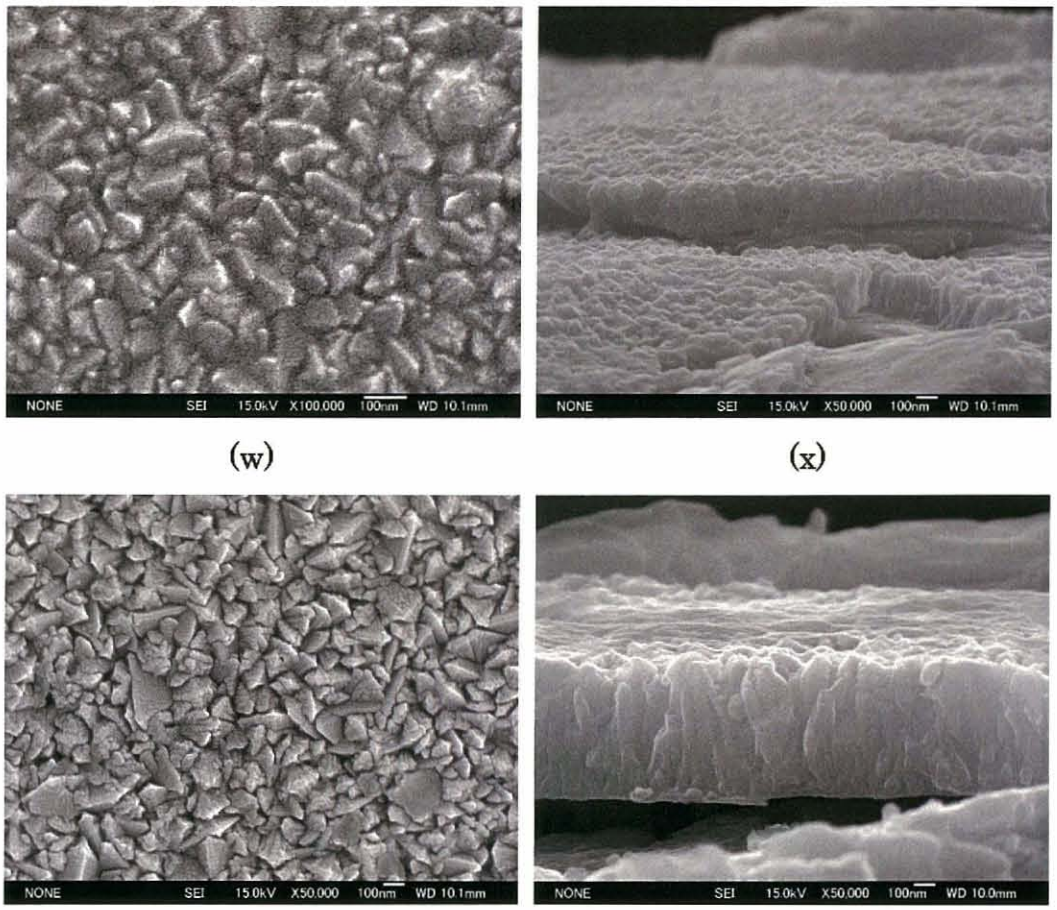

Fig. 3.9d Surface (w,y) and cross-sectional (x,z) SEM images of the TiO_2 film deposited on Ti in 150 Pa at the deposition temperature of 873 K. (w,x) deposited for 1 min with 50 sccm, (y,z) deposited for 3 min with 50 sccm

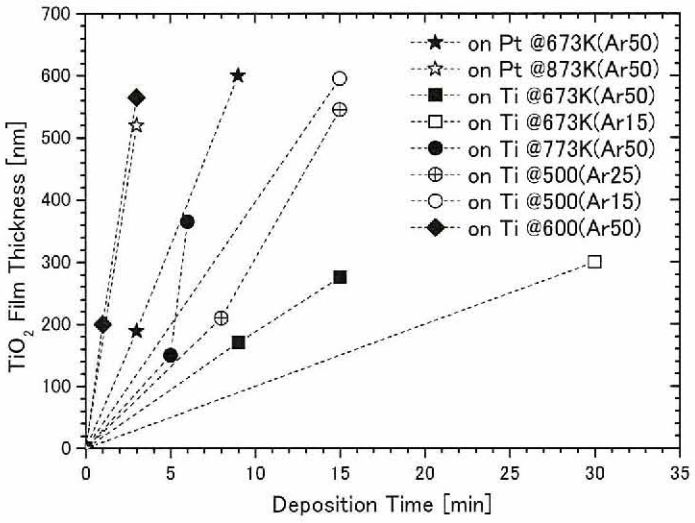

Fig. 3.10 TiO_2 film thickness versus deposition time for the exposures of 150 Pa on Pt and Ti substrates.

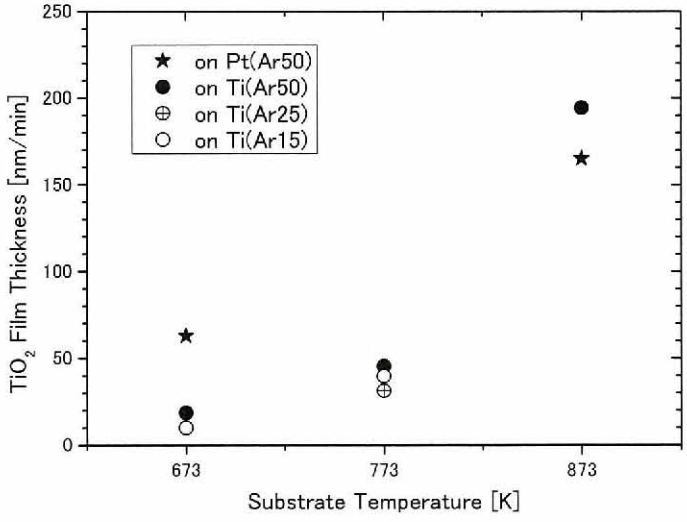

Fig. 3.11 TiO_2 film thickness versus deposition temperature for the exposures of 150 Pa on Pt and Ti substrates.

The preparation conditions and the sample characteristics of ZrO_2 films deposited on fused silica substrates are summarized in Table 3.2. From the morphology and the adhesion between film and substrate, the deposition conditions on borosilicate glass for thermal conductivity measurement were determined to be 723 K for the deposition temperature and 353 K for the preheating temperature. The surface and cross-sectional SEM images of six typical specimens of the products in the several deposition conditions are shown in Fig.3.12. The morphology of the surface shows a similar rough circle texture. However the morphology of the cross-section shows a different tendency. In the films deposited in the total pressure of 160 Pa, the number of the grain boundaries increased when increasing the deposition temperature. The morphology of the films deposited in 160 Pa was changed from a granule texture deposited at 673 K to a columnar texture deposited at 873 K. On the other hand, the number of the grain boundary was decreased when increasing the deposition temperature in the film deposited under the total pressure of 660 Pa. The morphology of the films deposited in 660 Pa was changed from a columnar texture deposited at 673 K to a cauliflower-shaped texture deposited at 773 K. Figure 3.13 shows the ZrO_2 film thickness versus deposition temperature for exposure of 160 Pa and 660 Pa for an hour. The ZrO_2 growth was not measurable at $T<573$ K in the present study. The film growth was increased when increasing the deposition temperature in the temperature range of $573 > T > 723$ K (reaction-limited region). At $T>723$ K, the film growth was saturated (diffusion-limited region). The film growth shows a similar dependency on total pressure. The thickness of the ZrO_2 films deposited in 660 Pa is slightly higher than the thickness of the ZrO_2 films deposited in 160 Pa. The Arrhenius plot of the ZrO_2 growth rate versus T^{-1} is shown in Fig.3.14. The activation energy was determined to be 54.9 kJ mol^{-1} for the total pressure of 160 Pa and 50.5 kJ mol^{-1} for the total pressure of 660 Pa.

Table 3.2 Preparation conditions, structural characteristics and room temperature thermal conductivity values of ZrO_2 films.

Deposition temperature [K]	Preheating temperature [K]	Total pressure [Pa]	Cross sectional morphology	adhesion	Film thickness [μm]
573	353	160	Smooth	×	0.1
623	353	160	Smooth	×	2.0
673	353	160	Granular	○	4.5
673	433	160	Granular	×	2.9
723	353	160	Granular	○	8.7
773	353	160	Granular	×	8.5
873	353	160	Columnar	×	8.1
623	353	660	Smooth	×	2.8
673	353	660	Columnar	△	5.5
723	353	660	Cauliflower	○	10.7
773	353	660	Cauliflower	×	10.5

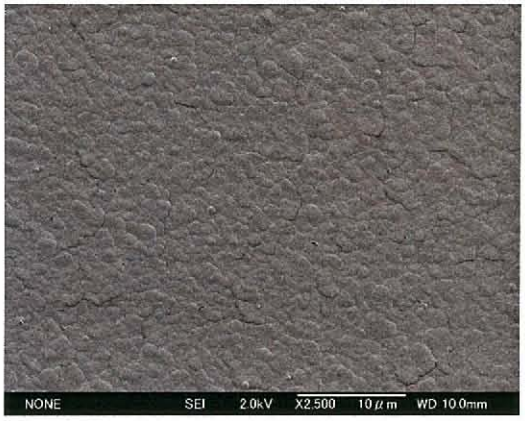
NONE SEI 2.0kV X2,500 10μm WD 10.0mm

(a)

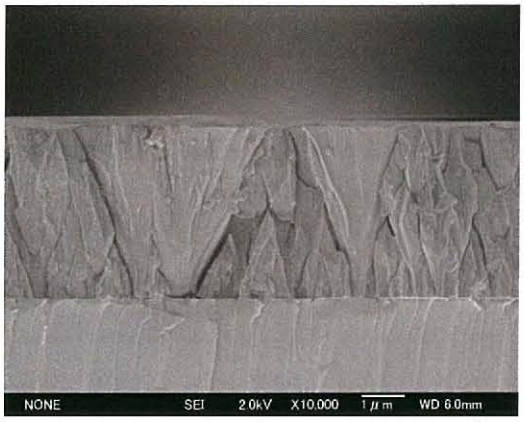
NONE SEI 2.0kV X10,000 1μm WD 6.0mm

(b)

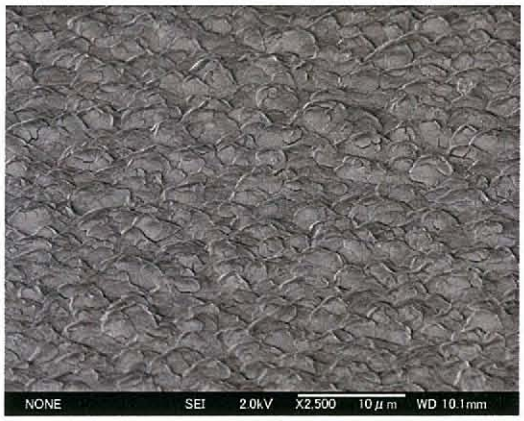
NONE SEI 2.0kV X2,500 10μm WD 10.1mm

(c)

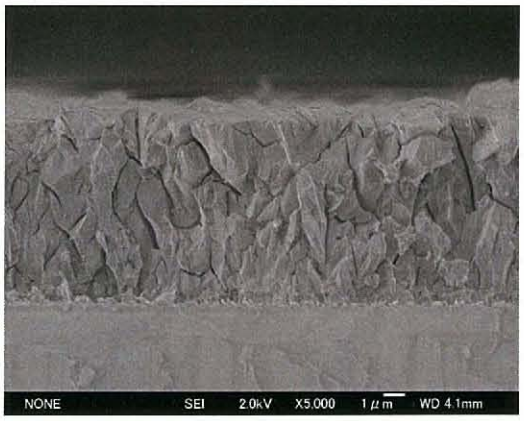
NONE SEI 2.0kV X5,000 1μm WD 4.1mm

(d)


NONE SEI 2.0kV X10,000 1μm WD 4.1mm

(e)

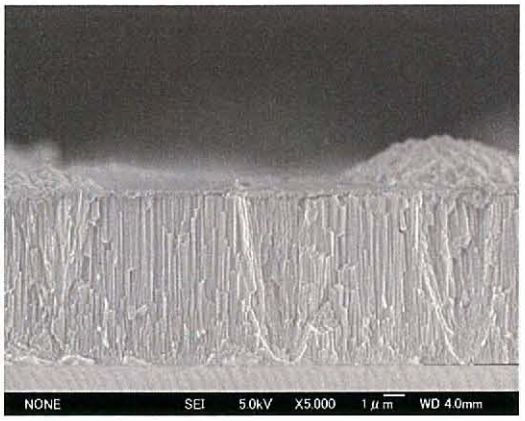
NONE SEI 5.0kV X5,000 1μm WD 4.0mm

(f)

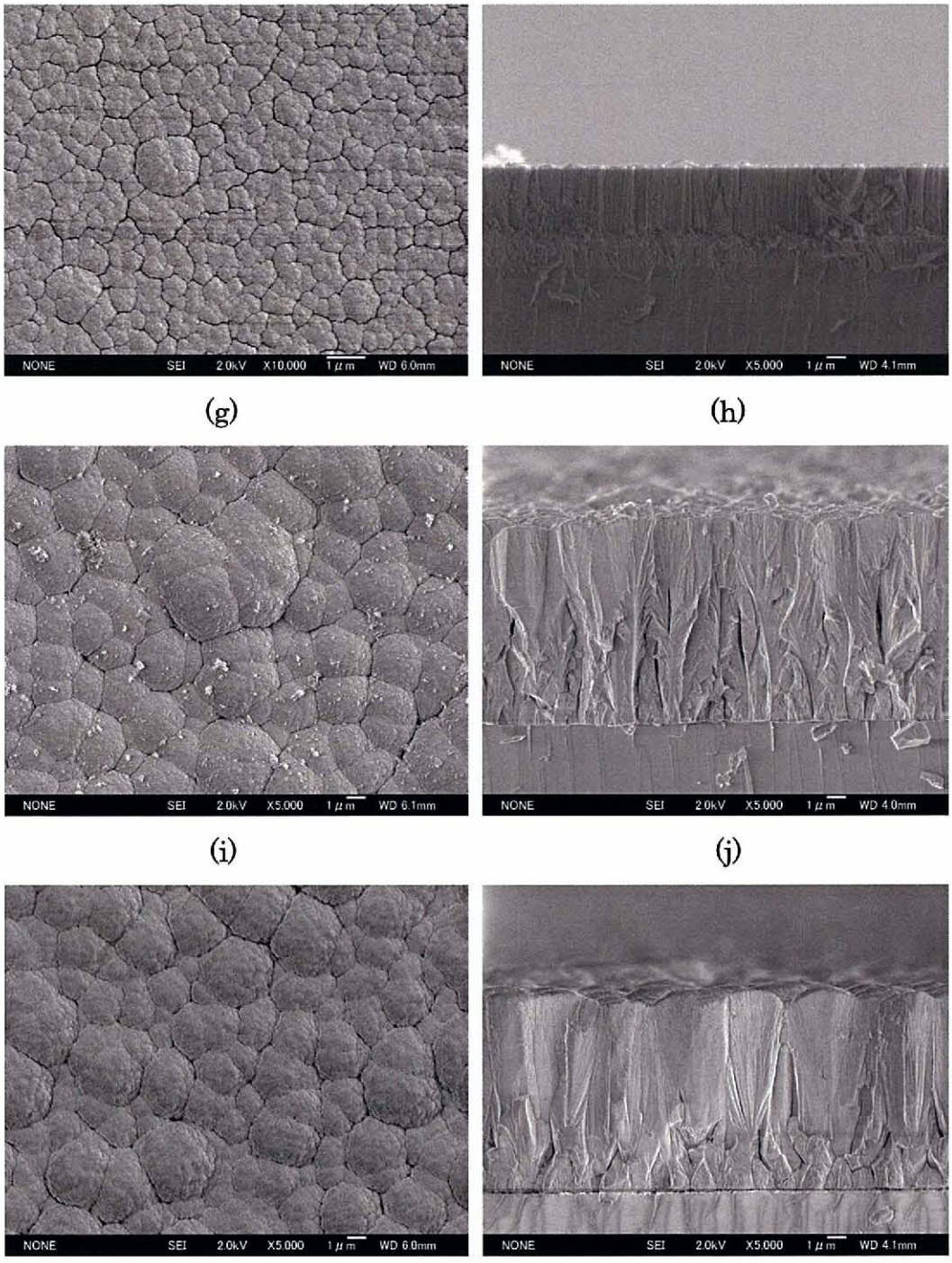

Fig. 3.12 Surface (a,c,e,g,i,k) and cross-sectional (b,d,f,h,j,l) SEM images of the ZrO_2 films deposited at the deposition temperature of 673-873 K at 150 Pa and 660 Pa on fused silica. (a,b) 673 K, 160 Pa, (c,d) 723 K, 160 Pa, (e,f) 873 K, 160 Pa, (g,h) 673 K, 660 Pa, (i,j) 723 K, 660 Pa, (k,l) 773 K, 660 Pa

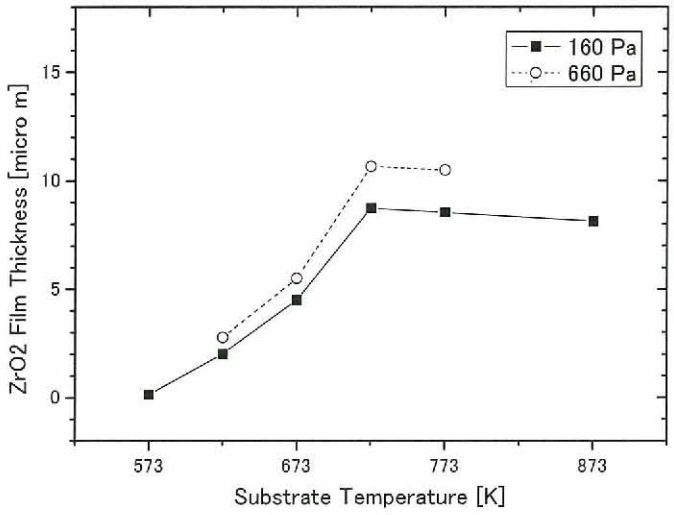

Fig. 3.13 ZrO_2 film thickness versus deposition temperature for the exposures of 160 Pa and 660 Pa on fused silica.

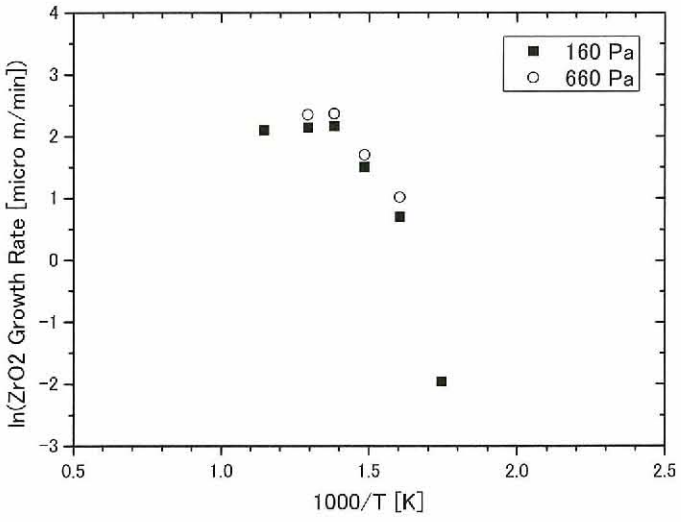

Fig. 3.14 Arrhenius plot of ZrO_2 growth rate versus T^{-1} for the exposures of 160 Pa and 660 Pa on fused silica.

Figure 3.15 shows the surface and cross-sectional SEM images of the ZrO_2 films deposited on borosilicate glass at the deposition temperature of 723 K in 160 Pa and 660Pa. The morphology was a similar texture to the ZrO_2 films deposited on fused silica substrates, the film deposited in 160 Pa and 660 Pa. The morphology of the films deposited in 160 Pa and 660 Pa was a granule texture and a cauliflower-shaped texture, respectively. The film thickness deposited in 160 Pa and 660 Pa was 8.3 μm and 8.8 μm, respectively.

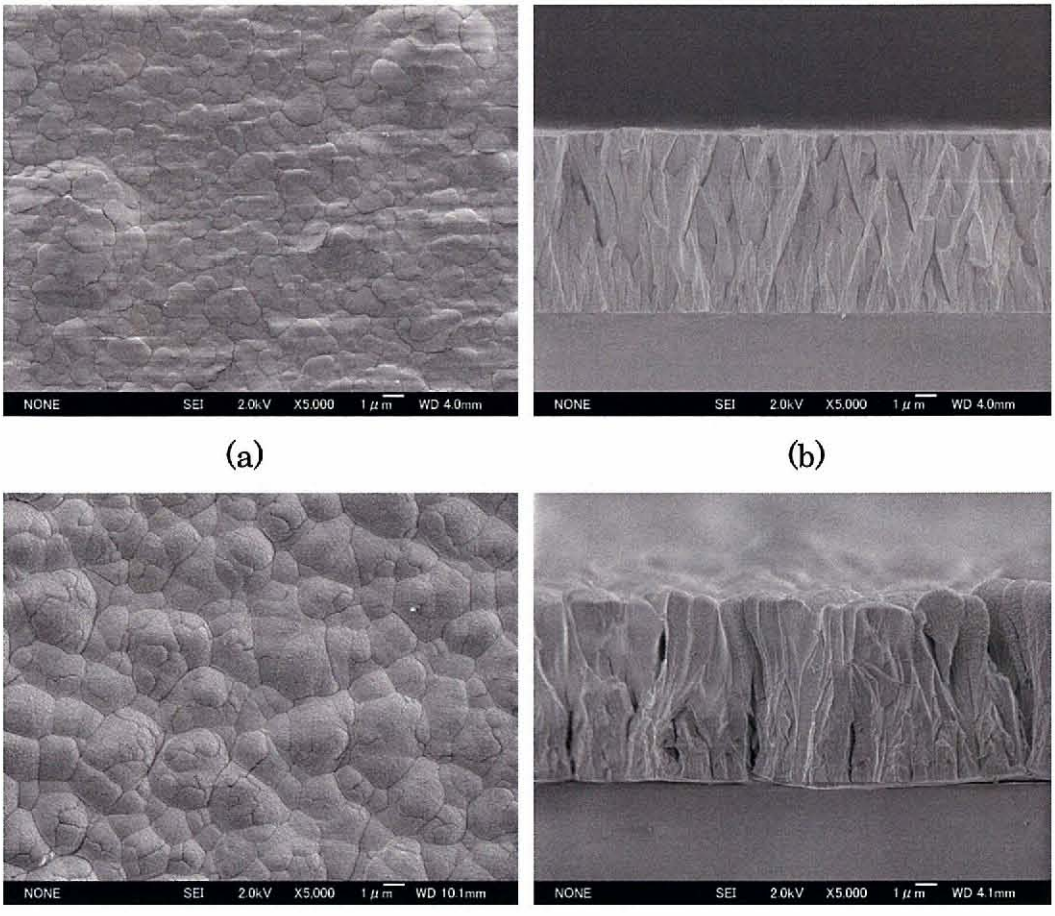

Fig. 3.15 Surface (a,c) and cross-sectional (b,d) SEM images of the ZrO_2 films deposited in 160 Pa (a,b) and 660 Pa (c,d) at the deposition temperature of 723 K on borosilicate glass for 1 hour.

3.3.2. Characteristics

Figure 3.16 shows XRD patterns of the TiO_2 films deposited at 150 Pa and 660 Pa on borosilicate glasses at the deposition temperature of 873 K. The deposition time was 1-3 hours with literature data [23,24]. From the XRD patterns, it is confirmed that the TiO_2 films exhibit anatase structures highly oriented to the (220) direction (70.3 degrees). The films deposited on fused silica substrate had similar anatase structures.

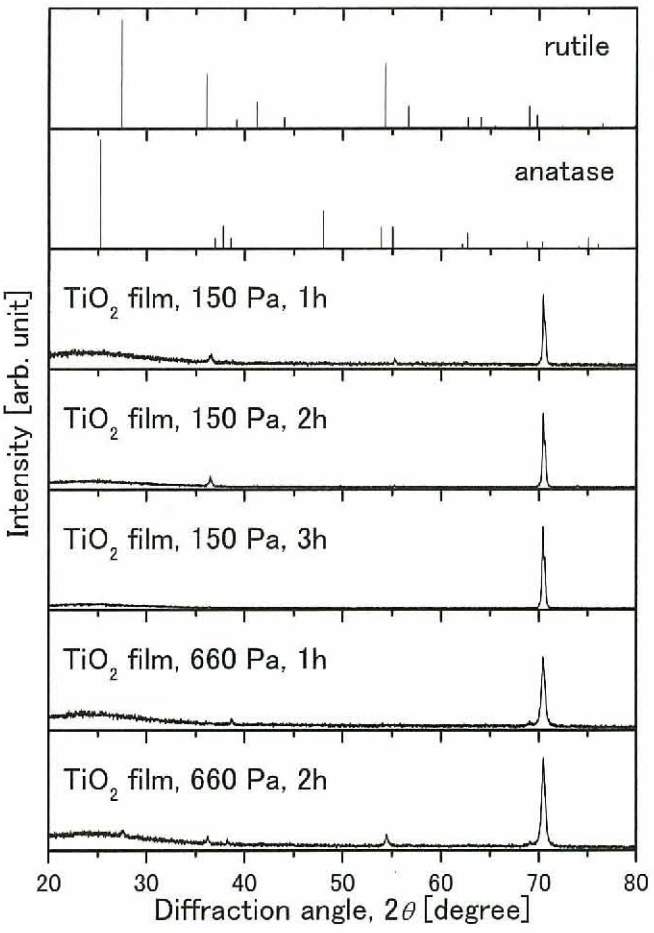

Fig. 3.16 XRD patterns of the TiO_2 films deposited at 150 Pa and 660 Pa. The deposition time and the substrates were 1-3 hours and borosilicate glass, respectively.

Figure 3.17 shows XRD patterns of the TiO_2 films deposited on Pd substrate at 150 Pa at 673 and 873 K deposition temperatures with published data [23-25]. From the XRD patterns, it is confirmed that the TiO_2 films exhibit polycrystalline anatase structures. The diffraction peaks attributed to the Pd substrate was also detected.

XRD patterns of the TiO_2 films deposited on Ti substrate at 150 Pa at 673 K of deposition temperature are shown in Fig. 3.18(a) with published data [23,24,26]. Whole films deposited at 673 K are identified as polycrystalline anatase structures. The diffraction peaks attributed to the Ti substrate were also detected.

Figure 3.18(b) shows XRD patterns of the TiO_2 films deposited on Ti substrate at 150 Pa at 773 K of deposition temperature with published data [23,24,26]. The films deposited at 773 K are anatase structure and rutile structure, which are indicated as compatible phases. The ratio of the rutile structure is increasing with the increase of the deposition temperature. The diffraction peaks attributed to the Ti substrate were also detected. The increment of rutile content in TiO_2 film decomposed from isopropyl titanate was reported [27]. In the present study, the variance of rutile content was not clearly determined.

Figure 3.18(c) shows XRD patterns of the TiO_2 films deposited on Ti substrate at 150 Pa at 873 K of deposition temperature with published data [23,24,26]. The films deposited at 873 K are anatase structure and rutile structure, which are indicated as compatible phases. The ratio of rutile structure is increasing with the increase of the deposition temperature. The diffraction peaks attributed to the Ti substrate were also detected.

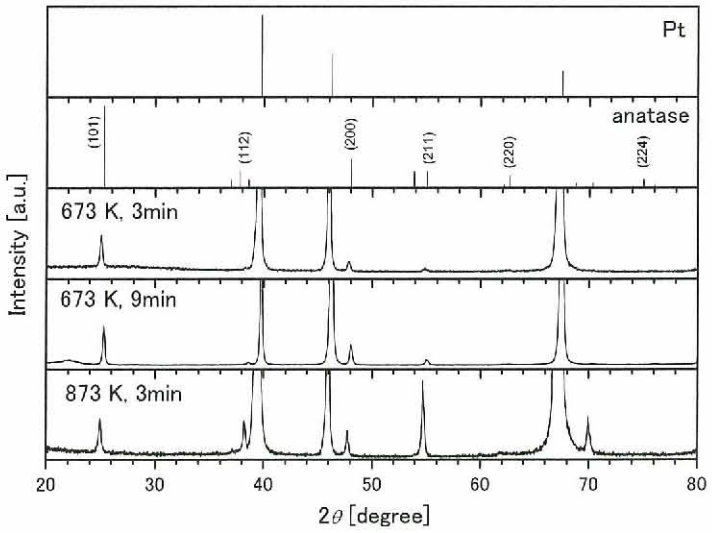

Fig. 3.17 XRD patterns of the TiO_2 films deposited on Pd substrate at 150 Pa.

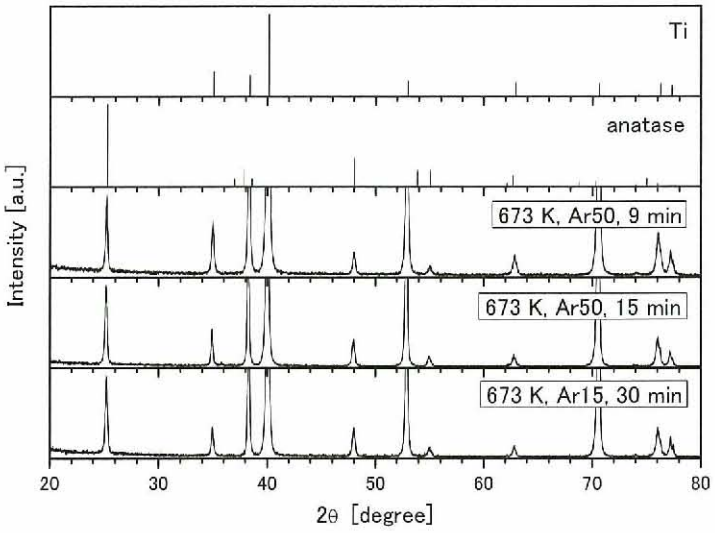

Fig. 3.18(a) XRD patterns of the TiO_2 films deposited on Ti substrate at 150 Pa in 673 K of substrate temperature.

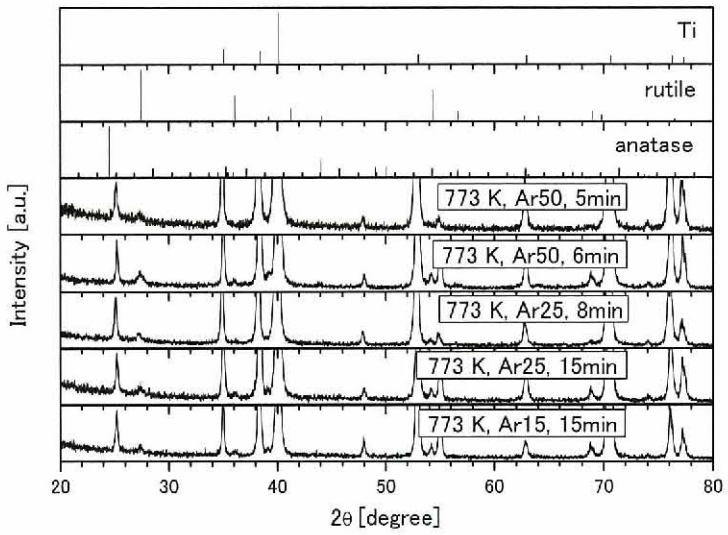

Fig. 3.18(b) XRD patterns of the TiO_2 films deposited on Ti substrate at 150 Pa in 773 K of substrate temperature.

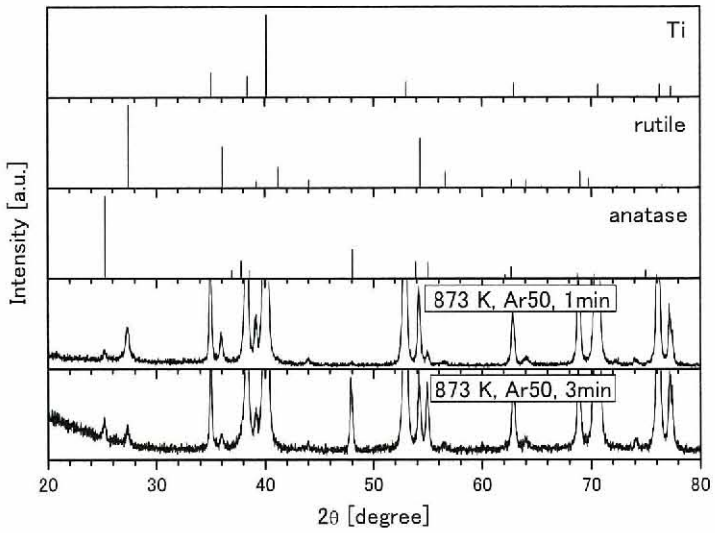

Fig. 3.18(c) XRD patterns of the TiO_2 films deposited on Ti substrate at 150 Pa in 873 K of substrate temperature.

Figure 3.19 shows XRD patterns of the ZrO_2 films deposited at 160 Pa and 660 Pa on fused silica at the deposition temperature of 673 K and 723 K for 1 hour with published data [28,29]. From the XRD patterns, the crystal structure could not be definitely determined. However it has been confirmed that the monoclinic structure was formed slightly higher than the tetragonal structure in the deposition at a lower temperature (a deposition temperature of 673 K), and the obtained tetragonal structure was slightly higher than the monoclinic structure in the ZrO_2 films deposited at a higher temperature (a deposition temperature of 723 K). The ZrO_2 film deposited at 673 K in 160 Pa was not identified the structure because there is a narrow peak around 30 degrees of the diffraction angle. However the ZrO_2 films deposited at 723 K seem to have a tetragonal structure. Therefore the ZrO_2 films for the thermal conductivity measurement were prepared with using a deposition temperature of 723 K.

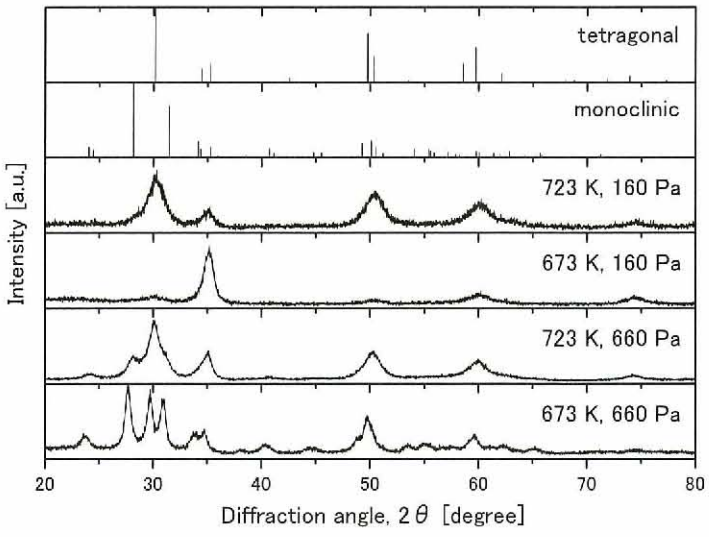

Fig. 3.19 Comparison of XRD patterns of ZrO_2 films deposited at various deposition temperatures.

The film densities on the fused silica and borosilicate glass were evaluated based on the deposition area, the film thickness, and the weight change before and after the deposition. All the films have similar densities: approximately 80-85% of the theoretical density. The results are in remarkable agreement with the back calculated density from the RBS results. A quantitative analysis of the amount of oxygen and amount of carbon impurities in the films was performed using RBS and NRA measurements. The back scatterings used in the present study are expressed by the following equations,

$$^{90}_{40}Zr(p,p_0)Zr \quad (3.15)$$

$$^{48}_{22}Ti(p,p_0)Ti \quad (3.16)$$

$$^{16}_{8}O(p,p_0)O \quad (3.17)$$

$$^{12}_{6}C(p,p_0)C \quad (3.18)$$

where p is irradiated proton and p_0 is proton in the reaction without gamma radiation. The energy of proton detected at an angle of 160 degrees of the reactions, eq.3.15, eq.3.16, eq.3.17 and eq.3.18, are 2490.31 keV, 2389.69 keV, 2039.54 keV and 1880.35 keV, respectively. The nuclear reactions used in the present study are expressed by the following equations,

$$^{12}_{6}C(d,p_0)^{13}_{6}C \quad (3.19)$$

$$^{16}_{8}O(d,p_0)^{17}_{8}O \quad (3.20)$$

$$^{16}_{8}O(d,p_1)^{17}_{8}O \quad (3.21)$$

where d is irradiated deuteron and p_1 is proton in the reaction with gamma radiation. The energy of proton detected at an angle of 140 degrees and the cross section of the reactions, eq.3.19, eq.3.20 and eq.3.21, are 3038.82 keV, 2454.55 keV and 1666.03 keV (gamma radiation: 870.7 keV) and 28.2 mb, 1.0 mb and 11.04 mb, respectively. The proton's kinetic energy drops 2752.19 keV, 2116.04 keV and 1202.54 keV by the Al filter (12.5 μm thickness) located in front of the detector, respectively. Figure 3.20 shows the comparison of yield obtained under 2.6 MeV-p+ irradiation of TiO_2 samples at an angle of

160 degrees with no filter. Figure 3.21, Figure 3.22 and Figure 3.23 shows the depth profile of density in the TiO_2 bulk sample, TiO_2 film deposited in 150 Pa and TiO_2 film deposited in 660 Pa calculated from RBS profiles. The back calculated density from the RBS results are in remarkable agreement with the geometric measured density. The authors evaluated the composition of each of the six samples: bulk TiO_2 (as a reference sample), TiO_2 film deposited at 150 Pa (dense texture film), TiO_2 film deposited at 660 Pa (feather-like texture film), bulk ZrO_2 (as a reference sample), ZrO_2 film deposited at 160 Pa (granule texture film), and ZrO_2 film deposited at 660 Pa (cauliflower-shaped texture film). The amounts of oxygen were comparable among the samples from RBS and NRA measurements. The values of O/Ti of the films deposited at both 150 Pa and 660 Pa were 2.06 ± 0.01. The values of O/Zr of the films deposited at 150 Pa and 660 Pa were 1.81 ± 0.01 and 1.77 ± 0.01, respectively. Figure 3.24 shows the comparison of yield obtained under 1.0 MeV-d+ irradiation of TiO_2 samples at an angle of 140 degrees with the Al filter. The amounts of carbon impurities differed slightly: the feather-like textured TiO_2 film contains over 2200 ± 13 ppm, while the dense-textured TiO_2 film and bulk TiO_2 contain approximately 300 ± 6 and 700 ± 7 ppm from the NRA measurement, respectively. Figure 3.25 shows the comparison of yield obtained under 1.0 MeV-d+ irradiation of ZrO_2 samples at an angle of 140 degrees with the Al filter. The cauliflower-shaped textured ZrO_2 film contains over 3300 ± 18 ppm, while the granule textured ZrO_2 film and bulk ZrO_2 contain approximately 500 ± 7 and 800 ± 7 ppm from the NRA measurement, respectively. The reason for the difference in carbon impurity between the feather-like texture of the TiO_2 film and the cauliflower-shaped texture of the ZrO_2 film, and the dense texture of the TiO_2 film and the granule texture of the ZrO_2 film is associated with the increasing film growth rate deposited at 660 Pa compared with 150 Pa. The decomposition of the precursor may not be completed. Therefore it seems that a higher impurity is immobilized in the film deposited at 660

Pa. Cameron et al. studied the reaction mechanism with Auger and infrared analysis [30]. ZrO_2 films were grown in the milliTorr range on Si(100) using ZTB. The carbon levels in the ZrO_2 film increased with increasing deposition temperature. It seems that the higher deposition rate leads to more carbon revels in the film deposited by MOCVD.

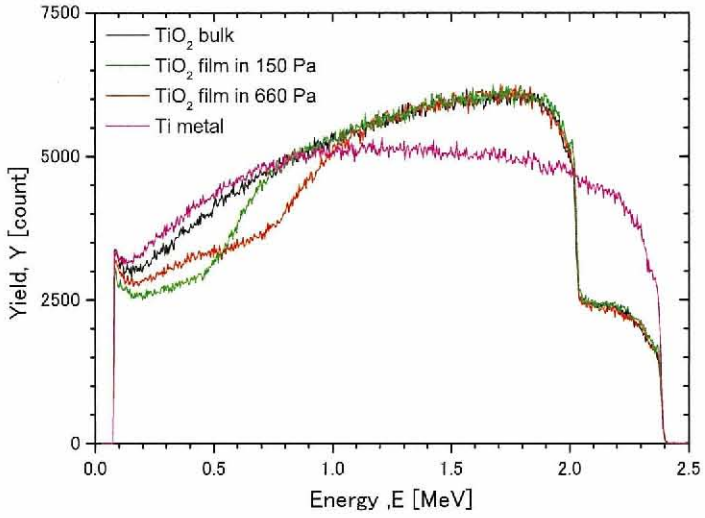

Fig. 3.20 Comparison of yield obtained under 2.6 MeV-p+ irradiation of TiO_2 samples at an angle of 160 degrees with no filter

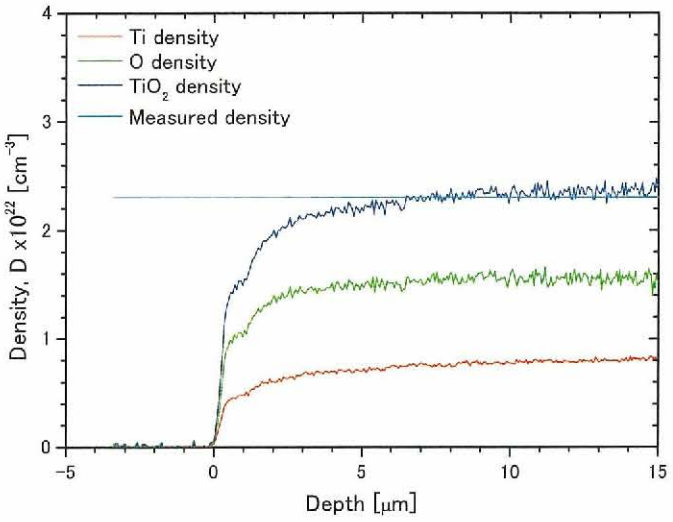

Fig. 3.21 Depth profile of density in TiO_2 bulk sample calculated from the RBS profile

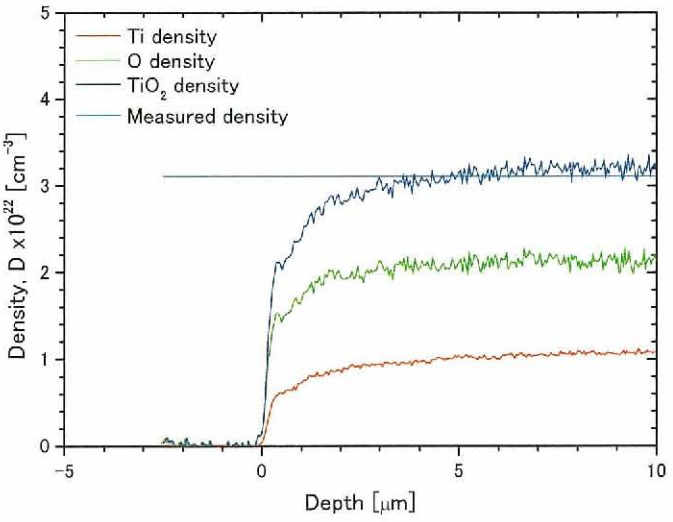

Fig. 3.22 Depth profile of density in TiO_2 film deposited in 150 Pa calculated from the RBS profile

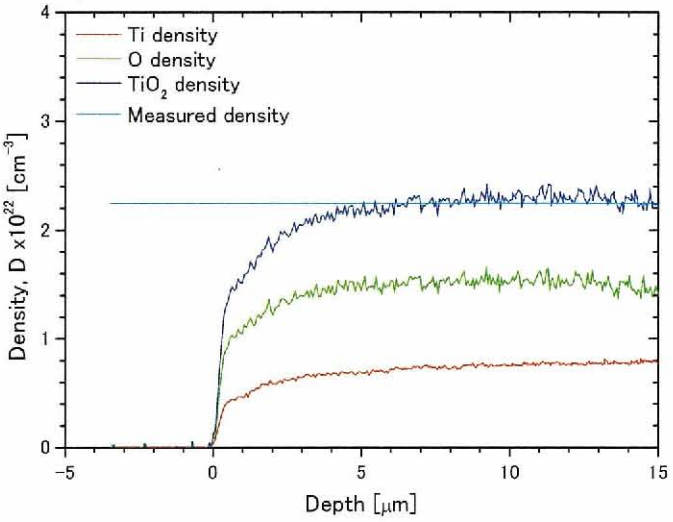

Fig. 3.23 Depth profile of density in TiO_2 film deposited in 660 Pa calculated from the RBS profile

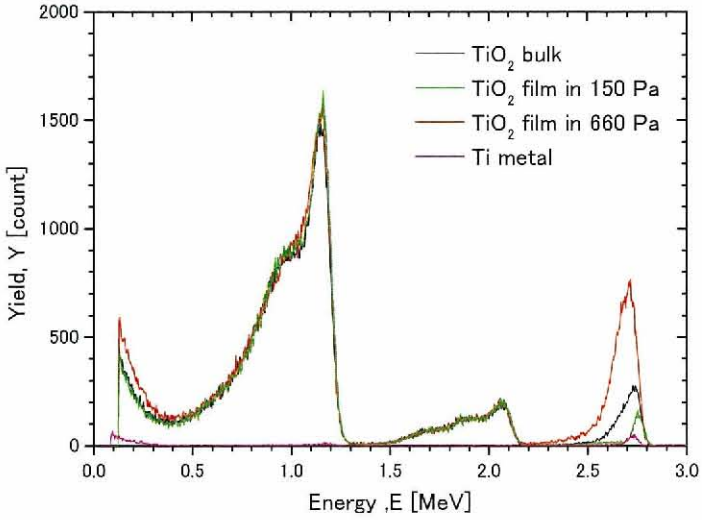

Fig. 3.24 Comparison of yield obtained under 1.0 MeV-d+ irradiation of TiO_2 samples at an angle of 140 degrees with the Al filter

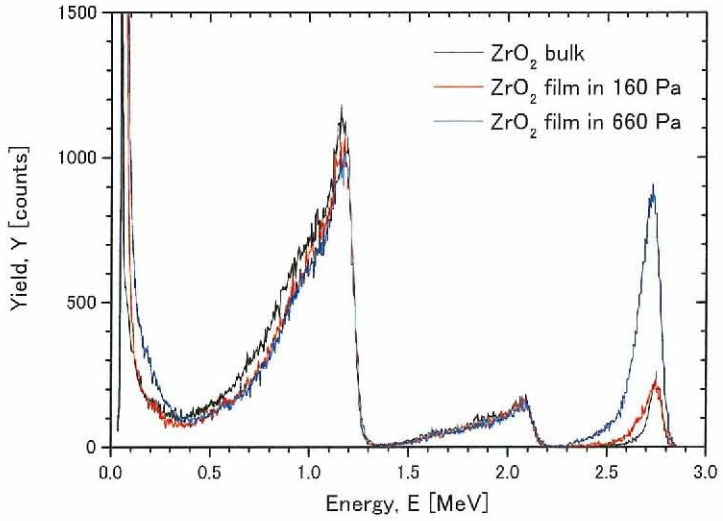

Fig. 3.25 Comparison of yield obtained under 1.0 MeV-d+ irradiation of ZrO_2 samples at an angle of 140 degrees with the Al filter

3.3.3. Thermal properties of oxide films

Figure 3.26 shows the thermal conductivity of the TiO_2 films deposited in 150 Pa and 660 Pa as a function of temperature. The thermal conductivity varies dramatically, depending on the microstructure. The thermal conductivity of the dense-textured TiO_2 films deposited at 150 Pa is approximately 6.0 $Wm^{-1}K^{-1}$ at room temperature, slightly below that of bulk TiO_2, which is 8.5 $Wm^{-1}K^{-1}$ [31]. This is caused by the low density of the films (80-85% T.D.) compared with that of the bulk sample (100% T.D.). The substrate-free TiO_2 film deposited at 150 Pa indicates the same tendency of the dense-textured TiO_2 films on the borosilicate glass substrate, indicating that the substrate has no influence on the thermal conductivity measurement. On the other hand, the thermal conductivity of the feather-like textured TiO_2 films deposited at 660 Pa is extremely low: approximately 0.5 $Wm^{-1}K^{-1}$ at room temperature. The thermal conductivity of the dense-textured TiO_2 films exhibits a T^{-1} temperature dependence,

indicating typical phonon conduction behavior. On the other hand, the thermal conductivity of the feather-like textured TiO_2 films exhibits a nearly flat temperature dependence. Thin film materials are typically deposited under nonequilibrium conditions that lead to microstructures unobtainable in bulk form. The minimum thermal conductivity shows the lowest possible thermal conductivity for the material. The estimated minimum thermal conductivity is 2.07 $Wm^{-1}K^{-1}$ around room temperature. The calculated thermal conductivities of grain sizes of 17 nm and 4 nm using anharmonic phonon-scattering rates determined from bulk crystal data are approximately 6 $Wm^{-1}K^{-1}$ and 5 $Wm^{-1}K^{-1}$ [32]. The measured thermal conductivity of the feather-like textured TiO_2 films deposited at 660 Pa is extremely lower than the published data: approximately 0.5 $Wm^{-1}K^{-1}$ at room temperature. Mun et al. investigated the heat treatment effect of thermal conductivity of TiO_2 film prepared by RF sputtering [33]. In the paper, the thermal conductivity of in-plain direction increased when increasing the grain size and the density of the heat treated films. It seems that the reduction of thermal conductivity is related to the grain boundary. Hasselman et al. reported that microcracks with preferred orientations as a function of the heat flow direction have the highest relative effect on physical properties, such as thermal conductivity [34]. Microcracks oriented perpendicular to the heat flow direction could reduce the in-plane thermal conductivity to less than one-tenth that of crack-free material. The feather-like texture films prepared in the present study contain a lot of grain boundary oriented perpendicular to the heat flow direction. One possible reason for the significant reduction of thermal conductivity in the feather-like textured TiO_2 films is the existence of grain boundaries oriented perpendicular to the heat flow direction.

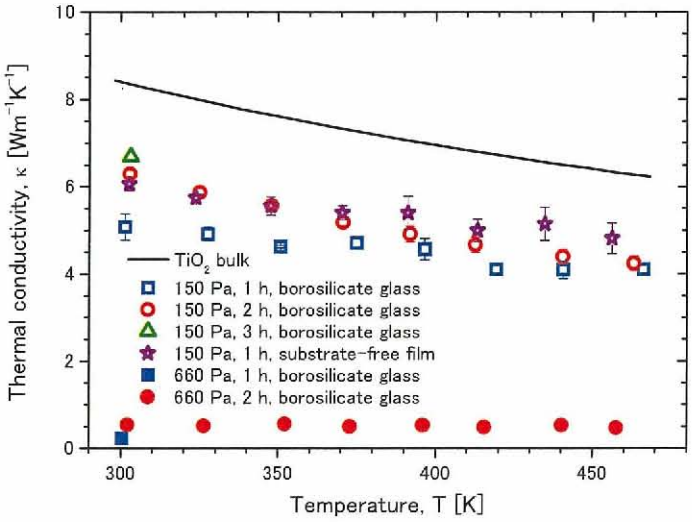

Fig. 3.26 Temperature dependence of the thermal conductivity of TiO_2 films

Figure 3.27 shows the thermal conductivity of the ZrO_2 films deposited at 160 Pa and 660 Pa as a function of temperature. The temperature dependence of thermal conductivity of ZrO_2 films shows a different tendency compared with TiO_2 films. Both films deposited in 160 Pa and 660 Pa have low thermal conductivity, between approximately half and one-quarter compared with Bulk. The thermal conductivity of the granule-textured ZrO_2 films deposited at 160 Pa and the cauliflower-shaped textured ZrO_2 film deposited at 660 Pa is approximately 0.4 $Wm^{-1}K^{-1}$ and 0.6 $Wm^{-1}K^{-1}$ at room temperature, below that of bulk ZrO_2, which is 2.6 $Wm^{-1}K^{-1}$ [35]. The low density of the films (80-85% T.D.) compared with that of the bulk sample (100% T.D.) is one reason why the low thermal conductivity is obtained. In addition, both ZrO_2 films have many grain boundaries. There are more grain boundaries in the granule texture ZrO_2 film deposited in 160 Pa compared with the cauliflower-shaped texture ZrO_2 film deposited in 660 Pa. Therefore the ZrO_2 film deposited in 160 Pa has lower thermal conductivity of in-plain direction than the ZrO_2 film deposited in 660 Pa.

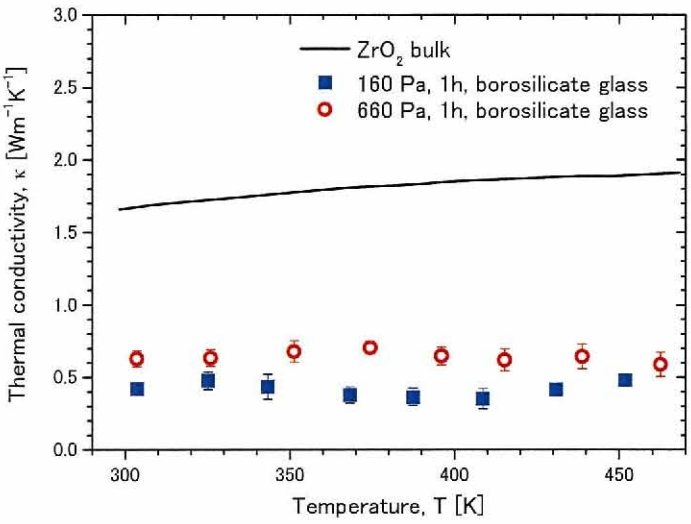

Fig. 3.27 Temperature dependence of the thermal conductivity of ZrO_2 films

3.3.4. Thermal properties of other materials

The author evaluated the thermal conductivity of a practical isotropic conductive adhesive (ICA) comprising of an epoxy-based binder containing flake-shaped and spherical Ag particles and ZYLON® HM, which consists of rigid-rod chain molecules of poly(p-phenylene-2,6-benzobisoxazole) (PBO). ICA has been expected to be the prime candidate for interconnecting materials in advanced electronics packaging systems. ZYLON® HM developed by TOYOBO is a new high-performance fiber used for a wide range of application areas, such as protective cloths for flames or sparks, sports, aerospace, industrial materials, and so on, because it has the best intensity among the existing organic fibers and a decomposition temperature of 923 K. ICA film specimens and ZYLON® HM fibers were provided by Inoue [36] and Yamanaka [37], respectively.

The ICA film specimens are composed by an epoxy-based binder containing Ag filler flake-shaped and spherical particles. In the ICA film specimens, the values of thermal conductivity in the horizontal direction

were higher than those in the vertical direction because the flake-shaped filler particles in the ICA film specimens oriented parallel to the horizontal direction (in-plane direction) of the film specimens and perpendicular to the vertical direction of the film specimens. Therefore the quality of the percolation network formed by the filler particles influenced the thermal conductivity of the ICA film specimens. The detailed results were reported in the published paper by Inoue [36].

For the thermal conductivity evaluation of ZIRON® HM in the length direction, the fibers were set in a bundle flattened parallel direction to the heating laser to heat uniformly, because no signal was determined in the trial of the thermal diffusivity measurement with a single fiber. The thermal diffusivities of ZIRON® HM obtained in the present study are summarized in Table 3.3. The thermal conductivity was calculated using the reference data of heat capacity at room temperature (1.56 $Jcm^{-3}K^{-1}$) reported by Takahashi and Hatta [38]. The thermal conductivity is extremely higher than the other organic fibers in spite of the fact that ZIRON® HM is an insulator material. The reason why ZYRON® HM has high the thermal conductivity may be because of the molecular chain orientation in the length direction. Fujishiro reported the main contribution to the thermal conductivity was from phonon conduction along the molecular chain axis of fiber in the fiber and the phonon conduction was limited by boundary-like scattering over the temperature range of 10-260 K [39]. Figure 3.28 shows the temperature dependence of thermal diffusivity and thermal conductivity of ZIRON® HM in the length direction. The thermal diffusivity and thermal conductivity decrease when the temperature increases. It seems that the phonon conduction is predominant in the thermal conduction. The value around room temperature obtained in the present study is in good agreement with the reference data [38]. The thermal conductivity reported by Yamanaka, Takahashi, and Hatta was measured using steady state method. The thermal diffusivity was

calculated using the reference data of heat capacity at room temperature (1.56 $Jcm^{-3}K^{-1}$) reported by Takahashi and Hatta [38]. The evaluation of temperature dependence of the heat capacity is needed to figure out the thermal property.

Table 3.3 The thermal diffusivity and thermal conductivity of ZIRON® HM

Temperature [K]	Thermal diffusivity [mm^2s^{-1}]	Thermal conductivity [$Wm^{-1}K^{-1}$]
304	26.1 ± 2.2	40.8 ± 2.1
325	23.7 ± 1.9	36.9 ± 2.6
351	19.7 ± 1.7	30.8 ± 3.2
376	16.6 ± 1.2	25.9 ± 2.1

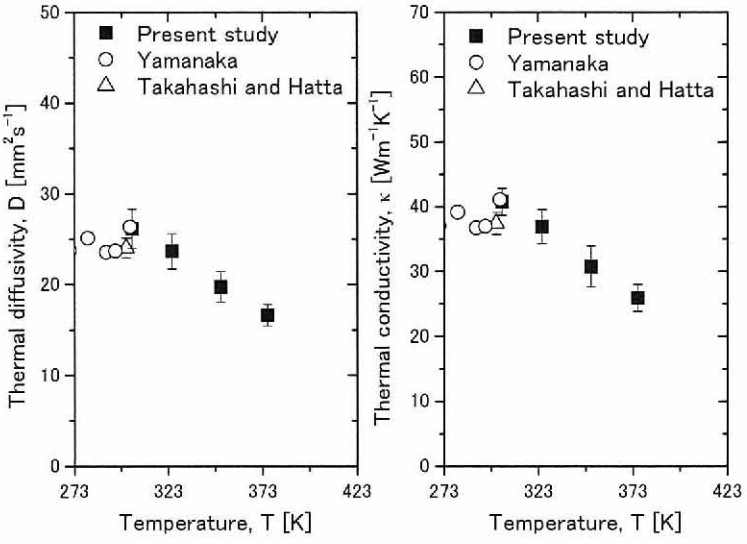

Fig. 3.28 Temperature dependence of the thermal diffusivity and thermal conductivity of ZIRON® HM in the length direction

3.4. Summary

The TiO_2 and ZrO_2 films with different morphologies were grown by MOCVD. TiO_2 films were deposited in the deposition temperature of 873 K and the pre-heated temperature of 433 K. From the XRD measurement, it is confirmed that the TiO_2 films exhibit anatase structures highly oriented to the (220) direction (70.3 degrees). The dense texture films were obtained in 150 Pa of the total pressure. On the other hand, the feather-like texture films were obtained in 660 Pa of the total pressure. The substrate-free TiO_2 film was also prepared by removing the NaCl substrate in deionized water. ZrO_2 films were deposited in around a deposition temperature of 723 K and a pre-heated temperature of 353 K. In the films deposited in the total pressure of 160 Pa, the number of grain boundaries increased when increasing the deposition temperature. The granule texture was obtained in 160 Pa at 723 K. On the other hand, the number of grain boundaries decreased when increasing the deposition temperature in the film deposited under the total pressure of 660 Pa. The morphology of the films deposited in 660 Pa at 673 K was a cauliflower-shaped texture.

A quantitative analysis of the amount of oxygen and amount of carbon impurities in the TiO_2 and ZrO_2 films were performed using RBS and NRA measurements. The amounts of oxygen were comparable among the samples. However, the amounts of carbon impurities differed slightly: the films deposited at 660 Pa contain high carbon impurities. The amounts of oxygen and carbon impurities are closely related to the deposition condition of the films.

The relationship between the microstructure and the thermal conductivity of the TiO_2 and ZrO_2 films was studied. The dense-textured TiO_2 films exhibited slightly lower thermal conductivity than that of bulk TiO_2; this was a result of the low relative density of the TiO_2 films. The feather-like textured TiO_2 films exhibited extremely low thermal conductivity -- below 0.5 $Wm^{-1}K^{-1}$ -- which is probably due to the grain

boundaries oriented perpendicular to the heat flow direction. Both the granule texture ZrO_2 film and cauliflower-shaped texture ZrO_2 film showed low thermal conductivity, approximately 0.4 $Wm^{-1}K^{-1}$ and 0.6 $Wm^{-1}K^{-1}$ at room temperature. There are more grain boundaries in the granule texture film deposited in 160 Pa compared with the cauliflower-shaped texture film deposited in 660 Pa. Therefore the film deposited in 160 Pa had lower thermal conductivity of in-plain direction than the film deposited in 660 Pa.

At the present time of writing, there is no innovative material on a development of new candidate materials with higher efficiency than YSZ. Therefore the research for a reduction of thermal conductivity from the view point of the coating technology is needed. The author has succeeded in realizing the thermal conductivity tuning in the films by controlling the microstructure. The results obtained in the present study apply to both TBC and TE designs for the development of high-performance materials. This concept of a reduction of thermal conductivity has a potential to be a practical application. For the realization, additional researches, such as a development of a high speed deposition technology of coatings with microstructures and a method of providing grain boundaries oriented perpendicular to the thickness direction is need for the future.

References

[1] N. P. Padture, M. Gell, and E. H. Jordan, "Thermal barrier coatings for gas-turbine engine applications," *Science*, **296(5566)** 280-284 (2002).

[2] D. D. Hass, A. J. Slifka, and H. N. G. Wadley, "Low thermal conductivity vapor deposited zirconia microstructures," *Acta Materialia*, **49(6)** 973-983 (2001).

[3] T. M. Tritt, "Thermoelectric materials: Holey and unholey semiconductors," *Science*, **283(5403)** 804-805 (1999).

[4] K. Sugiura, H. Ohta, K. Nomura, M. Hirano, H. Hosono, and K. Koumoto, "High electrical conductivity of layered cobalt oxide $Ca_3Co_4O_9$ epitaxial films grown by topotactic ion-exchange method," *Applied Physics Letters*, **89(3)** 032111/1-3 (2006)

[5] C. P. Fictorie, J. F. Evans, and W. L. Gladfelter, "Kinetic and mechanistic study of the chemical vapor deposition of titanium dioxide thin films using tetrakis (isopropoxo) titanium (IV)," *Journal of Vacuum Science & Technology, A: Vacuum, Surfaces, and Films*, **12(4, Pt. 1)** 1108-1113 (1994).

[6] M. Anpo and M. Takeuchi, "The design and development of highly reactive titanium oxide photocatalysts operating under visible light irradiation," *Journal of Catalysis*, **216(1-2)** 505-516 (2003).

[7] Y. Ohko, T. Tatsuma, T. Fujii, K. Naoi, C. Niwa, Y. Kubota, and A. Fujishima, "Multicolor photochromism of TiO_2 films loaded with silver nanoparticles," *Nature Materials*, **2(1)** 29-31 (2003).

[8] T. Miyagi, M. Kamei, T. Mitsuhashi, and A. Yamazaki, "Superior Schottky electrode of RuO2 for deep-level transient spectroscopy on anatase TiO_2," *Applied Physics Letters*, **83(9)** 1782-1784 (2003).

[9] R. S. Sonawane, B. B. Kale, and M. K. Dongare, "Preparation and photo-catalytic activity of Fe-TiO_2 thin films prepared by sol-gel clip coating," *Materials Chemistry and Physics*, **85(1)** 52-57 (2004).

[10] M. Matsumoto, "Development of plasma-sprayed thermal barrier coatings with low thermal conductivity and high oxidation resistance," *Journal of the Ceramic Society of Japan*, **115(Feb)** 118-123 (2007).

[11] J. H. Hong, W. J. Choi, and J. M. Myoung, "Properties of ZrO_2 dielectric layers grown by metalorganic molecular beam epitaxy," *Microelectronic Engineering*, **70(1)** 35-40 (2003).

[12] G. L. Tan and X. J. Wu, "Electronic conductivity of a ZrO_2 thin film as an oxygen sensor," *Thin Solid Films*, **330(2)** 59-61 (1998)

[13] K. Choy, W. Bai, S. Charojrochkul, and B. C. H. Steele, "The development of intermediate-temperature solid oxide fuel cells for the next millennium," *Journal of Power Sources*, **71(1,2)** 361-369 (1998).

[14] O. Bernard, A.M. Huntz, M. Andrieux, W. Seiler, V. Ji, and S. Poissonnet, "Synthesis, structure, microstructure and mechanical characteristics of MOCVD deposited zirconia films," *Applied Surface Science*, **253(10)** 4626-40 (2007)

[15] A. Kitamura, T. Tamai, A. Taniike, Y. Furuyama, T. Maeda, N. Ogiwara, and M. Saidoh, "Simulation of ERD spectra for a surface with a periodic roughness," *Nuclear Instruments & Methods in Physics Research, Section B: Beam Interactions with Materials and Atoms.* **134(1)** 98 (1998).

[16] J. R. Tesmer, M. Nastasi, J. C. Barbour, C. J. Maggiore, and J. W. Mayer, *HandBook of modern ion beam materials analysis* (Materials Research Society, Pittsburgh, USA, 1995).

[17] A. Taniike, N. Kubota, M. Takeuchi, Y. Furuyama, and A. Kitamura, "Ion-irradiation induced hydrogen loss from polyethylene film," *Journal of Applied Physics*, **92(11)** 6489-6494 (2002).

[18] R. Kato, A. Maesono, and R. P. Tye, "Thermal conductivity measurement of submicron-thick films deposited on substrates by modified ac calorimetry (laser-heating Angstrom method)," *International Journal of Thermophysics*, **22(2)** 617-629 (2001).

[19] I. Hatta, R. Kato, and A. Maesono, "Development of a.c. calorimetric method for thermal diffusivity measurement. I. Contribution of thermocouple attachment in a thin sample," *Japanese Journal of Applied Physics*, **25(6)** L493-495 (1986)

[20] A. J. Angstrom, *Annalen der Physik. 2. Folge*, **114** 513 (1861)

[21] T. Yamamoto, T. Morita, T. Kurauchi, M. Hakomori, S. Misawa, T. Uchiyama, and M. Matsuura, "Preparation of SiO_2/TiO_2 multilayer by planner magnetron sputtering with an inductively coupled rf plasma," *Shinku*, **38(3)** 255-258 (1995)

[22] A. C. Jung, S. J. Kim, N. Imaishi, and Y. Cho, "Effect of TiO_2 thin film thickness and specific surface area by low-pressure metal-organic chemical vapor deposition on photocatalytic activities," *Applied Catalysis B: Environmental*, **55(4)** 253-257 (2005)

[23] JCPDS card, TiO_2 (rutile),21-1276

[24] JCPDS card, TiO_2 (anatase), 21-1272

[25] JCPDS card, Pt, 4-802

[26] JCPDS card, Ti, 5-0681

[27] Y. Takahashi, H. Suzuki, and M. Nasu, "Rutile growth at the surface of titanium oxide films deposited by vapor-phase decomposition of isopropyl titanate," *Journal of the Chemical Society, Faraday Transactions 1: Physical Chemistry in Condensed Phases*, **81(12)** 3117-3125 (1985)

[28] JCPDS card, ZrO_2 (tetragonal), 17-923

[29] JCPDS card, ZrO_2 (monoclinic), 37-1484

[30] M. A. Cameron and S. M. George, "ZrO_2 film growth by chemical vapor deposition using zirconium tetra-tert-butoxide," *Thin Solid Films*, **348(1,2)** 90-98 (1999).

[31] I. Barin, O. Knacke, and O. Kubaschewski, "Thermochemical Properties of Inorganic Substances," *Thermodynamics, Thermochemistry, and Thermal Properties*, Section 69-1 921 pp. (Springer-Verlag, New York, N. Y. 1973).

[32] S. M. Lee, D.G. Cahill, and T.H. Allen, "Thermal conductivity of sputtered oxide films," *Physical Review B: Condensed Matter*, **52(1)** 253-257 (1995)

[33] J. Mun, S. W. Kim, R. Kato, I. Hatta, S. H. Lee, and K. H. Kang, "Measurement of the thermal conductivity of TiO_2 thin films by using the thermo-reflectance method" *Thermochimica Acta*, **455(1-2)** 55-59 (2007)

[34] D. P. H. Hasselman and J. P. Singh, "Analysis of thermal stress resistance of microcracked brittle ceramics," American Ceramic Society Bulletin. **58(9)** 856-860 (1979).

[35] Y. G. Touloukian, R. W. Powell, C. Y. Ho, and P. G. Klemens, *Thermal Conductivity : Metallic Elements and Alloys*, (Thermophysical Properties of Matter, Vol. 1). 1469 pp. (IFI/Plenum, New York, N. Y., 1970)

[36] M. Inoue, H. Muta, T. Maekawa, S. Yamanaka, and K. Suganuma, "Thermal conductivity of isotropic conductive adhesives composed of an epoxy-based binder," *Conference on High Density Microsystem Design and Packaging and Component Failure Analysis, Shanghai, China, June 27-30, 2006*, 236-241 (2006).

[37] A. Yamanaka and T. Kashima, "Application of organic fiber with high thermal conductivity," *Sen'i Gakkaishi*, **56(4)** 128-132 (2000).

[38] F. Takahashi and I. Hatta, "Thermal diffusivity measurement of high-strength high-modulus super fibers," *Nippon Netsubussei Shinpojumu Koen Ronbunshu, 25th, Nagano, Japan, Oct. 20-22, 2004*, C214/1-C214/3 (2004).

[39] H. Fujishiro, M. Ikebe, T. Kashima, and A. Yamanaka, "Thermal conductivity and diffusivity of high-strength polymer fibers," *Japanese Journal of Applied Physics*, Part 1: Regular Papers, Short Notes & Review Papers, **36(9A)** 5633-5637 (1997)

Chapter 4

Concluding remarks

In the present study, the author studied the thermophysical properties of alkaline earth perovskite oxide materials and alkaline earth and yttrium oxide materials on bulk and the fabrication and characterization of TiO_2 and ZrO_2 films grown by MOCVD. The author then tried to offer the material design of low thermal conductivity materials. The purpose of this study is the development of new materials and the modification of oxides for applications, such as TBC and TE. The systematic interests of the property offer possibilities for applications of its properties in different branches of new engineering.

In the chapter 2, thermophysical properties of alkaline earth perovskite type oxides and alkaline earth and yttrium oxide materials on bulk were systematically evaluated. The results that were obtained in this study are summarized bellow:

(1) The thermal conductivity is dependent on the relation of the tolerance factor because the phonon conductivity is dependent on crystal symmetry. There are obvious correlations between the tolerance factor and elastic constants. It is considered that the symmetry of a crystal is relevant to inter ionic bonding states, therefore the tolerance factor has affected the elasticity-characteristic of the material.

(2) The thermal conductivity of most perovskites with the exception of $SrRuO_3$ decreases when temperature increases. On the other hand, the thermal conductivity of $SrRuO_3$ increases when temperature increases and molybdates have very high thermal conductivity, which indicates that the electronic contribution is predominant. In molybdates, making solid solution did not succeed in the decrease of the thermal conductivity. The thermal conductivity of $SrHfO_3$ is 5.2 $Wm^{-1}K^{-1}$ at room temperature, and it reaches to 2.5-3.0 $Wm^{-1}K^{-1}$ in high temperature. The thermal conductivity of SrY_2O_4 decreases when temperature increases. The thermal conductivity of BaY_2O_4 was 3.9 $Wm^{-1}K^{-1}$ at 298 K, and decreased when temperature increases. The values of thermal conductivity of

SrY_2O_4 at 300 and 1200 K are 7.6 and 3.4 $Wm^{-1}K^{-1}$, respectively. The thermal conductivity at high temperature is slight higher than the thermal conductivity of YSZ, around 2 $Wm^{-1}K^{-1}$. It is necessary to decrease it more to apply it as a new substitute for thermal barrier coating material, a replacement of YSZ.

(3) The average linear thermal expansion coefficients are $1.13x10^{-5}$ K^{-1} for $SrHfO_3$, $1.03x10^{-5}$ K^{-1} for $SrRuO_3$, $7.98x10^{-6}$ K^{-1} for $SrMoO_3$, and $1.09x10^{-5}$ K^{-1} for SrY_2O_4, $1.08x10^{-5}$ K^{-1} for BaY_2O_4 in the temperature range between 300 K and 1100 K, and $7.97x10^{-6}$ K^{-1} for $BaHfO_3$ in the temperature range between 300 K and 1500 K. The value of the thermal expansion of $SrHfO_3$ is slight higher than other perovskite type oxides. SrY_2O_4 and BaY_2O_4 have a potential to be utilized as TBC materials because they have high temperature stability and a large enough thermal expansion coefficient.

(4) The melting temperature of $SrHfO_3$ (3200 K) is higher than that of other perovskites, for example, the melting temperature of $SrTiO_3$ is 2170 K, and that of $SrZrO_3$ is 2883 K. For the alkaline, Ba and Sr series perovskite type oxides, the products of α_l and T_m show approximately the same value ($\alpha_l \times T_m = 0.02$). However the value of thermal expansion of $SrHfO_3$ is slight higher than the other perovskites. This particular base of thermal expansion coefficient and melting temperature has a possibility of practical use.

(5) The electrical resistivity of $SrVO_3$, $SrRuO_3$, and molybdates are respectively of an order of magnitude of 10^{-4} and 10^{-6} Ωm. The electrical resistivity of the perovskites shows positive temperature dependence, indicating metallic behavior. The Seebeck coefficient of $SrRuO_3$ and $SrMoO_3$ is positive, showing that the majority of charge carriers are holes. The Seebeck coefficient of $SrVO_3$ and $BaMoO_3$ is negative, showing that the majority of charge carrier is electron. The Seebeck coefficient values of $SrVO_3$, $SrRuO_3$, $SrMoO_3$, and $SrMoO_3$ are respectively around 10-40

μVK^{-1}, 30-40 μVK^{-1}, 30 μVK^{-1}, 4-9 μVK^{-1}. Making the solid solution of molybdates rather lower than the value in molybdate.

The author then tried to offer the material design of low thermal conductivity materials. However, the innovative TBCs require the overall performance, such as low thermal conductivity (<2 $Wm^{-1}K^{-1}$), high thermal expansion coefficient conductivity (>$9x10^{-6}$ K^{-1}), a stable phase, chemical resistance, a low sintering rate, and high fracture toughness.

In the chapter 3, the relationship between the microstructure and the thermal conductivity of the TiO_2 and ZrO_2 films with different morphologies grown by MOCVD was studied. The results that were obtained in this study are summarized bellow:

(1) TiO_2 films were deposited in the deposition temperature of 873 K and the pre-heated temperature of 433 K. From the XRD measurement, it is confirmed that the TiO_2 films exhibit anatase structures highly oriented to the (220) direction (70.3 degrees). The dense texture films were obtained in 150 Pa of the total pressure. On the other hand, the feather-like texture films were obtained in 660 Pa of the total pressure. The substrate-free TiO_2 film was also prepared by removing the NaCl substrate in deionized water.

(2) ZrO_2 films were deposited in around a deposition temperature of 723 K and a pre-heated temperature of 353 K. In the films deposited in the total pressure of 160 Pa, the number of grain boundaries increased when increasing the deposition temperature. The granule texture was obtained in 160 Pa at 723 K. On the other hand, the number of grain boundaries decreased when increasing the deposition temperature in the film deposited under the total pressure of 660 Pa. The morphology of the films deposited in 660 Pa at 673 K was a cauliflower-shaped texture.

(3) A quantitative analysis of the amount of oxygen and amount of carbon impurities in the TiO_2 and ZrO_2 films were performed using RBS and NRA measurements. The amounts of oxygen were comparable among

the samples. However, the amounts of carbon impurities differed slightly: the films deposited at 660 Pa contain high carbon impurities. The amounts of oxygen and carbon impurities are closely related to the deposition condition of the films.

(4) The dense-textured TiO_2 films exhibited slightly lower thermal conductivity than that of bulk TiO_2; this was a result of the low relative density of the TiO_2 films. The feather-like textured TiO_2 films exhibited extremely low thermal conductivity -- below 0.5 $Wm^{-1}K^{-1}$ -- which is probably due to the grain boundaries oriented perpendicular to the heat flow direction.

(5) Both the granule texture ZrO_2 film and cauliflower-shaped texture ZrO_2 film showed low thermal conductivity, approximately 0.4 $Wm^{-1}K^{-1}$ and 0.6 $Wm^{-1}K^{-1}$ at room temperature. There are more grain boundaries in the granule texture film deposited in 160 Pa compared with the cauliflower-shaped texture film deposited in 660 Pa. Therefore the film deposited in 160 Pa had lower thermal conductivity of in-plain direction than the film deposited in 660 Pa.

The author has succeeded in realizing the thermal conductivity tuning in the films by controlling the microstructure. The results obtained in the present study apply to both TBC and TE designs for the development of high-performance materials.

Acknowledgement

The author would like to express the greatest appreciation to his supervisor, Prof. Shinsuke YAMANAKA (Chief examiner), for his precious guidance, invaluable discussions, and warm encouragement.

The author would like to express his great appreciation to Prof. Toshikazu TAKEDA (Associate examiner), Prof. Takao A. YAMAMOTO (Associate examiner), Prof. Akira YAMAGUCHI (Associate examiner) and Assoc. Prof. Masayoshi UNO (Associate examiner).

The author would like to express his graceful appreciation to Prof. Akira KITAMURA, Assoc. Prof. Yuichi FURUYAMA, Assoc. Prof. Akira TANIIKE (Department of Environmental Energy Science, Faculty of Maritime Sciences, Kobe University) and Dr. Naoyoshi KUBOTA (Nippon Steal Corporation) for their lectures on nuclear physics and the widerange of discussions on chemical composition analysis using the Accelerator apparatus. Mr. Hiroki IWAI (Japan Atomic Energy Agency) and Mr. Syo KAWATSU (Graduate School of Maritime Science, Kobe University) gave the greatest support and the best suggestions in the operation.

The author would like to express his sincere appreciation to Asst. Prof. Masahiro INOUE (The Institute of Scientific and Industrial Research, Osaka University) for his kind collaboration and progressive approach.

The author wishes to gratefully acknowledge to Asst. Prof. Tadachika NAKAYAMA and Prof. Koichi NIIHARA (Extreme Energy-Density Research Institute, Nagaoka University of Technology) for their support with the sample preparations.

The author wishes to gratefully acknowledge Asst. Prof. Toshiyuki FUJII (Research Reactor Institute, Kyoto University) for his helpful advice and support on Raman spectroscopy measurements.

The author wishes to gratefully acknowledge Dr. Tetsushi MATSUDA and Mr. Shin-ichi KOBAYASHI (Nuclear Fuel Industries) for their professional support on property measurements.

The author wishes to gratefully acknowledge Dr. Masayuki TAKEUCHI and Dr. Masahiko OSAKA (Japan Atomic Energy Agency) for their support and instructions.

The author would like to thank Prof. Roman NOWAK (Materials Science and Engineering, Helsinki University of Technology), Prof. Jerzy LIS (AGH University of Science and Technology) and Prof. Rafal Abdank-KOZUBSKI (Jagiellonian University) for their professional, polite and detailed debates with the author.

The author also would like to thank Dr. Mineaki MATSUMOTO (Japan Fine Ceramics Center), Asst. Prof. Teiichi KIMURA (Institute for Materials Research, Tohoku University), Dr. Atsuhiro YAMANAKA (Toyobo) and Mr. Tetsuhiro TANABE (Rohm) for giving invaluable comments and suggestions on the fabrication and analysis.

The author would like to give his best regards to all the members of YOSHIDA Private School (Official Association of Yamanaka Laboratory) for their intimate partnership and giving more than enough motivation. The author would like to give his respects to Dr. Masaki FUJIKANE (Matsushita Electric Industrial), a. k. a. Axis of Evil; Dr. Daigo SETOYAMA, a. k. a. Final Conscience; and Dr. Tsuyoshi HAMAGUCHI, a. k. a. Mad Kappa (Toyota Central R&D Labs.). The author would like to give his best regards to his best research partners, Mr. Takanori TANAKA (Sumitomo Metal Industries), Mr. Toru NAKAYAMA (Kyocera) and Ms. Eriko TANABE (School of Engineering, Osaka University). The author would like to express his greatest appreciation to Asst. Prof. Ken KUROSAKI and Asst. Prof. Hiroaki MUTA (Graduate School of Engineering, Osaka University). Finally, the author wishes to thank Ms. Kazuko TERASOMA (Graduate School of Engineering, Osaka University) and all the members of Yamanaka Laboratory.

List of publications

[1] Shinsuke Yamanaka, Takuji Maekawa, Hiroaki Muta, Tetsushi Matsuda, Shin-ichi Kobayashi and Ken Kurosaki, **Thermophysical properties of $SrHfO_3$ and $SrRuO_3$,** *Journal of Solid State Chemistry,* 177, Issue 10, 3484-3489 (October 2004).

[2] Shinsuke Yamanaka, Takuji Maekawa, Hiroaki Muta, Tetsushi Matsuda, Shin-ichi Kobayashi and Ken Kurosaki, **Thermal and mechanical properties of $SrHfO_3$,** *Journal of Alloys and Compounds,* 381, Issues 1-2, 295-300 (3 November 2004).

[3] Takuji Maekawa, Ken Kurosaki, Hiroaki Muta, Masayoshi Uno and Shinsuke Yamanaka, **Thermoelectric properties of perovskite type strontium ruthenium oxide,** *Journal of Alloys and Compounds,* 387, Issues 1-2, 56-59 (25 January 2005).

[4] Takuji Maekawa, Ken Kurosaki, Hiroaki Muta, Masayoshi Uno and Shinsuke Yamanaka, **Thermal and electrical properties of perovskite-type strontium molybdate,** *Journal of Alloys and Compounds,* 390, Issues 1-2, 314-317 (22 March 2005).

[5] Ken Kurosaki, Takanori Tanaka, Takuji Maekawa and Shinsuke Yamanaka, **Thermal properties of polycrystalline sintered SrY_2O_4,** *Journal of Alloys and Compounds,* 395, Issues 1-2, 318-321 (31 May 2005).

[6] Ken Kurosaki, Takuji Maekawa, Hiroaki Muta and Shinsuke Yamanaka, **Effect of spark plasma sintering temperature on thermoelectric properties of (Ti,Zr,Hf)NiSn half-Heusler compounds,** *Journal of Alloys and Compounds,* 397, Issues 1-2, 296-299 (19 July 2005).

[7] Ken Kurosaki, Takanori Tanaka, Takuji Maekawa and Shinsuke Yamanaka, **Thermophysical properties of SrY_2O_4,** *Journal of Alloys and Compounds,* 398, Issues 1-2, 304-308 (2 August 2005).

[8] Shinsuke Yamanaka, Ken Kurosaki, Takuji Maekawa, Tetsushi Matsuda, Shin-ichi Kobayashi and Masayoshi Uno, **Thermochemical and thermophysical properties of alkaline-earth perovskites,** *Journal of Nuclear Materials,* 344, Issues 1-3, 61-66 (1 September 2005).

[9] Takuji Maekawa, Ken Kurosaki and Shinsuke Yamanaka, **Thermal and mechanical properties of perovskite-type barium hafnate,** *Journal of Alloys and Compounds,* 407, Issues 1-2, 44-48 (5 January 2006).

[10] Ken Kurosaki, Jun Adachi, Takuji Maekawa and Shinsuke Yamanaka, **Thermal conductivity analysis of $BaUO_3$ and $BaZrO_3$ by semiempirical molecular dynamics simulation,** *Journal of Alloys and Compounds,* 407, Issues 1-2, 49-52 (5 January 2006).

[11] Takuji Maekawa, Ken Kurosaki, Hiroaki Muta, Masayoshi Uno, Shinsuke Yamanaka, Tetsushi Matsuda and Shin-ichi Kobayashi, **Thermophysical properties of perovskite type alkaline earth hafnates,** *Ceramic Transactions*, 179(Advances in Electronic and Electrochemical Ceramics), 69-76 (2006).

[12] Takanori Tanaka, Ken Kurosaki, Takuji Maekawa, Hiroaki Muta, Masayoshi Uno and Shinsuke Yamanaka, **Thermophysical properties of sintered SrY_2O_4 and the related compounds applicable to thermal barrier coating materials,** *Ceramic Transactions,* 179(Advances in Electronic and Electrochemical Ceramics), 77-83 (2006).

[13] Takuji Maekawa, Ken Kurosaki and Shinsuke Yamanaka, **Thermal and mechanical properties of polycrystalline $BaSnO_3$,** *Journal of Alloys and Compounds,* 416, Issues 1-2, 214-217 (8 June 2006).

[14] Takuji Maekawa, Ken Kurosaki and Shinsuke Yamanaka, **Physical properties of polycrystalline $SrVO_{3-\delta}$,** *Journal of Alloys and Compounds,* 426, Issues 1-2, 46-50 (21 December 2006).

[15] Masahiro Inoue, Hiroaki Muta, Takuji Maekawa, Shinsuke Yamanaka, Katsuaki Suganuma, **Thermal conductivity of isotropic conductive adhesives composed of an epoxy-based binder,** Conference on High Density Microsystem Design and Packaging and Component Failure Analysis, Shanghai, China, June 27-30, 2006, 236-241 (2006).

[16] Takuji Maekawa, Ken Kurosaki and Shinsuke Yamanaka, **Thermophysical properties of BaY_2O_4: A new candidate material for thermal barrier coatings,** *Materials Letters*, 61, Issues 11-12, 2303-2306 (May 2007).

[17] Takuji Maekawa, Ken Kurosaki, Takanori Tanaka and Shinsuke Yamanaka, **Thermal conductivity of titanium dioxide films grown by metal-organic chemical vapor deposition,** *Surface and Coatings Technology*, in press (DIO:10.1016/j.surfcoat.2007.11.017).

[18] Takuji Maekawa, Ken Kurosaki, Takanori Tanaka and Shinsuke Yamanaka, **Morphology and Thermal conductivity of zirconia films grown by metal-organic chemical vapor deposition,** *Surface and Coatings Technology*, to be submitted.

[19] Takuji Maekawa, Ken Kurosaki, Eriko Tanabe and Shinsuke Yamanaka, **Thermal conductivity of hafnium dioxide films grown by metal-organic chemical vapor deposition**, *Surface and Coatings Technology*, to be submitted.

[20] Takuji Maekawa, Ken Kurosaki, Eriko Tanabe and Shinsuke Yamanaka, **Fabrication and thermal property measurement of $SrTiO_3$ films grown by metal-organic chemical vapor deposition**, *Surface and Coatings Technology*, to be submitted.

Conference contributions

[1] Tetsushi Matsuda, Takuji Maekawa, Ken Kurosaki, Hiroaki Muta, Masayoshi Uno, Shin-ichi Kobayashi and Shinsuke Yamanaka, **Thermal Properties of $SrZrO_3$ and $SrCeO_3$**, The 5th International Meeting of Pacific Rim Ceramics Societies, 09-P-42, Nagoya, Japan, 29 September-2 October 2003.

[2] Takuji Maekawa, Hiroaki Muta, Ken Kurosaki and Shinsuke Yamanaka, **Mechanical Properties of Perovskite Type Strontium Oxides**, 28th International Conference and Exposition on Advanced Ceramics and Composites, CB-S4-80-2004, Florida, USA, 25-30 January 2004.

[3] Ken Kurosaki, Takuji Maekawa, Hiroaki Muta and Shinsuke Yamanaka, **Thermal Properties of Perovskite Type Strontium Oxides**, 28th International Conference and Exposition on Advanced Ceramics and Composites, CB-S4-87-2004, Florida, USA, 25-30 January 2004.

[4] Ken Kurosaki, Takuji Maekawa, Hiroaki Muta, Tetsushi Matsuda, Shin-ichi Kobayashi, Masayoshi Uno and Shinsuke Yamanaka, **Physical properties of perovskite type oxides 6 -Mechanical properties of $SrHfO_3$ and $SrRuO_3$-**, Annual Meeting of The Ceramic Society of Japan, 2004, 2H13, Fujisawa, JAPAN, 22-24 March 2004.

[5] Takuji Maekawa, Ken Kurosaki, Hiroaki Muta, Tetsushi Matsuda, Shin-ichi Kobayashi, Masayoshi Uno and Shinsuke Yamanaka, **Physical properties of perovskite type oxides 7 -Thermal properties of $SrHfO_3$ and $SrRuO_3$-**, Annual Meeting of The Ceramic Society of Japan, 2004, 2H14, Fujisawa, JAPAN, 22-24 March 2004.

[6] Takuji Maekawa, Ken Kurosaki, Hiroaki Muta, Tetsushi Matsuda, Shin-ichi Kobayashi and Shinsuke Yamanaka, **Physical Properties of Perovskite Type Alkali Earth Molybdates**, 106th Annual Meeting & Exposition of The American Ceramic Society, AM-EL-48-2004, Indiana, USA, 18-21 April 2004.

[7] Takuji Maekawa, Ken Kurosaki, Hiroaki Muta, Tetsushi Matsuda, Shin-ichi Kobayashi, Masayoshi Uno and Shinsuke Yamanaka, **Physical properties of perovskite type oxides 9 -Thermal properties of $BaMoO_3$ and $SrMoO_3$-**, 17th Fall Meeting of The Ceramic Society of Japan, 1P28, Ishikawa, JAPAN, 17-19 September 2004.

[8] Ken Kurosaki, Takuji Maekawa, Hiroaki Muta, Tetsushi Matsuda, Shin-ichi Kobayashi, Masayoshi Uno and Shinsuke Yamanaka, **Physical properties of perovskite type oxides 8 -Mechanical properties of $BaMoO_3$ and $SrMoO_3$-**, 17th Fall Meeting of The Ceramic Society of Japan, 1P29, Ishikawa, JAPAN, 17-19 September 2004.

[9] Takanori Tanaka, Takuji Maekawa, Ken Kurosaki, Hiroaki Muta, Masayoshi Uno and Shinsuke Yamanaka, **Thermal and mechanical properties of SrY_2O_4**, Annual Meeting of The Ceramic Society of Japan, 2005, 3D23, Okayama, JAPAN, 22-24 March 2005.

[10] Takuji Maekawa, Ken Kurosaki, Tetsushi Matsuda, Shin-ichi Kobayashi, Hiroaki Muta, Masayoshi Uno and Shinsuke Yamanaka, **Thermal and mechanical properties of perovskite type oxides 10 -Thermal and mechanical properties of $BaHfO_3$-**, Annual Meeting of The Ceramic Society of Japan, 2005, 3D24, Okayama, JAPAN, 22-24 March 2005.

[11] Ken Kurosaki, Takuji Maekawa, Tetsushi Matsuda, Shin-ichi Kobayashi, Hiroaki Muta, Masayoshi Uno and Shinsuke Yamanaka, **Thermal and mechanical properties of perovskite type oxides 11 -Perovskite type oxides as candidate for TBC materials-**, Annual Meeting of The Ceramic Society of Japan, 2005, 3D25, Okayama, JAPAN, 22-24 March 2005.

[12] Takuji Maekawa, Ken Kurosaki, Tetsushi Matsuda, Shin-ichi Kobayashi, Hiroaki Muta, Masayoshi Uno and Shinsuke Yamanaka, **Thermophysical Properties of Perovskite Type Alkali Earth Hafnates**, 107th Annual Meeting, Exposition, & Technology Fair of The American Ceramic Society, AM-S15-6-2005, Maryland, USA, 10-13 April 2005.

[13] Takanori Tanaka, Ken Kurosaki, Takuji Maekawa, Hiroaki Muta, Masayoshi Uno and Shinsuke Yamanaka, **Thermophysical Properties of Sintered SrY_2O_4 and the Related Compounds as Candidate for TBC Materials**, 107th Annual Meeting, Exposition, & Technology Fair of The American Ceramic Society, AM-S15-7-2005, Maryland, USA, 10-13 April 2005.

[14] Shinsuke Yamanaka, Takuji Maekawa, Ken Kurosaki, Tetsushi Matsuda, Shin-ichi Kobayashi, Hiroaki Muta and Masayoshi Uno, **Thermal, Mechanical, and Electrical Properties of Alkaline-Earth Perovskites Applicable to Attractive Functional Materials**, 107th Annual Meeting, Exposition, & Technology Fair of The American Ceramic Society, AM-S15-26-2005, Maryland, USA, 10-13 April 2005.

[15] Takuji Maekawa, Ken Kurosaki, Hiroaki Muta, Masayoshi Uno and Shinsuke Yamanaka, **Thermal and mechanical properties of perovskite type oxides 13 -Thermal and mechanical properties of $BaMoO_3$-$SrMoO_3$ solid solutions-**, 18th Fall Meeting of The Ceramic Society of Japan, 1P15, Osaka, JAPAN, 27-29 September 2005.

[16] Takuji Maekawa, Ken Kurosaki, Hiroaki Muta, Masayoshi Uno and Shinsuke Yamanaka, **Thermal and mechanical properties of perovskite type oxides 14 -Electrical properties of $BaMoO_3$-$SrMoO_3$ solid solutions-**, 18th Fall Meeting of The Ceramic Society of Japan, 1P16, Osaka, JAPAN, 27-29 September 2005.

[17] Takuji Maekawa, Ken Kurosaki, Hiroaki Muta, Masayoshi Uno and Shinsuke Yamanaka, **Thermal and mechanical properties of perovskite type oxides 15 -Thermal and mechanical properties of $SrFeO_{3-x}$ and $SrVO_{3-x}$-**, 18th Fall Meeting of The Ceramic Society of Japan, 1P17, Osaka, JAPAN, 27-29 September 2005.

[18] Ken Kurosaki, Takuji Maekawa, Hiroaki Muta, Masayoshi Uno and Shinsuke Yamanaka, **Thermal and mechanical properties of perovskite type oxides 16 -Electrical properties of $SrFeO_{3-x}$ and $SrVO_{3-x}$-**, 18th Fall Meeting of The Ceramic Society of Japan, 1P17, Osaka, JAPAN, 27-29 September 2005.

[19] Takanori Tanaka, Takuji Maekawa, Ken Kurosaki, Hiroaki Muta, Masayoshi Uno, Shinsuke Yamanaka and Masayuki Takeuchi, **Fabrication and thermal characterization of oxide thin films prepared by MOCVD method**, 18th Fall Meeting of The Ceramic Society of Japan, 1P23, Osaka, JAPAN, 27-29 September 2005.

[20] Takuji Maekawa, Tanori Tanaka, Ken Kurosaki, Hiroaki Muta, Masayoshi Uno and Shinsuke Yamanaka, **Fabrication and physical properties measurement of EBC-TBC oxide thin films with nanostructure control,** 4th 21st Century Center of Excellence (21COE) "Towards Creating New Industry Based on Inter-Nanoscience" International Symposium, P087, Toba, JAPAN, 18-19 November 2005.

[21] Ken Kurosaki, Takanori Tanaka, Takuji Maekawa, Hiroaki Muta, Masayoshi Uno and Shinsuke Yamanaka, **Physical properties of alkaline earth – yttrium ternary oxides**, Annual Meeting of The Ceramic Society of Japan, 2006, 3C02L, Tokyo, JAPAN, 14-16 March 2006.

[22] Takuji Maekawa, Takanori Tanaka, Ken Kurosaki, Hiroaki Muta, Masayoshi Uno, Shinsuke Yamanaka and Masayuki Takeuchi, **Fabrication and characterization of oxide thin films prepared by MOCVD method**, Annual Meeting of The Ceramic Society of Japan, 2006, 3C19, Tokyo, JAPAN, 14-16 March 2006.

[22] Takuji Maekawa, Ken Kurosaki, Hiroaki Muta, Masayoshi Uno and Shinsuke Yamanaka, **Thermal and mechanical properties of alkaline earth - rare earth oxides**, 19th Fall Meeting of The Ceramic Society of Japan, 2P51, Yamanashi, JAPAN, 19-21 September 2006.

[23] Takuji Maekawa, Tanori Tanaka, Ken Kurosaki, Hiroaki Muta, Masayoshi Uno and Shinsuke Yamanaka, **Thermal property optimization of EBC-TBC oxide films with nanostructure control and nanoscale analysis,** 5th 21st Century Center of Excellence (21COE) "Towards Creating New Industry Based on Inter-Nanoscience" International Symposium, P109, Awaji, JAPAN, 8-9 December 2006.

[24] Takuji Maekawa, Ken Kurosaki, Hiroaki Muta, Masayoshi Uno, Akira Kitamura and Shinsuke Yamanaka, **Microstructure and Thermal property of titania films prepared by MOCVD method,** Annual Meeting of The Ceramic Society of Japan, 2007, 1D21, Tokyo, JAPAN, 21-23 March 2007.

[25] Takuji Maekawa, Ken Kurosaki, Hiroaki Muta, Masayoshi Uno and Shinsuke Yamanaka, **Microstructure and Thermal property of zirconia films prepared by MOCVD method,** 20th Fall Meeting of The Ceramic Society of Japan, 2P1-18, Aichi, JAPAN, 12-14 September 2007.

Research funds

[1] **Independent research grants for PhD candidate** (for the project: Fabrication and physical properties measurement of EBC·TBC oxide thin films with nanostructure control), 21st Century Center of Excellence (21COE) "Towards Creating New Industry Based on Inter-Nanoscience" Nanomaterial research group, JPY 0.5 million, 2005.

[2] **Funds for student seminar 2006 in Poland**, 21st Century Center of Excellence (21COE) "Towards Creating New Industry Based on Inter-Nanoscience" Nanomaterial research group, JPY 1 million, 2005.

[3] **Independent research grants for PhD candidate** (for the project: Thermal property optimization of EBC·TBC oxide films with nanostructure control and nanoscale analysis), 21st Century Center of Excellence (21COE) "Towards Creating New Industry Based on Inter-Nanoscience" Nanomaterial research group, JPY 0.5 million, 2006.

[4] **Funds for student seminar 2007 in Japan**, 21st Century Center of Excellence (21COE) "Towards Creating New Industry Based on Inter-Nanoscience" Nanomaterial research group, JPY 0.4 million, 2006.